Mechanical Properties and Deformation Mechanisms in β-type Ti-Mo Alloys

Mechanical Properties and Deformation Mechanisms in β-type Ti-Mo Alloys

JI Xin

February 2018

Mechanical Properties and Deformation Mechanisms in β-type Ti-Mo Alloys

JI Xin
Doctoral Program in Materials Science and Engineering

Submitted to the Graduate School of
Pure and Applied Sciences
in Partial Fulfillment of the Requirements
for the Degree of Doctor of Philosophy in
Engineering

at the
University of Tsukuba

Abstract

During the past few decades, β-Ti alloys have attracted extensive attention for applications in aerospace, biomedical and energy industries due to their superior properties such as high specific strength, high corrosion resistance, low Young's modulus and good biocompatibility. Based on the chemical composition and thermomechanical treatment, the β-Ti alloys may contain various pases in their microstructure, such as equilibrium α and β phases, and metastable α', α" and ω phases. It has been widely acknowledge that the mechanical properties of β-Ti alloys depend significantly on the deformation behaviors, such as dislocation slip, deformation twinning and stress-induced martensitic transformation. Therefore, the comprehensive investigation on the deformation mechanisms and the related mechanical properties of β-Ti alloys is suggested of great importance.

The recently developed Ti-7.5Mo alloy with fully α" martensite has been revealed with low Young's modulus and good biocompatibility, which is regarded as a promising candidate for implant material. However, this alloy also exhibits relatively low mechanical strength, which restricts its further development. Since the mechanical properties are significantly depending on the deformation mechanisms, therefore, the present thesis firstly focused on deformation mechanisms of as-quenched α" martensite in the Ti-7.5Mo alloy. The as-quenched and deformed microstructures of α" martensite were investigated by combining scanning electron microscopy (SEM) and transmission electron microscopy (TEM). A microstructural patch of interest was tracked upon tensile deformation to a strain level of 5% by SEM, followed by TEM characterization of deformed microstructure in a focused ion beam (FIB)-fabricated lamella. The as-quenched α" martensite consist of $\{111\}_{\alpha''}$-type I transformation twins. After 5% deformation straining, the activation of a new $\{112\}_{\alpha''}$-type I deformation twinning was identified. Furthermore, the mechanism of the newly reported $\{112\}_{\alpha''}$-type I deformation twinning has been analyzed based on the crystallographic deformation twinning theory.

Then, in order to improve the strength while keeping the low Young's modulus of the Ti-7.5Mo alloy, the effect of oxygen content on the microstructure and mechanical properties of the Ti-7.5Mo alloy have been investigated. We developed a series of Ti-7.5Mo alloys with different oxygen contents (0~0.5 wt.%). The microstructure was characterized by SEM together with TEM. The crystal structure and phase stability of α" martensite in Ti-7.5Mo alloys with different oxygen contents were investigated on the basis of X-ray diffraction (XRD) and differential scanning calorimeter (DSC) analyses. Hardness and tensile tests were carried out to illustrate strengthening mechanism caused by different oxygen content. Among the newly developed alloys, Ti-7.5Mo-xO ($x \leq 0.3$ (wt.%)) alloys have been reported with an excellent combination of high yield strength (~640 MPa) and elongation (~28%), as well as low Young's modulus (~60 GPa). In particular, the present alloys are based on simply binary alloys, while most of other biomedical alloys are multicomponent systems. This may be advantageous in terms of the materials cost and processing point of view.

Furthermore, as a unique twinning mode in bcc alloys, {332}<113>$_\beta$ twinning contributes to the pronounced work-hardening in β-Ti alloys with bcc-β phase. This is similar to the twinning-induced plasticity (TWIP) in steels. Some investigations revealed that the mechanical properties and deformation mechanisms of β-Ti alloys have a strong dependence on the strain rate. However, there is a lack of understanding regarding the mechanism of strain rate dependence of work-hardening behavior in β-Ti alloys, in particular, about the effect of {332}<113>$_\beta$ twinning. The purpose of the last part of the thesis was to investigate the effect of strain rate on the tensile deformation behaviors in a β-Ti alloy showing TWIP effect. We focused on a Ti-10Mo-1Fe (wt.%) alloy, which deforms mainly by {332}<113>$_\beta$ twinning. The work-hardening behavior was investigated by monotonic tensile tests at different strain rates ranging from $2.8x10^{-5}$ s^{-1} to $2.8x10^{-1}$ s^{-1}. The microstructure evolution was characterized by Electron Backscattered Diffraction (EBSD) and XRD on {332}<113>$_\beta$ twins and dislocations. The results revealed lower increasing rates of {332}<113>$_\beta$ twins and dislocation density at higher strain rates deformation. This is ascribed to the adiabatic heating, leading to the reduced work-hardening rate at higher strain rates. The correlation between the work-hardening behavior and microstructure evolution are of great importance for improving the strength-ductility balance of β-Ti alloys.

Keywords: β-Ti alloy; deformation mechanisms; mechanical properties; orthorhombic-α" martensite; {332}<113>$_\beta$ twinning

Chapter 1 Introduction

1.1 Titanium and its alloys

During the past few decades, titanium and its alloys have been increasingly developed due to their superior properties such as low density, high strength, excellent corrosion resistance, and good biocompatibilities [1–3]. They are widely used in various applications in aerospace, chemical processing equipment, and biomedical industries, as illustrated in Fig. 1-1 [3]. The primarily advantages of titanium alloys include two parts [1]: (i) high specific strength (ratio between strength and density). The specific strength of titanium alloys are better at temperature below 500 K and even shows promising properties at higher temperature compared with other structural materials, as shown in Fig. 1-2 [1]. That's the reason why the titanium alloys could play an important role in the aerospace applications; (ii) excellent corrosion resistance in critical environments especially for pitting and corrosion cracking. It is because of the easily formed oxide film with any environment containing oxygen on the surface, which provides the titanium outstanding resistance to corrosion in a wide range of aggressive media. These desirable properties make titanium alloys attractive for various applications like aircraft (high specific strength), aero-engines (high specific strength and good creep resistance up to about 800 K), chemical processing equipment (good corrosion resistance) and biomedical devices (corrosion resistance and high strength) [1]. Besides, titanium and its alloys also have good toughness property making them useful for precision mechanism gears.

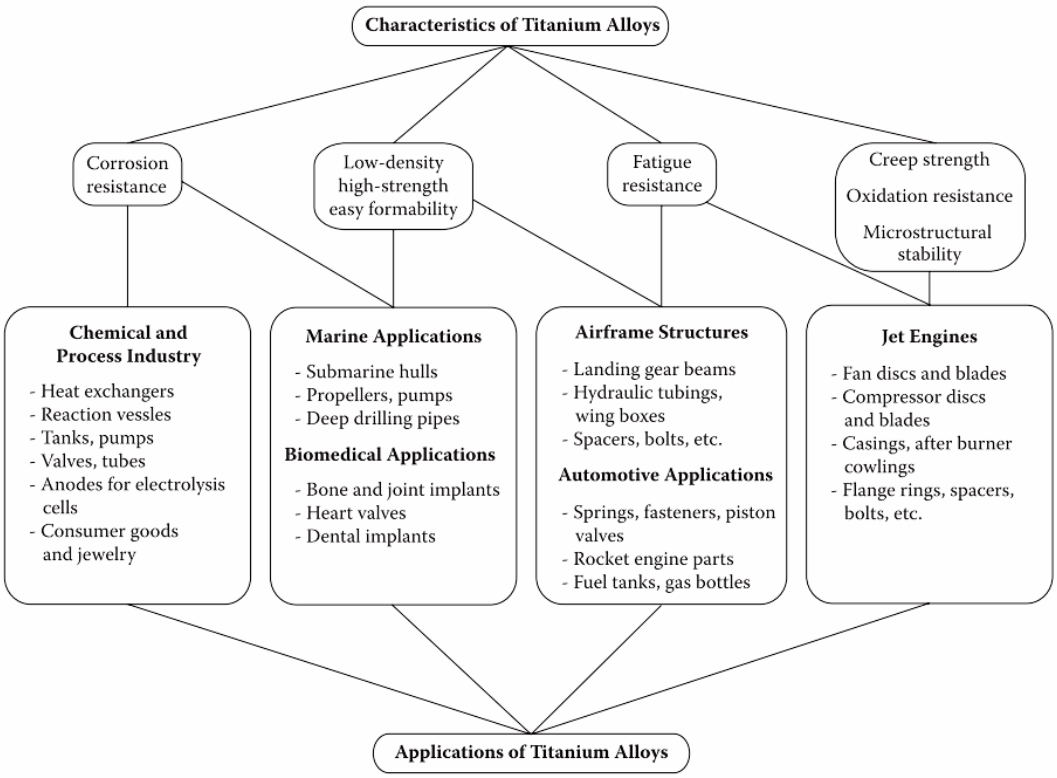

Fig. 1-1 General characteristics and typical application of titanium alloys. [3]

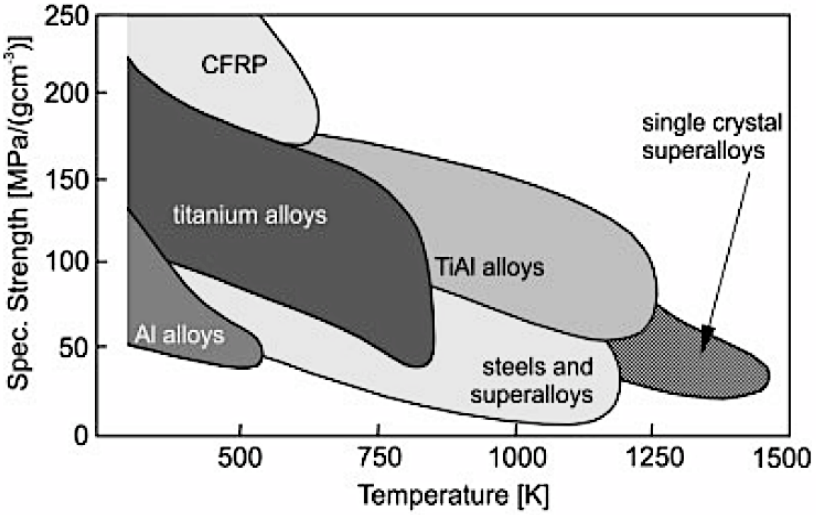

Fig. 1-2 Specific strength versus use temperature of various structural materials compared with titanium alloy.

However, the relatively high cost of titanium alloys that limits their range of applications. Actually, titanium is not rare since it ranks the fourth most abundant structural metal in the earth's crust, after aluminum, iron and magnesium. Unfortunately, it usually occurs not in a pure state and the concentration is relatively low. Thus, the difficulty in processing the metal makes it expensive [1]. The mechanical properties, such as strength, ductility, creep resistance, and fracture toughness, depend significantly on the microstructures, which are formed during the thermo-mechanical processing and thermal treatment procedures. Extensive researches have been carried out to understand the relationships between the microstructure evolution and mechanical properties of titanium alloys, which are essential for the design of new alloy systems, cost control and further development of titanium alloys.

1.1.1 Elemental addition in titanium alloys

There are two crystal structures in pure titanium, namely α titanium with hexagonal close packed (hcp) crystal structure and β-titanium with body-centered crystal (bcc) structure. The β-phase has been reported to be more stable at high temperature compared with the α phase. The phase transformation from β to α may take place when the temperature decreases to ~882 °C for pure titanium [4]. This temperature is called β transus temperature. Based on the effect on the β transus temperature, the alloying elements are classified as neutral, α-stabilizers or β-stabilizers, as shown schematically in Fig. 1-3 [1]. The α-stabilizers increase the β transus temperatures, while β-stabilizers shift the β phase field to lower temperatures. Neutral elements have only minor influences on the β transus temperature. Among the α- stabilizers of Al, oxygen, nitrogen, and carbon, Al is treated as the most important element for stabilizing the α phase. It can increase the β transus temperature significantly and lead to the strengthening effect due to the large solubility in both α and β phases. It is well established that the mechanical properties of titanium alloys are sensitively dependent on the interstitial solutes such as oxygen, nitrogen, and carbon [1]. For example, extensive efforts have revealed

the oxygen as an effective element to improve the strength of titanium alloys due to its solid-solution strengthening effect [5–7].

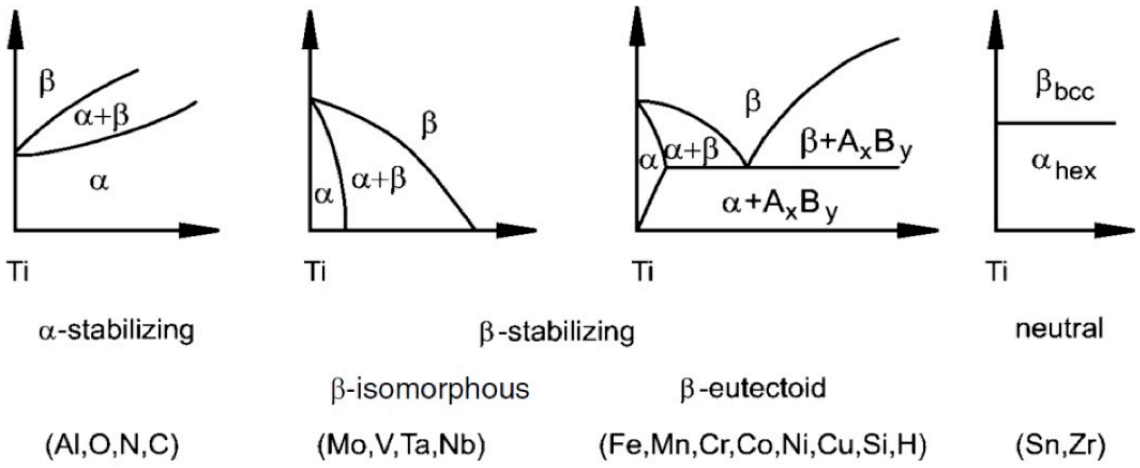

Fig. 1-3 Effect of alloying elements on phase diagrams of titanium alloys [1].

In order to evaluate the effect of α stabilizer in multicomponent titanium alloys, the concept of Al equivalency ($[Al]_{eq}$) is used with the following Eq. 1-1 [1], where the element symbol means the weight percent (wt.%) of each element in the alloy:

$$[Al]_{eq} = [Al] + 0.17[Zr] + 0.33[Sn] + 10[O] \quad 1\text{-}1$$

The β-stabilizers are divided into isomorphous and eutectoid elements, depending on exitence of a solid solution or eutectoid compound at a sufficiently elevated temperature. Both types of phase diagrams are shown schematically in Fig. 1-3. With higher solubility in titanium, the β-isomorphous elements such as Mo, V, Ta and Nb are more effective β phase stabilizers. On the other hand, the β-eutectoid elements such as Fe, Mn, Cr, Co, Ni, Cu, Si and H are of great importance making titanium intermetallic compounds with low volume fraction. Similarly, the Mo equivalency ($[Mo]_{eq}$) is used for all β phase stabilizers to describe the β phase stability. The equation is shown as follows [8]:

$$[Mo]_{eq} = [Mo] + 0.67[V] + 0.44[W] + 0.28[Nb] + 0.22[Ta] + 1.6[Cr] + 2.9[Fe] - 1.0[Al] \quad 1\text{-}2$$

In addition to the α- and β-stabilizers, there are some elements (such as Sn, Zr and Hf) regarded as neutral elements, which have negligible effets on the β transus temperature (Fig. 1-3). However, as far as strength is concerned, they are not neutral since they can primarily contribute to the strengthening of α phase. Many commercial multicomponent alloys contain Zr and Sn considered as α phase stabilizing elements. This is due to the chemical similarity of Zr to Ti and Sn can replace Al in the hexagonal ordered Ti_3Al phase. Besides, these neutral elements can completely dissolve in the α and β phases of titanium alloys.

1.1.2 Classification of titanium alloys

The schematically classification of titanium alloys is shown in Fig. 1-4, according to their positions in a pseudo-binary section through a β isomorphous phase diagram. Generally, titanium alloys are classified into three main categories: α-Ti alloys, α+β-Ti alloys, and β-Ti alloys. Furthermore, the β-Ti alloys can be further divided into metastable β-Ti and stable β-Ti alloys. The fundamental properties of these three categories are outlined in Table 1-1.

α-Ti alloys comprise commercial pure (cp) titanium alloys and alloys with only α-stabilizers and/or neutral elements, such as Ti-3Al-2.5V, and Ti-5Al-2.5Sn alloys. These classes of titanium alloys consist of mainly α phase and a small amount of β phase (2-5 vol.%) at grain boundaries [4]. The β phase is helpful in controlling the recrystallized α grain size and improving the hydrogen tolerance of α-Ti alloys. Due to the excellent corrosion resistance of α-Ti alloys compared to stainless steel, they are widely used in chemical industry. They are also become popular for heat exchanger and other piping applications because of their good weldability and general fabricability. In addition, they usually show good creep strength, which is preferred for elevated temperature applications up to ~700 K. However, the α-Ti alloys exhibit relatively low strength due to the lack of solid solution strengthening elements. Meanwhile, the formability of α-Ti alloys is relatively low since the hcp structure of α phase requires a high stress to trigger the non-basal slip systems.

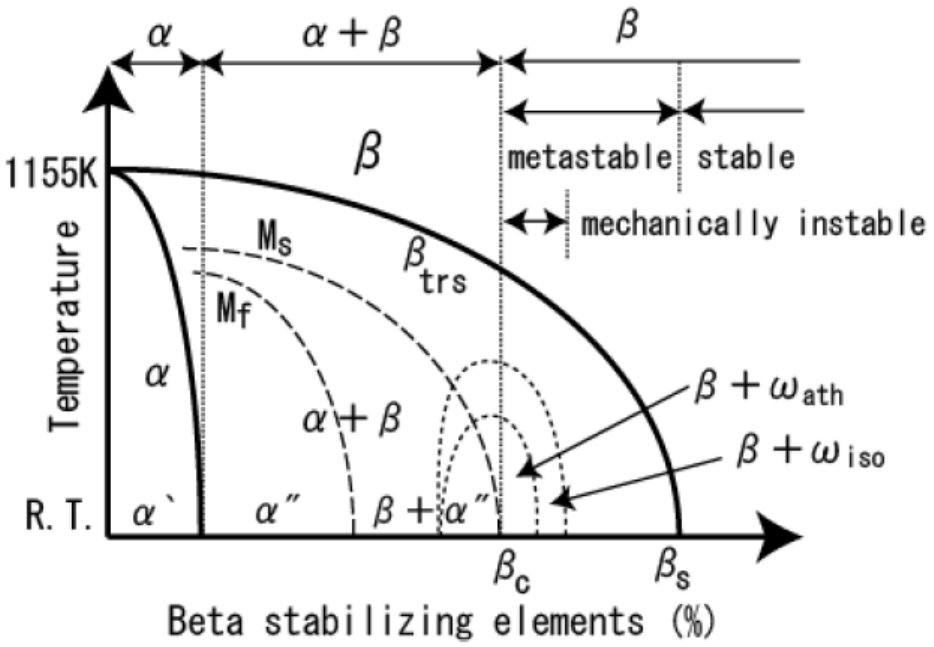

Fig. 1-4 Pseudo-binary phase diagram to classify titanium alloys with decomposition products of β phase. β_c is the critical minimum β-stabilizer amount for the metastable β-Ti alloys to retain β completely on quenching from β phase field and β_s is the minimum amount of β-stabilizer for stable β-Ti alloys: β_{trs}, M_s and M_f refer to β transus, martensite start and finish temperatures, respectively.

Table 1-1 Some fundamental properties comparison of α, α+β, β Ti alloys

	α	α+β	β
Density	+	+	-
Strength	-	+	++
Ductility	-/+	+	+/-
Fracture toughness	+	-/+	+/-
Creep strength	+	+/-	-
Corrosion behavior	++	+	+/-
Oxidation behavior	++	+/-	-
Weldability	+	+/-	-
Cold formability	--	-	-/+

α+β-Ti alloys have a range in the phase diagram (Fig. 1-4) from the α/α+β phase boundary up to the intersection of the Ms-line with room temperature. This type of Ti-alloys offers an excellent combination of strength, toughness and high-temperature properties, which makes them strongly attractive in aerospace and other fields demanding high strength alloys. α+β-Ti alloys contain both α- and β-stabilizers and have the β phase ranging from about 5 to 40 vol.% at room temperature. Furthermore, they can be further strengthened by solution treatment and aging, resulting in a variety of microstructure/property combinations. α+β-Ti alloys include the currently most widely used titanium alloy, *i.e.*, Ti-6Al-4V. It exhibits an excellent balance of strength, ductility, fatigue and excellent damage tolerance properties, which makes it intensively developed in the aerospace, automotive and medicine industry. Apart from Ti-6Al-4V, some α+β-Ti alloys have special features and are used as high-temperature alloys, such as Ti-6Al-2Sn-4Zr-2Mo-0.1Si (Ti-6242) and (Ti-5.8Al-4Sn-3.5Zr-0.5Mo-0.7Nb-0.35Si-0.06C (IMI 834). They are mainly applied in the high-pressure compressor stages of aero-engines where the temperature exceeds 300 K and Ti-6Al-4V cannot be used because of creep consideration.

β-Ti alloys can be further divided into metastable and stable β-Ti alloys, depending on the amount of β-stabilizers, as shown in Fig. 1-4. With sufficient β-stabilizers, the β phase can be fully achieved upon quenching from high-temperature β phase field and no martensitic transformation occurs. α phase can precipitate from the metastable β phase by solution treatment and aging below β transus temperature, resulting in the strengthening of β-Ti alloys. Thus they could be improved by adjusting the chemical composition and formation processing to satisfy diverse demands of high strength, adequate toughness and fatigue resistance for airframe application. Actually most of the commercially used β-Ti alloys are metastable β-Ti alloys. In addition, metastable β-Ti alloys exhibit good corrosion resistance, good biocompatibility, shape memory effect and superelasticity, which make them attracting more and more attentions. A more detailed description of β-Ti alloys will be presented in the next section.

1.2 β-Ti alloys

1.2.1 Mechanical properties

In general, β-Ti alloys is the alloy with sufficiently rich β-stabilizers that the β phase can be retained and no martensitic transformation occurs by quenching from the β phase field to room temperature [4]. Bania [8] correlated that a $[Mo]_{eq}$ value above about 10 was required to retain the full β phase upon quenching. Meanwhile, Eylon *et al*. [9] suggested that a definition of β alloys based on the values of $[Mo]_{eq}$, in which the β alloys with $[Mo]_{eq}$ ranging from 8-30 were termed "metastable β", those above 30 identified as "stable β", and those below 8 were considered as "β-rich α+β" alloys. Sometimes alloys with roughly $[Mo]_{eq}$ values of 5-10 were also identified as "near-β" alloys. Since a number of leaner Ti alloys contain sufficient β stabilizer to confer improved formability and forgeability, and a good heat treatment strengthening response, they are often treated as β-Ti alloys. These can include alloys such as Ti–5Al–2Sn–2Zr–4Mo–4Cr (Ti17, $[Mo]_{eq}$ = 5.4), Ti–5Al–2Sn–2Cr–4Mo–4Zr-1Fe (Beta CEZ, $[Mo]_{eq}$ = 5.1) and Ti–13Nb–13Zr alloy.

Table 1-2 Advantages and disadvantages of β-Ti alloys [1].

Advantages	**Disadvantages**
-high specific strength	-high density
-low modulus	-low modulus
-high strength/high toughness	-poor low- and high-temperature properties
-high fatigue strength	-small processing window (some alloys)
-good deep hardenability	-high formulation cost
-low forging temperature	-segregation problems
-cold formable (some alloys)	-high springback
-easy to heat treat	-microstructural instabilities
-excellent corrosion resistance (some alloys)	-poor corrosion resistance (some alloys)
-excellent combustion resistance (some alloys)	-interstitial pick up

The advantages and disadvantages of β-Ti alloys are listed in Table 1-2 and commercial β-Ti alloys are shown in Table 1-3 in a descending order of $[Mo]_{eq}$, together with applications and introduced periods [9]. Considerable efforts have been devoted to exploring novel β-Ti alloys for diverse applications because of their superior properties, such as high strength, low Young's modulus, good biocompatibility, superelasticity, and better formability compared to α-Ti and α+β-Ti alloys. So far the primary application of β-Ti alloys is for the aerospace field. The airframe weight of Boeing 777 contains about 10% of titanium alloys and it is the first commercial airplane in which β-Ti alloys exceed the classical Ti-6Al-4V alloy in the mass content. The main reason is the application of the high strength β-type Ti-10-2-3 in the landing gear

structure. Other β-Ti alloys such as Ti-7Mo-3Nb-3Cr-3Al (Ti-7333) and Ti-5Al-5Mo-5V-3Cr (Ti-5553) [10], with ultrahigh strength and excellent ductility, have also been used for aerospace applications.

Meanwhile, extensive research attentions have been focused on the development of β-Ti alloys for biomedical applications. It is well known that the α+β type Ti-6Al-4V alloy is currently the most popular titanium alloy used in the biomedical field. This alloy has Young's modulus of ~110 GPa, which is much lower than that of other alloys, such as stainless steel (~200 GPa) or Co-Cr-Mo alloys (~210 GPa) [11]. However, these currently used alloys present some drawbacks such as low mechanical biocompatibility with human bones and long-term health issues. Moreover, the Young's modulus of Ti-6Al-4V is still higher than the human bones (10-40 GPa), which may cause stress-shielding effect [9-10]. Thus, some novel β-Ti alloys with lower modulus, better formability and non-toxic elements (i.e. Al- and V-free) have been attracting more and more attentions for biomedical applications, such as Ti-7.5Mo (wt.%) [12,13], Ti-15Mo (wt.%) [14], Ti-12Mo-6Zr-2Fe (wt.%) [15], and Ti-29Nb-13Ta-4.6Zr (wt.%, TNTZ) [16]. In particular, Ti-35Nb-4Sn alloy has been reported with the lowest Young's modulus (40 GPa) reported so far among the developed biomedical titanium alloys. Meanwhile, Ti-7.5Mo alloy has been recently developed by Ho *et al.* [12] with a low Young's modulus of ~60GPa [17]. This alloy also exhibits good biocompatibility which was confirmed through cytotoxicity test and animal implantation study [18].

Despite the aerospace and biomedical applications, β-Ti alloys are also widely used in chemical industry for downhole service and other fields [1]. However, there are still several problems leading to the limited use of these alloys, including relatively higher costs as compared to α+β-Ti alloys, microstructural instability, low ductility in high strength weldments, potential melting segregation problems and a lack of sufficient design data [9]. It has been widely acknowledged that the mechanical properties of β-Ti alloys depend significantly on the deformation behaviors, such as dislocation slip, deformation twinning and stress-induced martensitic transformation [19,20]. Therefore, the comprehensive investigation of the deformation mechanisms of β-Ti alloys is suggested of great importance. Meanwhile, extensive studies have been expended for the design of cost-effective β-Ti alloys. For instance, some of them were developed for the reduced cost by using iron as an inexpensive but effective β-stabilizer, such as Beta CEZ and SP700. In addition, the interstitial elements such as oxygen, carbon and nitrogen have been revealed as effective elements to improve the strength and some functional properties of β-Ti alloys [21–23]. The novel β-Ti alloys with an excellent combination of mechanical properties such as high strength, good ductility and low Young's modulus are always desirable.

.

Table 1-3 Composition, category, applications, source and year of introduction of major β-titanium alloys [9]

Alloy composition	Commercial name	Category	Mo Eq.	Actual and potential applications	Year introduced (company)
Ti-35V-15Cr	Alloy C	Beta	47	Burn resistant alloy	1990 (P&W)
Ti-40Mo		Beta	40	Corrosion resistance	1952 (RemCru)
Ti-30Mo		Beta	30	Corrosion resistance	1952 (RemCru)
Ti-6V-6Mo-5.7Fe-2.7Al	TIMETAL 125	Metastable	24	High strength aircraft fasteners	1990 (TIMET)
Ti-13V-11Cr-3Al	B120VCA	Metastable	23	Airframe, landing gear, springs	1952 (RemCru)
Ti-1Al-8V-5Fe	37108	Metastable	19	Fasteners	1957 (RMI)
Ti-12Mo-6Zr-2Fe	TMZF	Metastable	18	Orthopedic implants	1992(Howmedica)
Ti-4.5Fe-6.8Mo-1.5Al	TIMETAL LCB	Metastable	18	Low cost, high strength alloy	1990 (TIMET)
Ti-15V-3Cr-1Mo-.5Nb-3Al	VT35	Metastable	16	High strength airframe castings	-(Russian)
Ti-3Al-8V-6Cr-4Mo-4Zr	Beta-C	Metastable	16	Oil-field, springs, fasteners	1969 (RMI)
Ti-15Mo	IMI 205	Metastable	15	Corrosion resistance	1958 (IMI)
Ti-8V-8Mo-2Fe-3Al	8-8-2-3	Metastable	15	High strength forgings	1969 (TIMET)
Ti–15Mo–2.6Nb–3Al–0.2Si	Beta 21S	Metastable	13	Oxidation/ corrosion resist, TMCs	1989 (TIMET)
Ti–15V–3Cr–3Sn–3Al	42078	Metastable	12	Sheet, plate airframe castings	1978 (USAF)
Ti–11.5Mo–6Zr–4.5Sn	Beta Ⅲ	Metastable	12	High strength	1969 (Crucible)
Ti–10V–2Fe–3Al	40212	Metastable	9.5	High strength forgings	1971 (TIMET)
Ti–5V–5Mo–1Cr–1Fe–5Al	VT22	Metastable	8	High strength forgings	(Russian)
Ti–5Al–2Sn–2Zr–4Mo–4Cr	Ti-17	Beta-rich	5.4	High strength, medium temperature	1968 (GEAE)
Ti–4.5Al–3V–2Mo–2Fe	SP700	Beta-rich	5.3	High strength, SPF	1989 (NKK)
Ti–5Al–2Sn–2Cr–4Mo–4Zr-1Fe	Beta CEZ	Beta-rich	5.1	High strength, medium temperature	1990(CEZUS)
Ti–13Nb–13Zr		Beta-rich	3.6	Orthopedic implants	1992 (Smith&Neph)

1.2.2 Phase constitution

It has been revealed that the mechanical properties of β-Ti alloys depend significantly on the presence of various phases in their microstructures [19,24]. These phases can be classified into equilibrium phases (α and β) and non-equilibrium or metastable phases (α', α" and ω), depending on the thermo-mechanical treatment.

1.2.2.1 The equilibrium phases

1.2.2.1.1 The β phase

The β phase exhibits bcc crystal structure and the space group of β phase is $Im\bar{3}m$ with two atoms at (0,0,0) and (1/2, 1/2, 1/2) coordinates [1]. The atomic unit cell of β phase is schematically shown in Fig. 1-5(a), with the most densely packed planes {110} highlighted. The close-packed directions are the <111> directions. The lattice parameter of pure β-Ti at 1173 K is a = 0.332 nm, as indicated. According to the reports, the lattice parameter of bcc-β phase varies with alloy composition [25,26]. The molybdenum concentration dependence of the lattice parameter of β phase is shown in Fig. 1-5(b) [25]. As mentioned before, the β phase stability also depends significantly on the alloy composition, and it is quantified with the value of $[Mo]_{eq}$. The various β phase stabilities result in different plastic deformation modes, which can be dislocation slip, deformation twinning, and stress-induced α" martensitic transformation. The details of the deformation mechanisms of β phase will be introduced in section 1.2.3.

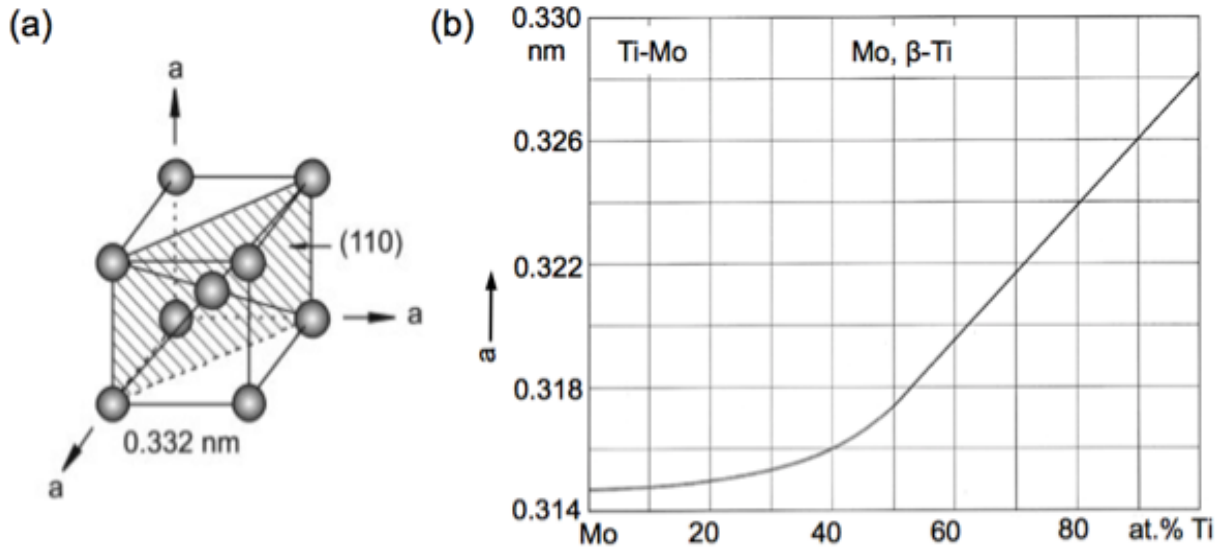

Fig. 1-5 (a) Crystal structure of bcc-β phase [1]. (b) Composition dependence of lattice parameter of bcc-β phase in Ti-Mo alloys [25].

1.2.2.1.2 The α phase

The α phase exhibits hcp crystal structure with the space group of $P6_3/mmc$. There are two atoms at (0, 0, 0) and (1/3, 2/3, 1/2) positions involved in per unit cell [1]. The atomic unit cell of α phase is schematically shown in Fig. 1-6(a). It can be observed in Fig. 1-6(a) that there are three most densely packed types of lattice planes, *i.e.*, {0001}, $\{\bar{1}010\}$ and $\{10\bar{1}1\}$. The three a_1, a_2, and a_3 axes are the close-packed directions with the indices of $<11\bar{2}0>$. The lattice parameter of pure α-Ti is a = 0.295 nm, and c = 0.468 nm.

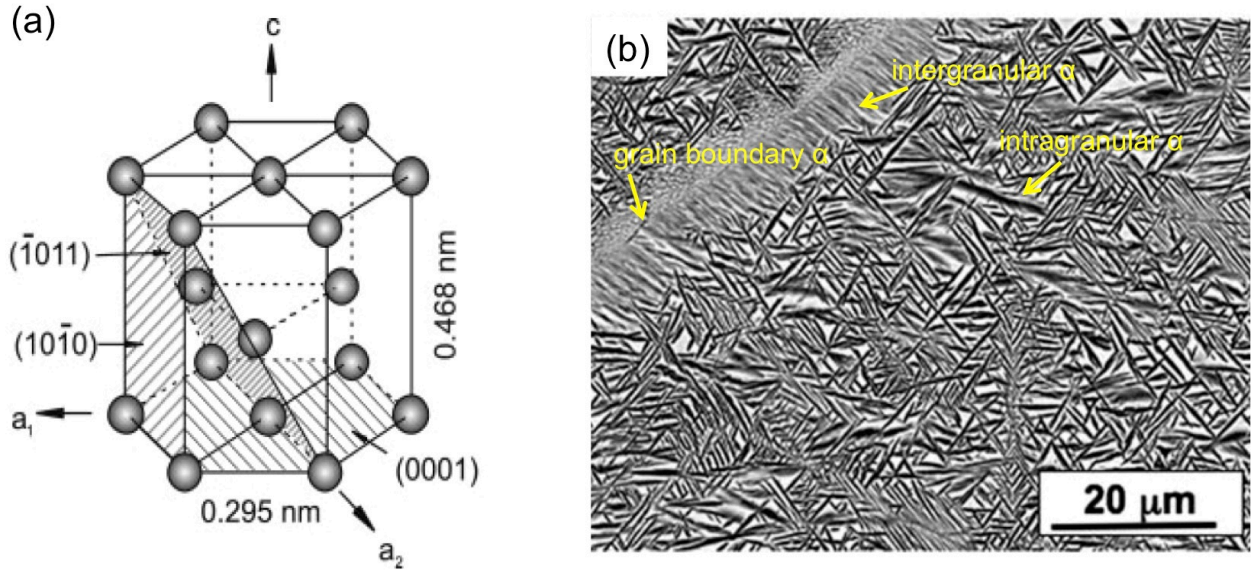

Fig. 1-6 (a) Crystal structure of hcp-α phase [1]. (b) Backscattered electron (BSE) image of Ti-5553 alloy after solution treatment (1273 K/60 min/water quenched) and aging (933 K/4 h/furnace cooled) [24].

The c/a ratio is 1.587. The α phase in β-Ti alloys is formed by means of β to α phase transformation, which is a diffusional process. It can be precipitated when the β-Ti alloys are quenched at low cooling rate from β phase region, or upon aging at α+β temperature region. The precipitated α phase can be classified into three types depending on the nucleation sites, including grain boundary α, intergranular α, and intragranular α phase. Fig. 1-6(b) shows an example of precipitated α phase in Ti-5Al-5Mo-5V-3Cr alloy [24]. The volume fraction, particle size, distribution and morphology of precipitate α phase can have pronounced effects on the mechanical properties of β-Ti alloys [4].

1.2.2.2 The non-equilibrium phases

1.2.2.2.1 The α' and α" martensite phases

There are two kinds of martensite phases in β-Ti alloys, namely, α' phase and α" phase. The α' phase has an hcp crystal structure, which is identical to α phase. On the other hand, the α" martensite has a disordered orthorhombic structure, belonging to the space group of Cmcm [27]. The martensite α'/α" phases are formed by martensitic transformation from β phase during rapid cooling/water quenching, *i.e.*, β → α'/α", depending on the amount of β-stabilizers [12,28,29]. The martensite structure changes from α' to α" when the

β-stabilizer content increases above a critical amount. For example, the α' is formed with Mo content up to about 6 wt.% in Ti-Mo binary alloys, as shown in Fig. 1-7 [12]. The α'/α" boundary for Ti-Ta binary alloys is about 20 wt.% Ta [28]. The α" martensite phase can also form in metastable β-Ti alloy by mechanical deformation, which provides additional mechanical driving force to trigger the martensitic transformation. The orthorhombic-α" martensite has been reported to play a key role in several mechanical properties of β-Ti alloys [12,30,31]. For example, the shape memory effect and superelasticity of Ti-Nb alloys are related with the reversible martensitic transformation between β phase and α" martensite phase [30,31]. Meanwhile, the orthorhombic-α" martensite leads to the Young's modulus of β-Ti alloys to the values close to human bones (~30 GPa), which is important for the design of advanced biomedical materials [12,32–34]. Furthermore, the stress-induced α" martensitic transformation (SIM α") contributes to the plasticity of β-Ti alloys with the effect of transformation induced plasticity (TRIP), similar to that in steel [35,36]. The details of the α" martensite phase will be given in the present study.

Extensive studies have been performed on the crystallography and morphology of α" martensite [28,37–39]. Fig. 1-8 shows a schematic illustration of the lattice correspondence between bcc-β and orthorhombic-α" martensite [39]. The face-centered tetragonal (fct) cell is further distorted to form the orthorhombic cell. The lattice parameter of the orthorhombic-α" martensite is $a_{\alpha''}$, $b_{\alpha''}$ and $c_{\alpha''}$, where $a_{\alpha''} < b_{\alpha''} < c_{\alpha''}$. The atom

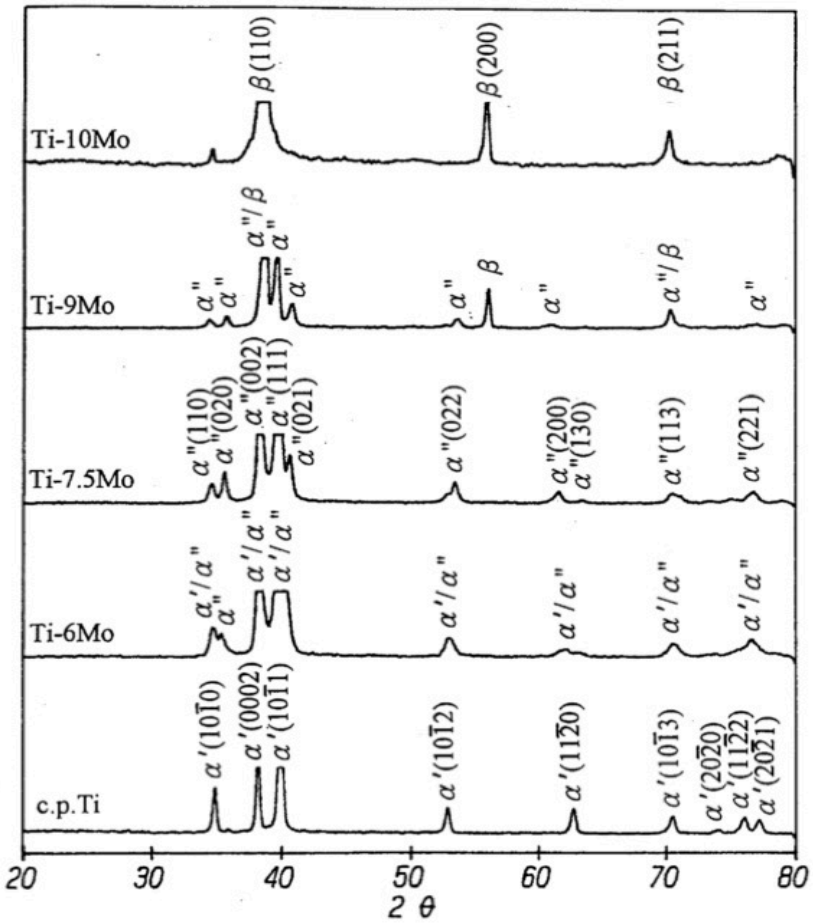

Fig. 1-7 X-ray diffraction pattern of c.p. Ti and Ti-Mo alloys [12].

positions are (0, 0, 0), (1/2, 1/2, 0), (0, 1-2y, 1/2), (1/2, 1/2-2y, 1/2). The atoms at the face-centered positions in the orthorhombic lattice are shifted to complete the β → α″ martensitic transformation, indicated by arrows in Fig. 1-8(b). The magnitude of this shift is y along the b-axis. According to previous reports [37,38], the orthorhombic-α″ structure in β-Ti alloys can be described as a transitional phase between the hcp-α' (y = 1/6) and bcc-β (y = 0) phases. The magnitude of δ in the α″ structure is restricted to $0 < \delta < 1/6$. The lattice parameters of orthorhombic-α" martensite vary with the alloy composition [29,40]. The lattice correspondence between β phase and α" martensite is as follows:

$$[100]_\beta \,//\, [100]_{\alpha''},\ [010]_\beta \,//\, 1/2[01\bar{1}]_{\alpha''},\ [001]_\beta \,//\, 1/2[011]_{\alpha''}$$

$$\text{or } [100]_{\alpha''} \,//\, [100]_\beta,\ [010]_{\alpha''} \,//\, 1/2[011]_\beta,\ [001]_{\alpha''} \,//\, 1/2[0\bar{1}1]_\beta$$

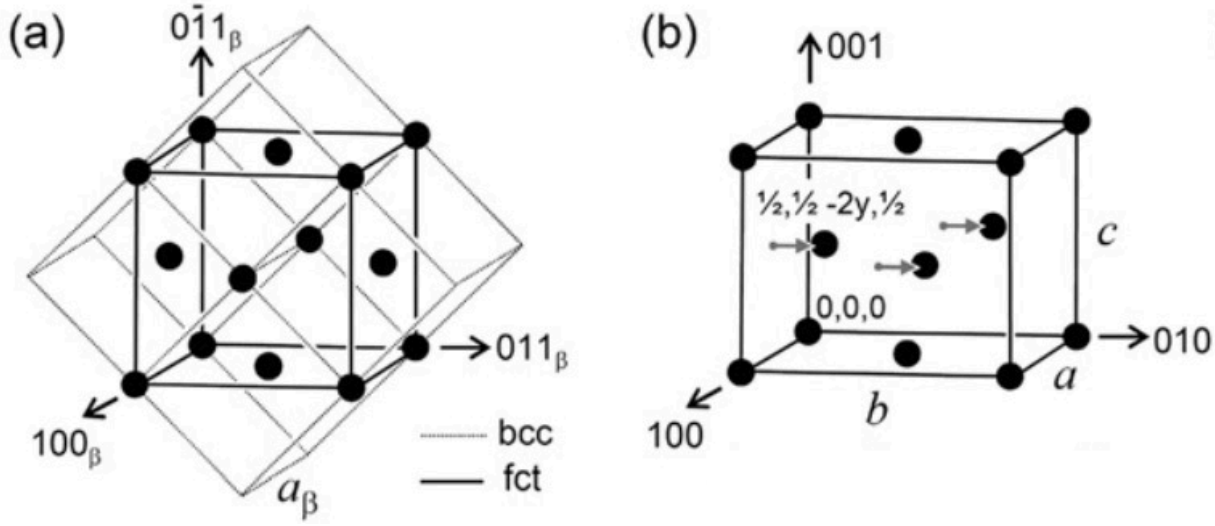

Fig. 1-8 Schematic illustration of the lattice correspondence between β and α" martensite [39].

The α" martensite in β-Ti alloys exhibits fine, acicular morphology. Fig. 1-9(a) and (b) show the optical micrographs of Ti-10Mo alloy with quenching induced α" martensite [41]. An internal twinning structure in α" martensite has been commonly reported, which is associated with the accommodation of the transformation strain from β to α" martensite [42]. Most of the literatures have claimed the internal twinning structure of α" martensite as $\{111\}_{\alpha''}$-type I twinning [41,43]. An example observed by transmission electron microscopy (TEM) is shown in Fig. 1-9(c), together with the analysis of selected area electron diffraction (SAED) pattern. Meanwhile, $<112>_{\alpha''}$-type II twinning and $\{110\}_{\alpha''}$-compound twinning, have been reported within α" martensite plate, depending on the lattice parameters of β and α" martensite phases [43].

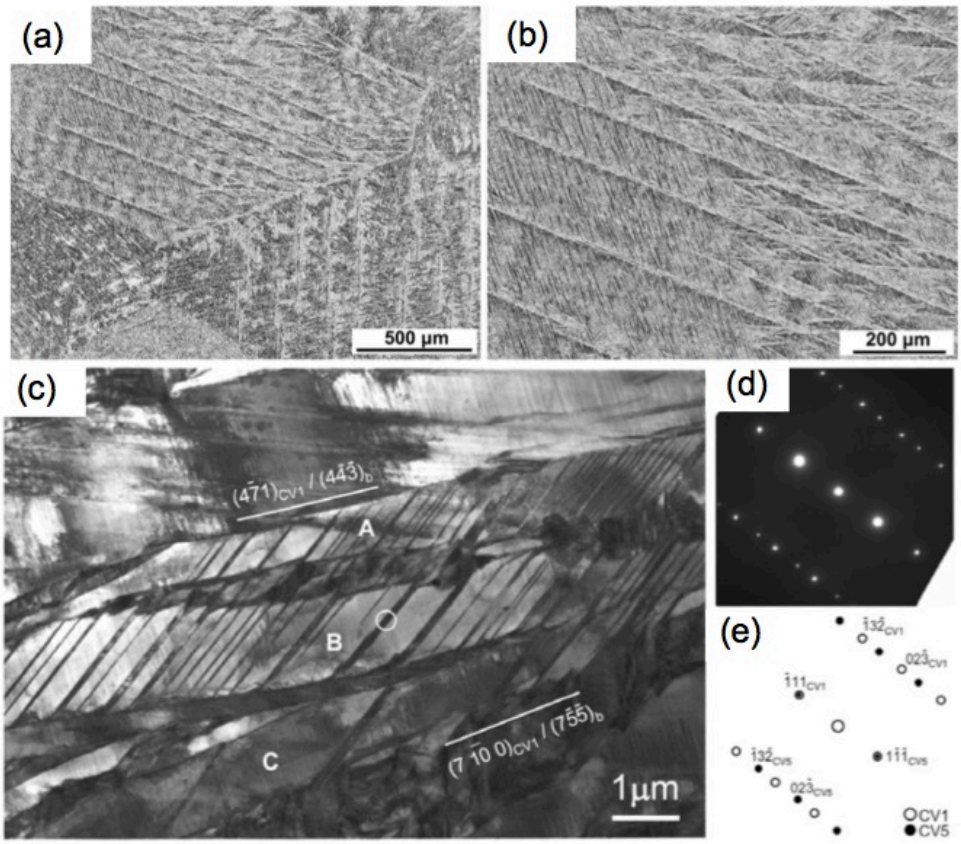

Fig. 1-9 (a), (b) Optical micrographs of Ti-10Mo showing the acicular α" martensite plates [41]. (c) Bright field (BF) image of typical twinning structure in α" martensite of Ti-16Nb-3Al alloy. (d) Selected area diffraction (SAD) pattern taken from the encircle region of (a). (c) Key diagram of (b) [39].

1.2.2.2.2 The ω phase

The crystal structure of the ω phase has been determined to be hexagonal with a space group of P6/mmm, or trigonal with a space group of P3m1, depending on the extent of transformation from β phase. The ω has a hexagonal symmetry upon the complete transformation, while a trigonal system after the incomplete transformation. The three atom positions in the cell are (0, 0, 0,), (2/3, 1/3, 1/2), and (1/3, 2/3, 1/2) for ideal hexagonal, and (0, 0, 0), (2/3, 1/3, 1/2+*z*), and (1/3, 2/3, 1/2-*z*) (0< *z* <0.167) for trigonal structure. The ω phase is formed by collapsing one pair of planes to the intermediate position, leaving the next plan unaltered and collapsing the next pair and so on. The atomic movements required are $\pm a_\beta\sqrt{3}/12$ or equivalently $\pm c_\omega/6$ for a complete transformation. For a partial collapse (atomic movement < $a_\beta\sqrt{3}/12$), the trigonal ω is obtained. In addition, as there are 4 equivalent bcc $<111>_\beta$ axes, the ω phase can nucleate in 4 variants with the following orientation relationship

$$<111>_\beta \,//\, <0001>_\omega \qquad \text{and} \qquad \{1\bar{1}0\}_\beta \,//\, \{11\bar{2}0\}_\omega$$

Generally, ω phase in the β-Ti alloys can be classified into 3 types depending on their formation mechanisms, *i.e.*, athermal ω (ω_{ath}), isothermal ω (ω_{iso}), and deformation-induced ω phase [44]. The ω_{ath} precipitates upon fast cooling from the high temperature β region in β-Ti alloy with sufficient β-stabilizer.

The morphology of ω_{ath} precipitates exhibits an ellipsoidal shape with 2-10 nm in the diameter. A typical TEM image of ω_{ath} is illustrated in Fig. 1-10 (a) [45]. The ω_{iso} is formed during aging process at the temperature range of 373-773 K. Furthermore, the size and volume fraction of ω_{iso} increase with increasing the holding time and decrease with the quenching rate. The ω_{iso} precipitates can be either ellipsoidal or cuboidal in terms of lattice misfits (Fig. 1-10(b) and (c)) [4]. The ω_{iso} has been proved with remarkable effect on the mechanical properties, especially increasing the hardness of β-Ti alloys [46]. Extensive studies have reported the deformation-induced ω phases in β-Ti alloys upon deformation at room temperature and shock loading [44,47,48]. It generally displays plate-like morphology (Fig. 1-10(d)) [49].

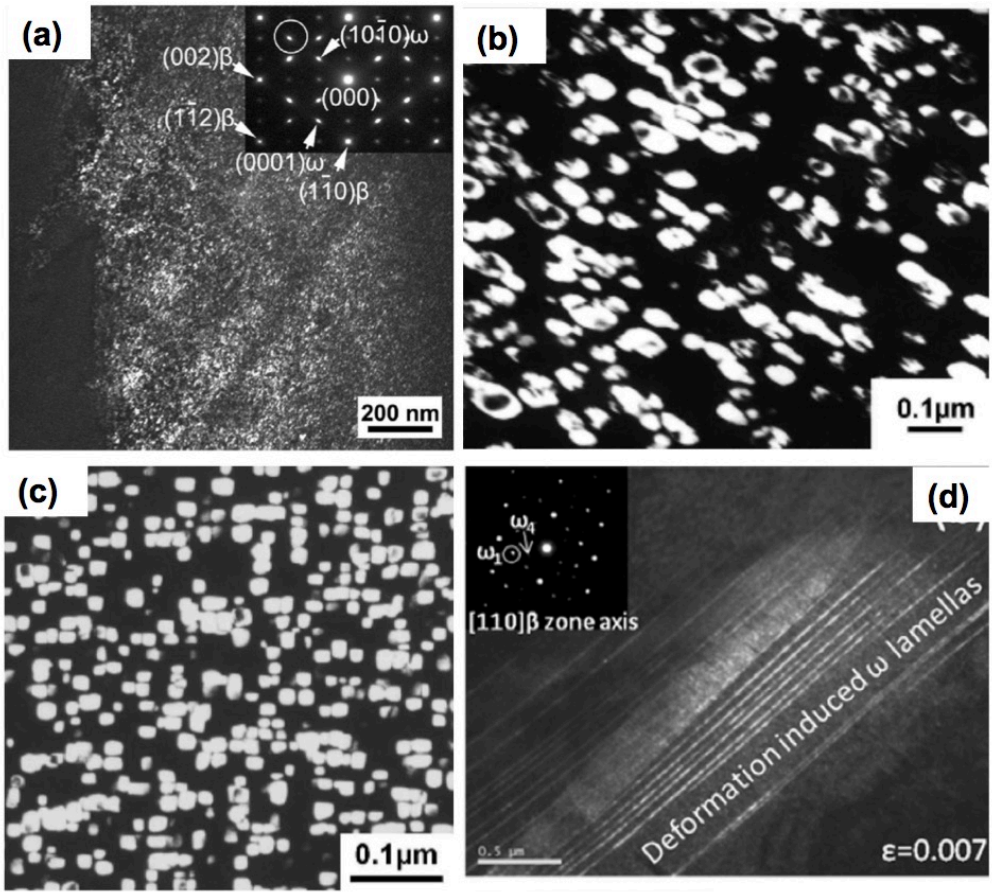

Fig. 1-10 (a) Dark field (DF) TEM image of ω_{ath} in air-cooled Ti-10Mo alloy [45]. (b) DF of ellipsoidal ω_{iso} in aged Ti-16Mo alloy. (c) DF of cuboidal ω_{iso} in aged Ti-8Fe alloy [4]. (d) DF of deformation-induced ω plates in Ti-12Mo alloy [49].

1.2.3 Deformation mechanisms

The plastic deformation of metals and alloys involves various mechanisms such as dislocation slip, deformation twinning, stress-induced martensitic transformation, or a combination of these. The deformation mechanisms in β-Ti alloys with mainly bcc-β phase have been widely studied, which mainly vary from stress-induced martensitic transformation to $\{332\}\langle 113\rangle_\beta$ twinning and then to dislocation slip as the β phase stability increases, as shown in Fig. 1-11 [19,20,50]. Stress-induced α″ martensite (SIM α″) is the

dominant deformation mode when the $[Mo]_{eq}$ is in the range of 7.4-12, $\{332\}<113>_{\beta}$ twinning for 10-18 wt.% $[Mo]_{eq}$, and dislocation slip for $[Mo]_{eq} > 20$ [19]. For the β-rich Ti alloys with mainly orthorhombic-α" martensite phase, the deformation twinning and dislocation slip have been reported [51,52]. However, the mechanisms of these deformation behaviors in α" martensite are still not clear. On the other hand, the interplay between the different deformation mechanisms significantly affects the mechanical properties of the materials.

1.2.3.1 Deformation mechanisms of bcc-β phase

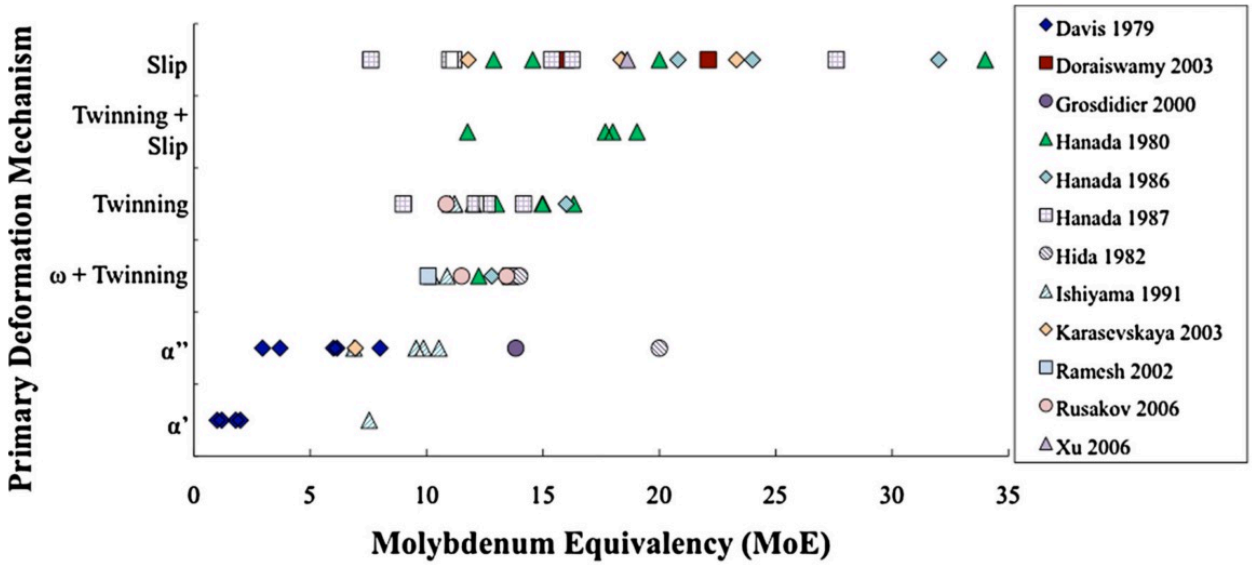

Fig. 1-11 The experimental results reported for the deformation mechanisms as function of Mo equivalency in β-Ti alloy [19].

1.2.3.1.1 Stress-induced α" martensitic transformation

Stress-induced α" martensitic transformation (SIM α") has been reported to take place in the less stabilized β phase, as indicated in Fig. 1-11 [19]. The crystal structure of α" martensite and the lattice correspondence between β phase and α" phase have been well introduced in the section of 1.2.2.2.1. Additionally, the triggering stress for the SIM α" transformation in metastable β-Ti alloys has been reported to depend on (i) the chemical composition in β phase (or the β phase stability), (ii) the testing temperature, and (iii) the microstructure of the alloy [19]. For example, the yield stress is observed to increase with increasing the β phase stability and decreasing the α" volume fraction in Ti-Nb-Si alloys [53]. Also, the triggering stress for SIM α" has been reported to increase with increasing β grain size up to 300 μm in Ti-10V-2Fe-3Al alloy [54]. Most importantly, the SIM α" transformation is great interest for biomedical and micromechanics applications because of the resulting shape-memory effect and pseudo-elastic behavior [55]. Furthermore, the SIM α" is suggested as a good candidate for reaching a better balance of strength and ductility properties of β-Ti alloys, similar to the TRIP steels [36,56].

1.2.3.1.2 {332}<113>$_\beta$ deformation twinning

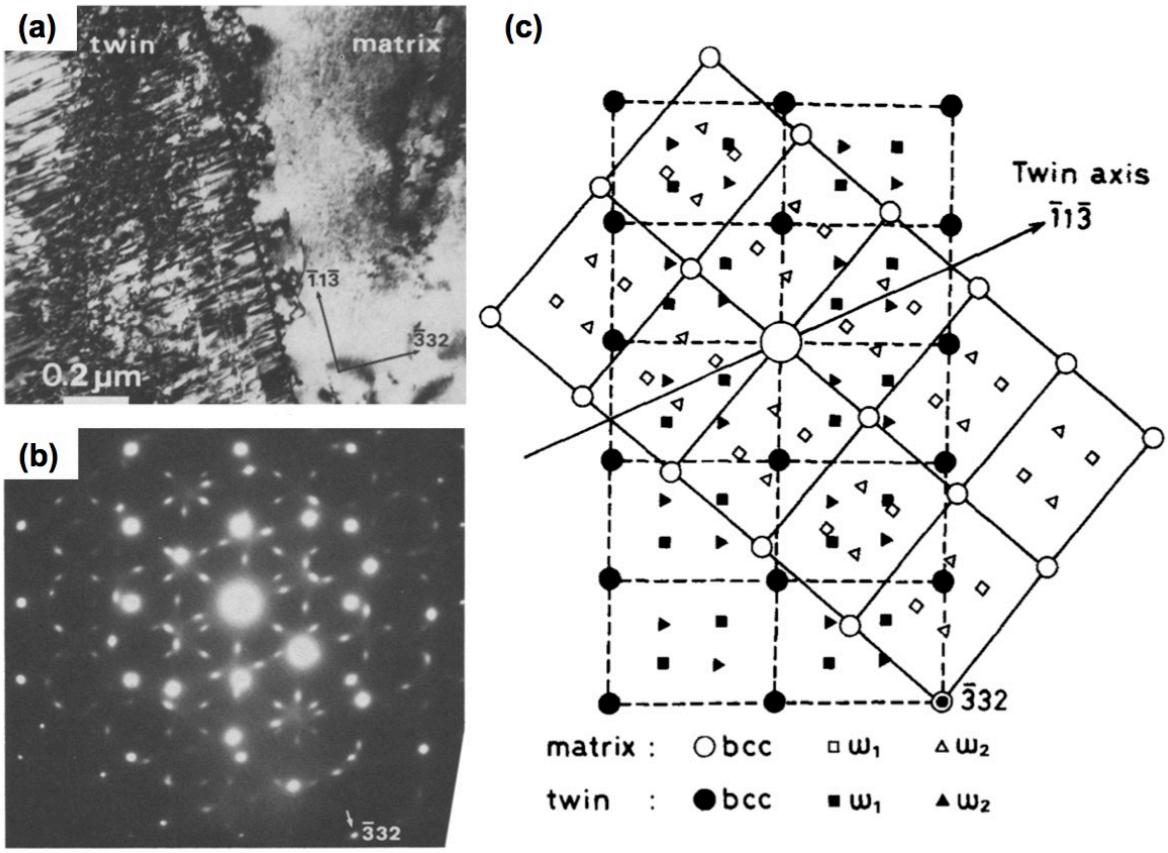

Fig. 1-12 (a) TEM-BF image of $(\bar{3}32)[\bar{1}1\bar{3}]$ twin in Ti-22V alloy after tension. (b) The corresponding SAD pattern with electron beam // [110]. (c) Schematic diffraction pattern of (b) [58].

The bcc metals and alloys usually deform by the well-known twinning mode of {112}<111>$_\beta$. However, a unique twinning mode, {332}<113>$_\beta$ twinning has been reported in β-Ti alloys such as Ti-Nb [57], Ti-V (Fig. 1-12) [58], and Ti-Mo (Fig. 1-13) [50] alloys with the reduced amount of β-stabilizers. Fig. 1-12 shows the TEM images and SAD patterns of {332}<113>$_\beta$ twinning structure in Ti-22V alloy. It has been reported that the boundaries of {332}<113>$_\beta$ twins with a misorientation angle of 50.48° along the <110>$_\beta$ direction [59], which is very important for identification of {332}<113>$_\beta$ twins with EBSD analysis (Fig. 1-13 [50]).

The decreasing of the β-stabilizers results in the low shear modulus c' ($(c_{11}-c_{12})/2$), which reflects the resistance to the shear of {110}$_\beta$ planes along <110>$_\beta$ directions. This suggests that the lattice instability of bcc-β phase contributes to the activation of {332}<113>$_\beta$ twinning. Meanwhile, Hanada *et al.* [58] proposed that the {332}<113>$_\beta$ twinning is closely related to the stability of β phase with respect to athermal ω phase, which is introduced through quenching. Unlike the {112}<111>$_\beta$ twinning mode, in which only atomic shearing is necessary for the twin formation, the {332}<113>$_\beta$ twinning mode requires not only shearing, but one-half of the atoms much shuffle to their twin positions. Several models of the atomic movements required in {332}<113>$_\beta$ twinning have been promoted [60–62]. For example, Tobe *et al.* [60] have considered the lattice instability in bcc-β by proposing a modulated structure with base-centered tetragonal symmetry. They

clarified the atomic movement (shearing and shuffling) in the formation of $\{332\}<113>_{\beta}$ twinning with the theory of crystallography of deformation twinning proposed by Bilby and Crocker [42,63].

Several studies revealed that the activation of $\{332\}<113>_{\beta}$ twinning in β-Ti alloys resulted in a significant work-hardening rate and improved ductility, similarly to the twinning-induced plasticity (TWIP) effect in steels [20,50,64]. The mechanism of work-hardening in TWIP alloys is now well-explained with a dynamic Hall-Petch effect induced by the deformation twins [64]. The twin boundary is acting as the strong barrier for the dislocation glide, and the increasing number of twin defects results in a continuous reduction of dislocation mean free path, leading to the rise of strength. Min *et al.* [64] offered a quantitative evaluation of $\{332\}<113>_{\beta}$ twinning contributing to work hardening in Ti-15Mo alloy. Thus the understanding of TWIP effect in terms of $\{332\}<113>_{\beta}$ twinning is of great importance for improving the combination of strength and ductility.

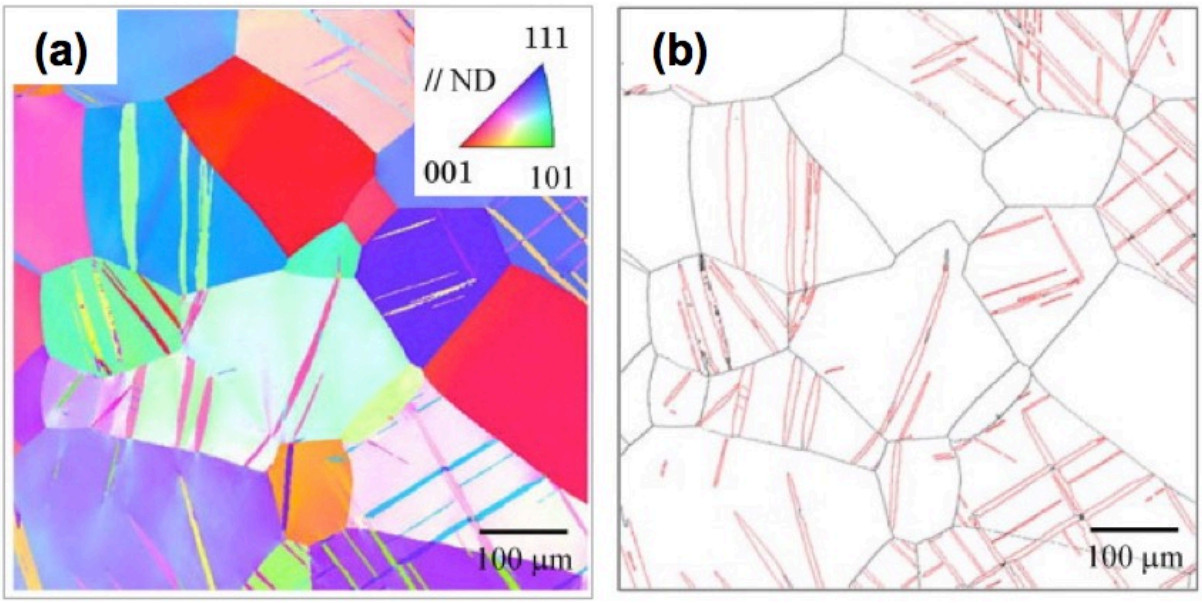

Fig. 1-13 EBSD maps of Ti–10Mo–2Fe alloy after tensile strain of 4%. (a) Inverse pole figures (IPF) map for the ND. (b) Boundary map. The red line with a misorientation angle of 50.48° along the (110) direction corresponding to the $\{332\}<113>_{\beta}$ twins [50].

1.2.3.1.3 Dislocation slip

The bcc-β phase can deform by dominant dislocation slip with the high concentration of β phase stabilizers [19]. The slip systems in bcc structure are well understood. The slip system usually operates on the most densely packed planes, *i.e.*, $\{110\}_{\beta}$ planes. In addition, the slip systems on the $\{112\}_{\beta}$ and $\{123\}_{\beta}$ planes are also observed, all with the Burgers vector of $<111>_{\beta}$ [65]. In general, deformation mainly by dislocation slip results in relatively high yield strength, comparatively low work-hardening rate, and low elongation when compared with lower β stabilized alloys deforming mainly by $\{332\}<113>_{\beta}$ twinning, as shown in Fig. 1-14 [20]. Therefore, the deformation mode of dislocation slip is also playing an important role in the improvement of mechanical properties of β-Ti alloys. For example, Min *et al.* [50] reported in

Ti-Mo-based alloys that the combination of deformation modes, *i.e.*, {332}<113>$_{\beta}$ twinning and slip, can enhance the uniform elongation while maintaining high strength.

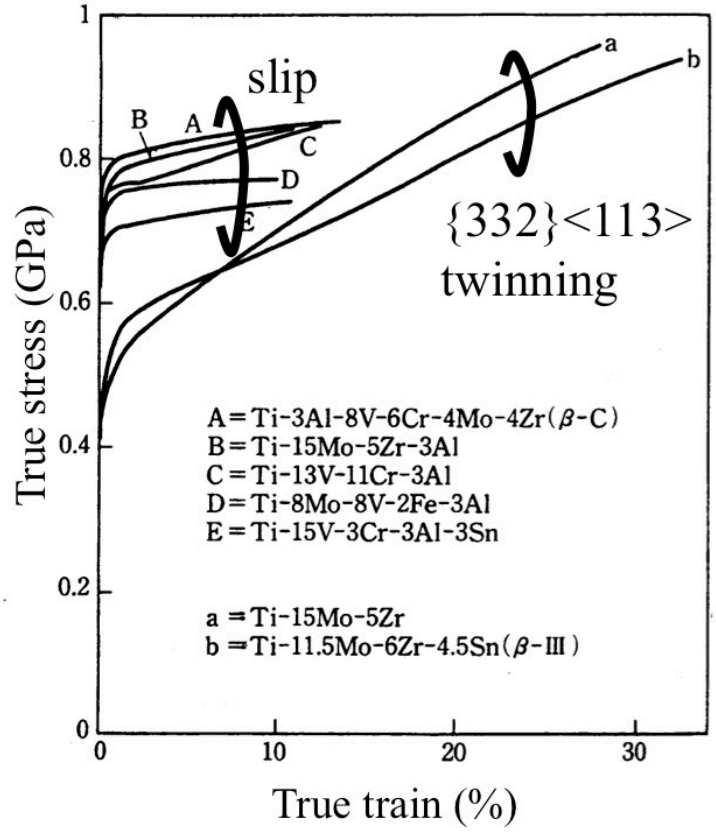

Fig. 1-14 True stress-strain curves for as-quenched commercial β-Ti alloys with different β phase stabilities [20].

1.2.3.2 Deformation mechanisms of orthorhombic-α" martensite

The orthorhombic-α" martensite has been reported to play a key role in the characteristic mechanical properties of β-Ti alloys, such as the shape memory effect, superelasticity, and low Young's modulus [30,37,40]. For example, the shape memory effect and superelasticity of Ti-Nb alloys are associated with the reversible martensitic transformation [30,31]. Thus, extensive studies have been focused on the microstructure and crystallography of the α" martensite. The crystal structure of α" martensite is similar to that of α-uranium, and both have an orthorhombic structure. Furthermore, the plastic deformation of α-uranium has been investigated, including the twinning and dislocation slip [66,67]. However, the plastic deformation mechanism of α" martensite phase has not been well studied.

Recently, Bertrand *et al*. [51] have reported that the α" martensite in Ti-25Ta-20Nb (wt.%) alloy deforms by plastic twinning with a {130}<310>$_{\alpha"}$ twinning system, as shown in Fig. 1-15. It has also been identified in Ti-27Nb (at.%) alloy [68]. This twinning system has been reported with a strong correspondence with the {332}<113>$_{\beta}$ twinning in the bcc-β phase. Besides, Ping *et al*. [52] have found the deformation twinning of {110}$_{\alpha"}$-type I in a Ti-40Nb (wt.%) alloy, which involves the smallest shear

magnitude during the twin formation. This result consistent with the crystallographic analysis of deformation twinning proposed by Bilby and Crocker [63,69]. The deformation twinning system is suggested to depend on the lattice parameters of α" martensite, which changes significantly with the alloy composition. Therefore, like the various twinning systems reported in α-uranium, there is a high possibility of other deformation twinning systems existing in the α" martensite of β-Ti alloys. Nevertheless, there is still a lack of knowledge on the deformation mechanisms of α" martensite.

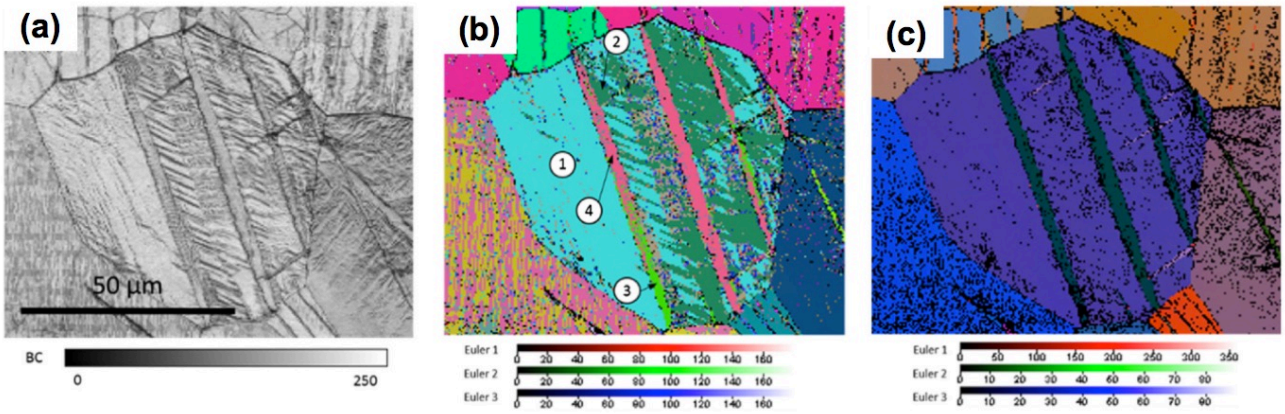

Fig. 1-15 EBSD maps of Ti-25Ta-20Nb alloy strained until 6%: (a) band contrast (BC). (b) Euler angles obtained from indexation with the α" phase and (c) Euler angles obtained from indexation with the β phase [51].

1.3 Ti-Mo alloys

The minimum concentrations of the β-stabilizers, Mo, Nb, and Ta to retain the fully β phase upon quenching are 10, 22 and 70 wt.%, respectively for Ti-Mo [12], Ti-Nb [29], and Ti-Ta [28] alloys. Therefore, Ti–Mo alloys have received much attention because of the remarkable β-stabilizing effect and the favorable safety of Mo. Extensive fundamental studies have been carried out on the microstructure and mechanical properties of Ti-Mo alloys [12,13,36]. As mentioned before, Ho *et al*. [12] studied the microstructure of Ti-Mo binary alloys after water quenching and found that α' martensite was formed in the alloy containing Mo < 6 wt.%, α″ martensite in 6~10 wt.% Mo, and the retained β phase became dominant when Mo exceed 10 wt.%, as shown in Fig. 1-16. Sun *et al*. [36] have reported pronounced work-hardening in Ti-12Mo alloy which combines deformation modes of SIM α″ and $\{332\}\langle 113\rangle_\beta$ twinning. With the superior properties such as low Young's modulus, good balance of strength and ductility, excellent biocompatibility, Ti-Mo alloys as biomaterials have been studied [70,71]. Up to now, Ti-7.5Mo [12,13] and Ti-15Mo [14] alloys have been developed with low Young's modulus. Besides, Ti-15Mo alloy exhibits an extremely high crevice corrosion resistance in seawater at a high temperature of 373K. Recently, the Ti-7.5Mo alloy has been reported with much lower Young's modulus (~65 GPa) [14]. Furthermore, Lin *et al*. [18] reported that a greater amount of new bone was formed at the Ti-7.5Mo alloy than the Ti-6Al-4V alloy after implantation in the rabbit femur, Fig. 1-17, which indicates good bone-implant interaction of Ti-7.5Mo alloy. Therefore, the

Ti-7.5Mo alloy has been described as a promising candidate for implant material and it is attracting more and more research attentions.

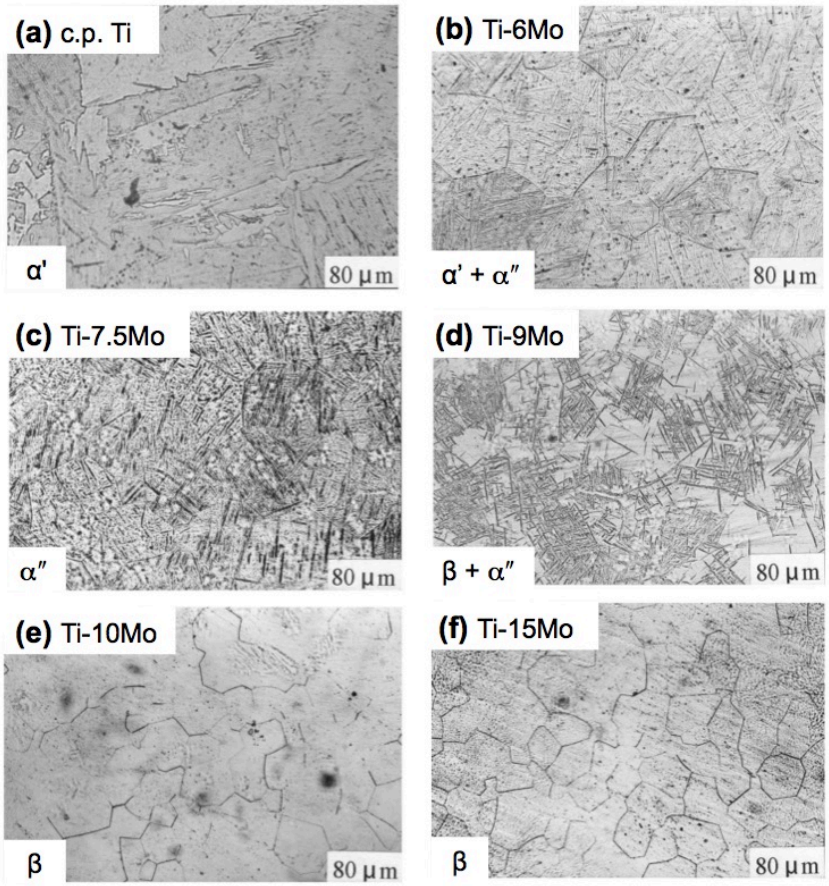

Fig. 1-16 Optical micrographs of as-quenched Ti-Mo binary alloys with different Mo contents. These alloys are composed of different phases, as indicated in the image [12].

Furthermore, various alloying elements were added in Ti-Mo-based alloys to improve the mechanical properties and shape memory effect of the binary alloys. Min *et al*. [72] have developed a series of Ti-Mo-Fe alloys by replacing the costly Mo content with Fe element, which is also an effective β-stabilizer. They reported a Ti-10Mo-2Fe alloy that exhibited a considerable balance between strength and ductility by combining the deformation modes of $\{332\}<113>_{\beta}$ twinning and slip [72]. Besides, the superelasticity and shape memory effect have been found in Ti-Mo-Ag [73], Ti-Mo-Sn [73] and Ti-Mo-Ga [74] alloys. They have been developed as Ni-free superelasticity and shape memory alloys that could replace Ti-Ni, which has been suspected of producing allergenic and carcinogenic reactions from the Ni content.

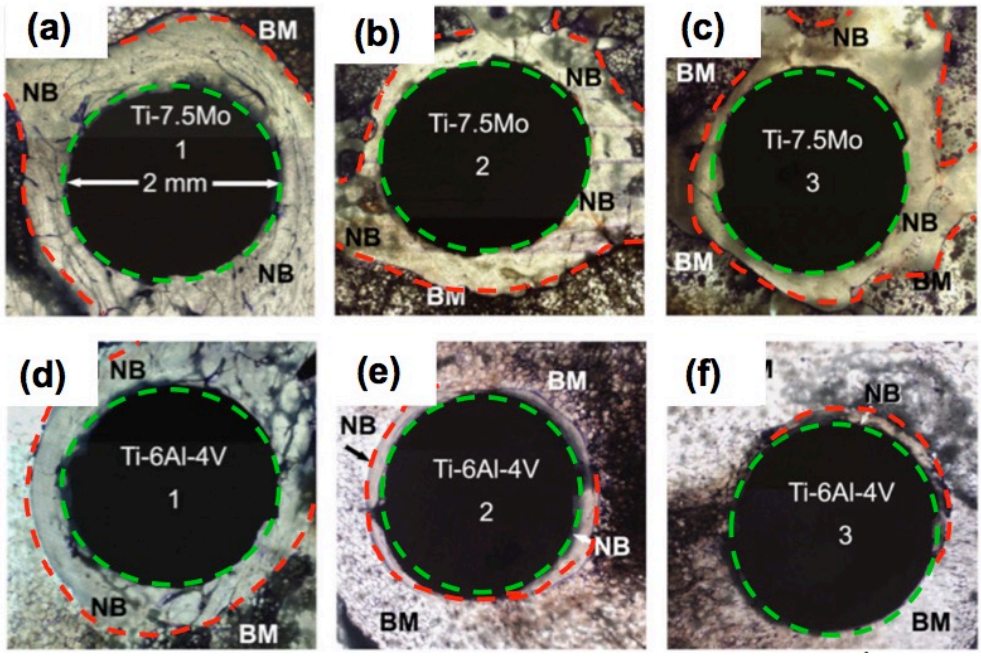

Fig. 1-17 An overview of new bone formation on major parts of the implant within the femur of rabbits, including Ti-7.5Mo (a)-(c) and Ti-6Al-4V (d)-(f). NB and BM indicate the new bone and bone marrow, respectively [18].

1.4 Research aim and scope

It is widely acknowledged that the mechanical properties of metals and alloys depend significantly on the deformation mechanisms such as stress-induced martensitic transformation, deformation twinning, and dislocation slip. Literatures show that deformation mechanisms of β-Ti alloys containing bcc-β phase are widely studied. However, there is not enough study focused on the mechanisms of plastic deformation of orthorhombic-α″ martensite, which is also important for the improvement of mechanical properties of β-Ti alloys. Meanwhile, the recently developed Ti-7.5Mo alloy with low Young's modulus and good biocompatibility great potential for biomedical applications is regarded as a promising candidate for implant material. However, the Ti-7.5Mo alloy with fully α" martensite exhibits the main drawback of relatively low mechanical strength compared to other β-Ti alloys with bcc-β phase [17]. It is widely recognized that the deformation mechanisms significantly influence the mechanical properties of β-Ti alloys with bcc-β phase [19,20]. Thus, a better understanding of the deformation behaviors of α" martensite is suggested essential for the improvement of mechanical properties of Ti-7.5Mo alloy and other β-Ti alloys with α" martensite. Meanwhile, it is well established that the mechanical properties of titanium alloys are sensitively dependent on the interstitial solutes such as oxygen, nitrogen, carbon, and hydrogen [7,21,75]. Extensive efforts have revealed oxygen as an effective element to improve the strength of titanium alloys due to its solid-solution strengthening effect [75,76]. However, the influences of oxygen on the properties of orthorhombic-α" martensite in Ti-Mo alloys are still not clear.

As a unique twin mode in bcc metals and alloys, β_β twinning has been frequently observed in Ti-Mo, Ti-Nb, Ti-V and Ti-Cr alloys [19,58,77]. Several studies have revealed that the $\{332\}<113>_\beta$ twinning in

β-Ti alloys results in a high work-hardening rate and improved ductility, similar to the TWIP steels [36,78]. The mechanism of pronounced work-hardening induced by the twinning can be well-explained by a dynamic Hall-Petch effect [79]. Some investigations revealed that the mechanical properties and deformation mechanisms of β-Ti alloys have a strong dependence on the strain rate [77,80,81]. However, there is a lack of understanding regarding the mechanism of strain rate dependence of work-hardening behavior in β-Ti alloys, in particular, about the effect of $\{332\}<113>_{\beta}$ twinning.

Therefore, the present thesis firstly focused on deformation mechanisms of as-quenched α" martensite in the Ti-7.5Mo alloy. The experimental observations and crystallographic analysis were performed. Then, in order to improve the strength while keeping the low Young's modulus of the Ti-7.5Mo alloy, the effect of oxygen content on the microstructure and mechanical properties of the Ti-7.5Mo alloy have been investigated. The last part of the thesis was to investigate the effect of strain rate on the tensile deformation behaviors in a β-Ti alloy showing TWIP effect. We focused on a Ti-10Mo-1Fe (wt.%) alloy which deforms mainly by $\{332\}<113>_{\beta}$ twinning [50]. The work hardening behavior was investigated by monotonic tensile tests at different strain rates ranging from $2.8x10^{-5}$ s^{-1} to $2.8x10^{-1}$ s^{-1}. The correlation between the work-hardening behavior and microstructure evolution was discussed.

References

[1] C. Leyens, M. Peters, Titanium and Titanium Alloys, Wiley Online Library, 2003.
[2] G. Welsch, R. Boyer, E.W. Collings, Materials Properties Handbook: Titanium Alloys, in: G. Welsch, R. Boyer, E.W. Collings (Eds.), Mater. Prop. Handb. Titan. Alloy., ASM International, 1993: pp. 5–11.
[3] V.A. Joshi, Titanium alloys: An atlas of structures and fracture features, 2006.
[4] G. Lütjering, J.C. Williams, Titanium, Springer Berlin Heidelberg New York, 2003.
[5] H. Duan, H. Xu, W. Su, Y. Ke, Z. Liu, H. Song, Effect of oxygen on the microstructure and mechanical properties of Ti-23Nb-0.7Ta-2Zr alloy, Int. J. Miner. Metall. Mater. 19 (2012) 1128–1133.
[6] M. Besse, P. Castany, T. Gloriant, Mechanisms of deformation in gum metal TNTZ-O and TNTZ titanium alloys: A comparative study on the oxygen influence, Acta Mater. 59 (2011) 5982–5988.
[7] I.I. Kornilov, Effect of oxygen on titanium and its alloys, Met. Sci. Heat Treat. 15 (1974) 826–829.
[8] P.J. Bania, Beta titanium alloys and their role in the titanium industry, JOM. 46 (1994) 16–19.
[9] D. Eylon, A. Vassel, Y. Combres, R.R. Boyer, P.J. Bania, R.W. Schutz, Issues in the development of beta titanium alloys, Jom. 46 (1994) 14–15.
[10] J.D. Cotton, R.D. Briggs, R.R. Boyer, S. Tamirisakandala, P. Russo, N. Shchetnikov, J.C. Fanning, State of the Art in Beta Titanium Alloys for Airframe Applications, Jom. 67 (2015) 1281–1303.
[11] R.M. Pilliar, Modern metal processing for improved load-bearing surgical implants, Biomaterials. 12 (1991) 95–100.
[12] W.F. Ho, C.P. Ju, J.H. Chern Lin, Structure and properties of cast binary Ti–Mo alloys, Biomaterials. 20 (1999) 2115–2122.
[13] W.F. Ho, A comparison of tensile properties and corrosion behavior of cast Ti-7.5Mo with c.p. Ti, Ti-15Mo and Ti-6Al-4V alloys, J. Alloys Compd. 464 (2008) 580–583.
[14] L. Zardiackas, D. Mitchell, J. Disegi, Characterization of Ti-15Mo Beta Titanium Alloy for Orthopaedic Implant Applications, in: Med. Appl. Titan. Its Alloy. Mater. Biol. Issues, ASTM International, 100 Barr Harbor Drive, PO Box C700, West Conshohocken, PA 19428-2959, 1996: pp. 60–75.
[15] K. Wang, The use of titanium for medical applications in the USA, Mater. Sci. Eng. A. 213 (1996) 134–137.
[16] D. Kuroda, M. Niinomi, M. Morinaga, Y. Kato, T. Yashiro, Design and mechanical properties of new β type titanium alloys for implant materials, Mater. Sci. Eng. A. 243 (1998) 244–249.

[17] C.C. Chung, S.W. Wang, Y.C. Chen, C.P. Ju, J.H. Chern Lin, Effect of cold rolling on structure and tensile properties of cast Ti-7.5Mo alloy, Mater. Sci. Eng. A. 631 (2015) 52–66.
[18] D.J. Lin, C.C. Chuang, J.H. Chern Lin, J.W. Lee, C.P. Ju, H.S. Yin, Bone formation at the surface of low modulus Ti–7.5Mo implants in rabbit femur, Biomaterials. 28 (2007) 2582–2589.
[19] R.P. Kolli, W.J. Joost, S. Ankem, Phase Stability and Stress-Induced Transformations in Beta Titanium Alloys, JOM. 76 (2015) 1273–1280.
[20] S. Hanada, O. Izumi, Correlation of tensile properties, deformation modes, and phase stability in commercial β-phase titanium alloys, Metall. Trans. A. 18 (1987) 265–271.
[21] H. Conrad, Effect of interstitial solutes on the strength and ductility of titanium, Prog. Mater. Sci. 26 (1981) 123–403.
[22] E.W. Collins, J.C. Ho, H.L. Gegel, Solid Solution Strengthening and Fundamental Design of Titanium Alloys, 1972.
[23] A. Ramarolahy, P. Castany, F. Prima, P. Laheurte, I. Péron, T. Gloriant, Microstructure and mechanical behavior of superelastic Ti-24Nb-0.5O and Ti-24Nb-0.5N biomedical alloys, J. Mech. Behav. Biomed. Mater. 9 (2012) 83–90.
[24] S. Nag, R. Banerjee, R. Srinivasan, J.Y. Hwang, M. Harper, H.L. Fraser, ω-Assisted nucleation and growth of α precipitates in the Ti-5Al-5Mo-5V-3Cr-0.5Fe β titanium alloy, Acta Mater. 57 (2009) 2136–2147.
[25] B. Predel, Mo-Ti, in: O. Madelung (Ed.), Landolt-Börnstein - Gr. IV Phys. Chem., Springer Berlin Heidelberg, Berlin/Heidelberg, 1997: pp. 1–3.
[26] X.H. Min, P.F. Bai, S. Emura, X. Ji, C. Cheng, B. Jiang, K. Tsuchiya, Effect of oxygen content on deformation mode and corrosion behavior in β-type Ti-Mo alloy, Mater. Sci. Eng. A. 684 (2017) 534–541.
[27] A.R.G. Brown, D. Clark, J. Eastabrook, K.S. Jepson, The Titanium–Niobium System, Nature. 201 (1964) 914–915.
[28] Y.L. Zhou, M. Niinomi, T. Akahori, Effects of Ta content on Young's modulus and tensile properties of binary Ti-Ta alloys for biomedical applications, Mater. Sci. Eng. A. 371 (2004) 283–290.
[29] M. Bönisch, M. Calin, T. Waitz, A. Panigrahi, M. Zehetbauer, A. Gebert, W. Skrotzki, J. Eckert, Thermal stability and phase transformations of martensitic Ti–Nb alloys, Sci. Technol. Adv. Mater. 14 (2013) 55004.
[30] H.Y. Kim, Y. Ikehara, J.I. Kim, H. Hosoda, S. Miyazaki, Martensitic transformation, shape memory effect and superelasticity of Ti–Nb binary alloys, Acta Mater. 54 (2006) 2419–2429.
[31] H.Y. Kim, S. Hashimoto, J. Il Kim, H. Hosoda, S. Miyazaki, Mechanical Properties and Shape Memory Behavior of Ti-Nb Alloys, Mater. Trans. 45 (2004) 2443–2448.
[32] Y.L. Hao, S.J. Li, S.Y. Sun, C.Y. Zheng, Q.M. Hu, R. Yang, Super-elastic titanium alloy with unstable plastic deformation, Appl. Phys. Lett. 87 (2005) 2003–2006.
[33] S. Cai, J.E. Schaffer, Y. Ren, Deformation of a Ti-Nb alloy containing ??-martensite and omega phases, Appl. Phys. Lett. 106 (2015) 1–6.
[34] H. Matsumoto, S. Watanabe, S. Hanada, Beta TiNbSn Alloys with Low Young's Modulus and High Strength, Mater. Trans. 46 (2005) 1070–1078.
[35] I. Gutierrez-Urrutia, D. Raabe, Multistage strain hardening through dislocation substructure and twinning in a high strength and ductile weight-reduced Fe–Mn–Al–C steel, Acta Mater. 60 (2012) 5791–5802.
[36] M. Marteleur, F. Sun, T. Gloriant, P. Vermaut, P.J. Jacques, F. Prima, On the design of new β-metastable titanium alloys with improved work hardening rate thanks to simultaneous TRIP and TWIP effects, Scr. Mater. 66 (2012) 749–752.
[37] S. Banumathy, R.K. Mandal, A.K. Singh, Structure of orthorhombic martensitic phase in binary Ti-Nb alloys, J. Appl. Phys. 106 (2009).
[38] C.X. Li, H. Bin Luo, Q.M. Hu, R. Yang, F.X. Yin, O. Umezawa, L. Vitos, Lattice parameters and relative stability of α″ phase in binary titanium alloys from first-principles calculations, Solid State Commun. 159 (2013) 70–75.
[39] T. Inamura, H. Hosoda, H.Y. Kim, S. Miyazaki, Antiphase boundary-like stacking fault in alpha''-martensite of disordered crystal structure in beta-titanium shape memory alloy, Philos. Mag. 90 (2010) 3475–3498.
[40] H.Y. Kim, S. Miyazaki, Martensitic Transformation and Superelastic Properties of Ti-Nb Base Alloys, Mater. Trans. 56 (2015) 625–634.

[41] C.H. Wang, C.D. Yang, M. Liu, X. Li, P.F. Hu, A.M. Russell, G.H. Cao, Martensitic microstructures and mechanical properties of as-quenched metastable β-type Ti–Mo alloys, J. Mater. Sci. 51 (2016) 6886–6896.
[42] A.G. Crocker, Twinned martensite, Acta Metall. 10 (1962) 113–122.
[43] T. Inamura, J.I. Kim, H.Y. Kim, H. Hosoda, K. Wakashima, S. Miyazaki, Composition dependent crystallography of α ″-martensite in Ti–Nb-based β-titanium alloy, Philos. Mag. 87 (2007) 3325–3350.
[44] B.S. Hickman, The formation of omega phase in titanium and zirconium alloys: A review, J. Mater. Sci. 4 (1969) 554–563.
[45] C.H. Wang, M. Liu, P.F. Hu, J.C. Peng, J.A. Wang, Z.M. Ren, G.H. Cao, The effects of α″ and ω phases on the superelasticity and shape memory effect of binary Ti-Mo alloys, J. Alloys Compd. 720 (2017) 488–496.
[46] S.K. Sikka, Y.K. Vohra, R. Chidambaram, Omega phase in materials, Prog. Mater. Sci. 27 (1982) 245–310.
[47] T.S. Kuan, R.R. Ahrens, S.L. Sass, The Stress-induced omega phase transformation in Ti-V alloys, Metall. Trans. A. 6 (1975) 1767–1774.
[48] H. Liu, M. Niinomi, M. Nakai, K. Cho, H. Fujii, Deformation-induced ω-phase transformation in a β-type titanium alloy during tensile deformation, Scr. Mater. 130 (2017) 27–31.
[49] F. Sun, J.Y. Zhang, M. Marteleur, T. Gloriant, P. Vermaut, D. Laillé, P. Castany, C. Curfs, P.J. Jacques, F. Prima, Investigation of early stage deformation mechanisms in a metastable β titanium alloy showing combined twinning-induced plasticity and transformation-induced plasticity effects, Acta Mater. 61 (2013) 6406–6417.
[50] X.H. Min, S. Emura, T. Nishimura, K. Tsuchiya, K. Tsuzaki, Microstructure, tensile deformation mode and crevice corrosion resistance in Ti–10Mo–xFe alloys, Mater. Sci. Eng. A. 527 (2010) 5499–5506.
[51] E. Bertrand, P. Castany, Y. Yang, E. Menou, T. Gloriant, Deformation twinning in the full-α″ martensitic Ti-25Ta-20Nb shape memory alloy, Acta Mater. 105 (2016) 94–103.
[52] D.H. Ping, Y. Yamabe-Mitarai, C.Y. Cui, F.X. Yin, M. a. Choudhry, Stress-induced α″ martensitic (110) twinning in β-Ti alloys, Appl. Phys. Lett. 93 (2008) 151911.
[53] H.S. Kim, S.H. Lim, I.D. Yeo, W.Y. Kim, Stress-induced martensitic transformation of metastable β-titanium alloy, Mater. Sci. Eng. A. 449–451 (2007) 322–325.
[54] A. Bhattacharjee, S. Bhargava, V.K. Varma, S.V. Kamat, A.K. Gogia, Effect of β grain size on stress induced martensitic transformation in β solution treated Ti–10V–2Fe–3Al alloy, Scr. Mater. 53 (2005) 195–200.
[55] H. Warlimont, L. Delaey, R. V. Krishnan, H. Tas, Thermoelasticity, pseudoelasticity and the memory effects associated with martensitic transformations, J. Mater. Sci. 9 (1974) 1545–1555.
[56] C. Brozek, F. Sun, P. Vermaut, Y. Millet, A. Lenain, D. Embury, P.J. Jacques, F. Prima, A β-titanium alloy with extra high strain-hardening rate: Design and mechanical properties, Scr. Mater. 114 (2016) 60–64.
[57] S. Hanada, M. Ozeki, O. Izumi, Deformation characteristics in β phase Ti-Nb alloys, Metall. Trans. A. 16 (1985) 789–795.
[58] S. Hanada, O. Izumi, Transmission Electron Microscopic Observations of Mechanical Twinning in Metastable Beta Titanium Alloys, Metall. Trans. A. 17 (1986) 1409–1420.
[59] M.J. Blackburn, J.A. Feeney, Stress-Induced Transformations in Ti-Mo alloys, J. Inst. Met. 99 (1971) 132–134.
[60] H. Tobe, H.Y. Kim, T. Inamura, H. Hosoda, S. Miyazaki, Origin of {332} twinning in metastable β-Ti alloys, Acta Mater. 64 (2014) 345–355.
[61] M.J. Lai, C.C. Tasan, D. Raabe, On the mechanism of {332} twinning in metastable β titanium alloys, Acta Mater. 111 (2016) 173–186.
[62] V.S. Litvinov, G.M. Rusakov, Twinning on the {332}<113> system in unstable β titanium alloys, Phys. Met. Metallogr. 90 (2000).
[63] B.A. Bilby, A.G. Crocker, The Theory of the Crystallography of Deformation Twinning, Proc. R. Soc. A. 288 (1965) 240–255.
[64] X.H. Min, X.J. Chen, S. Emura, K. Tsuchiya, Mechanism of twinning-induced plasticity in β-type Ti–15Mo alloy, Scr. Mater. 69 (2013) 393–396.
[65] P. Castany, M. Besse, T. Gloriant, In situ TEM study of dislocation slip in a metastable β titanium alloy, Scr. Mater. 66 (2012) 371–373.

[66] R.W. Cahn, Plastic Deformation of Alpha-Uranium ; Twinning and Slip, Acta Metall. 1 (1953) 49–70.
[67] F.C. Frank, A note on twinning in alpha-uranium, Acta Metall. 1 (1953) 71–74.
[68] P. Castany, Y. Yang, E. Bertrand, T. Gloriant, Reversion of a Parent {310}<130>α ″ Martensitic Twinning System at the Origin of {332 } <113> Twins Observed in Metastable β Titanium Alloys, Phys. Rev. Lett. 117 (2016) 1–6.
[69] A.G. Crocker, The crystallography of deformation twinning in alpha-uranium, J. Nucl. Mater. 16 (1965) 306–326.
[70] N.T.C. Oliveira, G. Aleixo, R. Caram, A.C. Guastaldi, Development of Ti–Mo alloys for biomedical applications: Microstructure and electrochemical characterization, Mater. Sci. Eng. A. 452 (2007) 727–731.
[71] N.T.C. Oliveira, A.C. Guastaldi, Electrochemical stability and corrosion resistance of Ti–Mo alloys for biomedical applications, Acta Biomater. 5 (2009) 399–405.
[72] X.H. Min, K. Tsuzaki, S. Emura, K. Tsuchiya, Enhancement of uniform elongation in high strength Ti–Mo based alloys by combination of deformation modes, Mater. Sci. Eng. A. 528 (2011) 4569–4578.
[73] T. Maeshima, M. Nishida, Shape Memory Properties of Biomedical Ti-Mo-Ag and Ti-Mo-Sn Alloys, Mater. Trans. 45 (2004) 1096–1100.
[74] H.Y. Kim, Y. Ohmatsu, J. Il Kim, H. Hosoda, S. Miyazaki, Mechanical Properties and Shape Memory Behavior of Ti-Mo-Ga Alloys, Mater. Trans. 45 (2004) 1090–1095.
[75] J. Il Kim, H.Y. Kim, H. Hosoda, S. Miyazaki, Shape Memory Behavior of Ti–22Nb–(0.5–2.0)O (at%) Biomedical Alloys, Mater. Trans. 46 (2005) 852–857.
[76] M. Nakai, M. Niinomi, T. Akahori, H. Tsutsumi, M. Ogawa, Effect of Oxygen Content on Microstructure and Mechanical Properties of Biomedical Ti-29Nb-13Ta-4.6Zr Alloy under Solutionized and Aged Conditions, Mater. Trans. 50 (2009) 2716–2720.
[77] M. Ahmed, D. Wexler, G. Casillas, D.G. Savvakin, E. V. Pereloma, Strain rate dependence of deformation-induced transformation and twinning in a metastable titanium alloy, Acta Mater. 104 (2016) 190–200.
[78] X. Min, S. Emura, F. Meng, G. Mi, K. Tsuchiya, Mechanical twinning and dislocation slip multilayered deformation microstructures in β-type Ti–Mo base alloy, Scr. Mater. 102 (2015) 79–82.
[79] L. Remy, Kinetics of f.c.c. deformation twinning and its relationship to stress-strain behaviour, Acta Metall. 26 (1978) 443–451.
[80] H. Zhan, D. Kent, G. Wang, M.S. Dargusch, The dynamic response of a β titanium alloy to high strain rates and elevated temperatures, Mater. Sci. Eng. A. 607 (2014) 417–426.
[81] K. Ogawa, Temperature and strain rate effects on plastic deformation of titanium alloys, Mater. Sci. Forum. 539–543 (2007) 3619–3624.

Chapter 2 Materials and experimental methods

2.1 Materials preparation

2.1.1 Ti-7.5Mo-xO alloys

The ingots of Ti-7.5Mo-xO (x = 0, 0.2, 0.3, 0.4 and 0.5 (wt.%), nominal composition) alloys were prepared by cold crucible levitation melting under Ar gas atmosphere. The amount of oxygen was controlled by the addition of TiO_2. The weight of each ingot was around 1 kg. After solidification, the ingots were hot forged at 1273 K to 40% thickness reduction and thereafter hot rolled at 1173 K into plates of 290 mm (length, *l*) × 50 mm (wide, *w*) × 10 mm (thickness, *t*) with 75% thickness reduction followed by air-cooling. The materials were subsequently solution-treated at 1173 K for 1 hour followed by water quenching. The schematic drawing of the sample preparation processing is illustrated in Fig. 2-1. Here, the principal axes of the hot-rolled plates are defined as RD (rolling direction), ND (normal direction to the rolling plane) and TD (transverse direction).

2.1.2 Ti-10Mo-1Fe alloy

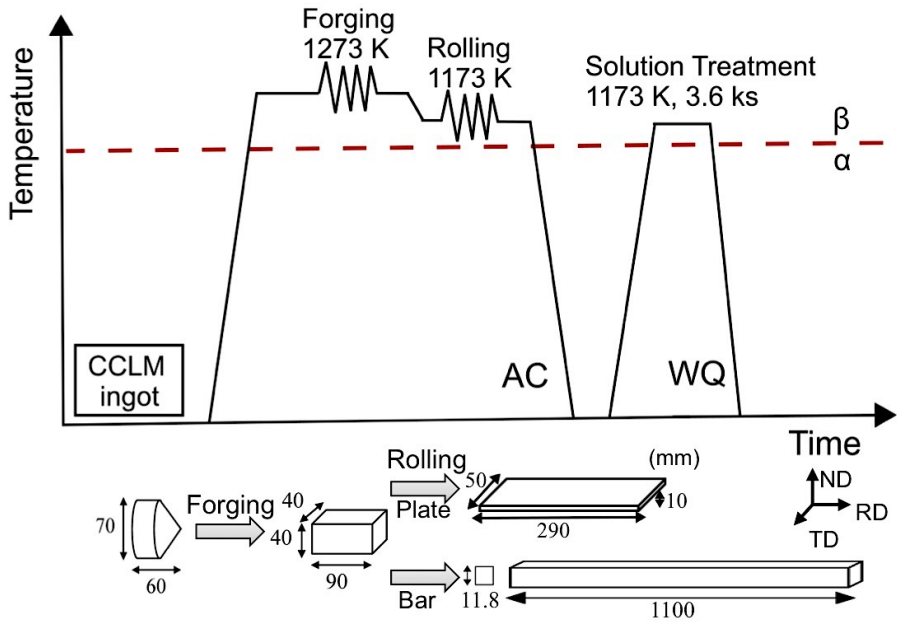

Fig. 2-1 Schematic drawing of the heat treatment for Ti-7.5Mo alloy (plate shape) and Ti-10Mo-1Fe (bar plate) with different oxygen contents. CCLM, AC, WQ refer to cold crucible levitation melting, air-cooling and water quenching, respectively.

The ingot of Ti-10Mo-1Fe (wt.%) alloy was also prepared by cold crucible levitation melting under Ar gas atmosphere. After solidification, the ingot was hot forged at 1273 K into the block of 90 mm (*l*) × 40 mm (*w*) × 40 mm (*t*). However, the block was further hot rolled at 1173 K into the 14.3 mm square bar, followed by air-cooling. Then the solution-treatment was performed at 1173 K in the single β phase region for 1 hour, followed by water quenching, as shown in Fig. 2-1.

2.2 Mechanical tests

2.2.1 Tensile tests

In order to investigate the tensile behavior and strain rate dependence of prepared Ti-alloys, the uniaxial tensile tests were carried out on an INSTRON 5581 testing machine with a 10 mm gauge length clip-on extensometer to record the strain. Fig. 2-2 shows the parameters of tensile specimens with a gauge length of 18 mm (*l*) x 4 mm (*w*) x 2 mm (*t*). They were cut by electric discharge machine. The tensile axis (TA) was parallel to RD. The tensile behaviors of Ti-7.5Mo-xO alloys were investigated at a constant strain rate of $2.8x10^{-4}$ s^{-1}. In order to track the microstructure evolution of Ti-7.5Mo alloy, mechanically polishing was performed prior to tensile deformation with emery paper of #320, and then changed to SiO_2 colloidal suspension with particle size from 9 μm to 3 μm, finally the sample was polished and etched together with a mix of Mastermet (colloidal silica suspension with a particle size of 0.06 μm): H_2O_2 = 4:1 (in volume percent) to a mirror surface. In order to study the effect of strain rate on the work-hardening behavior of Ti-10Mo-1Fe alloy, tensile tests were carried out at 5 different strain rates of $2.8x10^{-5}$, $2.8x10^{-4}$, $2.8x10^{-3}$, $2.8x10^{-2}$ and $2.8x10^{-1}$ s^{-1}, respectively. All the tensile tests were carried out at an ambient temperature.

2.2.2 Micro-hardness tests

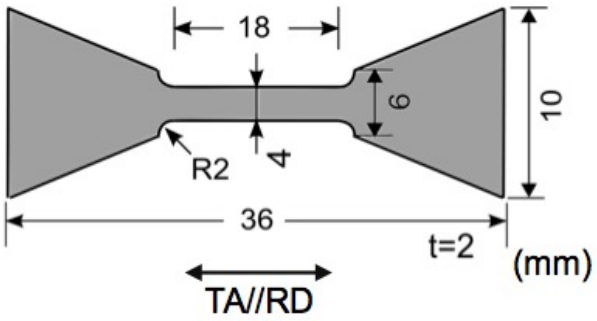

Fig. 2-2 Parameters of tensile specimen. The tensile axis (TA) is parallel to RD.

The hardness properties of prepared Ti-alloys were measured using a Vickers micro-hardness tester (Matsuzawa MMT-X) with a load of 100 g for a loading time of 15 s. The specimens were cut after solution-treatment and the RD-TD planes were mechanically polished to mirror surfaces. Then the tests were performed with a load of 100 g for a loading time of 15 s. In order to achieve the reliable results, 50 indents were tested for each sample and the average values were used.

2.3 Microstructure characterizations

2.3.1 X-ray diffraction

In the present study, XRD analysis was performed on a Rigaku TTR III instrument (Fig. 2-3) with Cu-Kα radiation (λ = 1.541 Å), operated at 40 kV-50 mA. For the phase identification in Ti-7.5Mo-xO alloys, the scanning condition was set with a step size of 0.02° and a scan speed of 0.5-2°/min. The surface

of specimens was prepared by mechanically polish and followed by etching with a solution of Mastermet and H_2O_2 (4:1 by volume) to a mirror condition.

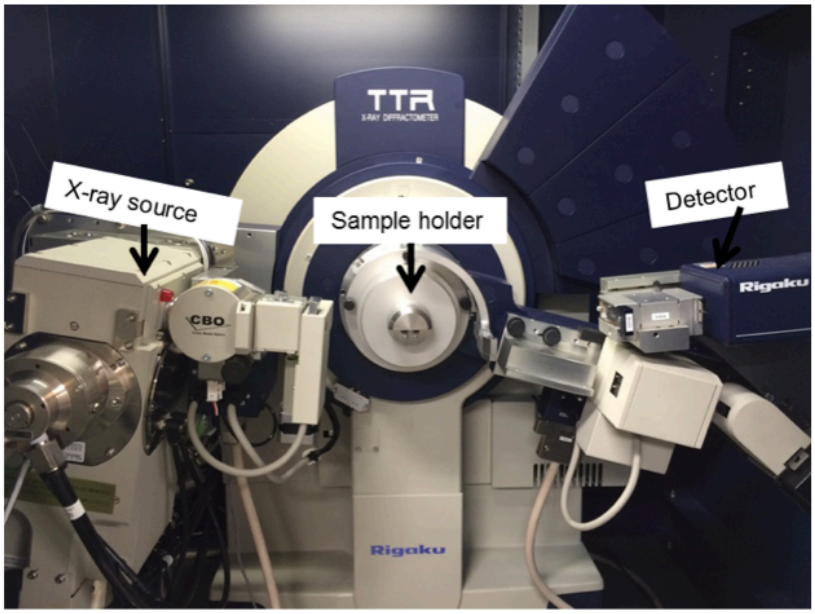

Fig. 2-3 Rigaku TTR III instrument with three main parts of sample holder in the middle, X-ray source on the left arm and Detector on the right arm.

2.3.2 Scanning electron microscope

In the present study, a Σigma-Zeiss field emission scanning electron microscope (FE-SEM) was used for microstructure characterization. It is equipped with a backscattered electron (BSE) detector and an electron backscattered diffraction (EBSD) detector by TSL orientation imaging microscopy (OIM) system. EBSD maps were obtained at 20 kV with a step size ranging between 20-1500 nm and a working distance between 15-20 mm. The data was analyzed by a TSL OIM data analysis software.

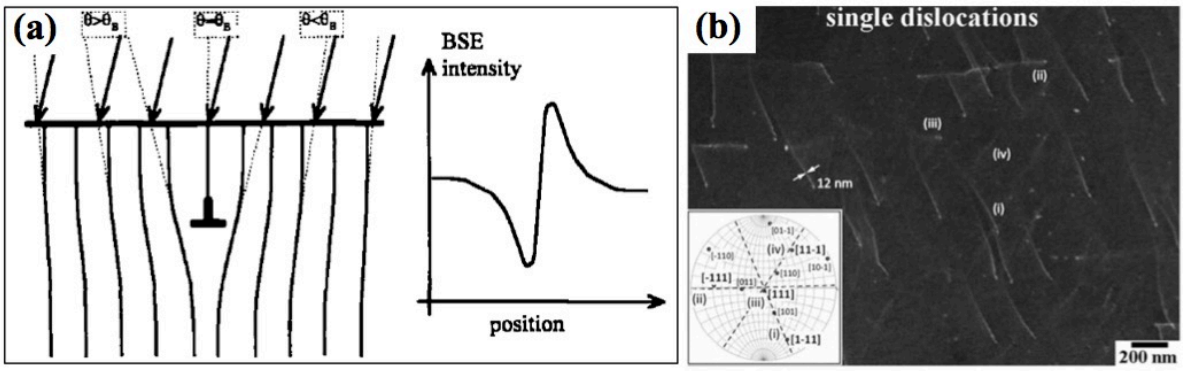

Fig. 2-4 (a) Schematic diagram of ECCI technique with illustration of the BSE intensity change by the local lattice plane tilting near a dislocation [3]. (b) ECCI image of dislocation taken in a lightly deformed FeSi alloy [2].

In addition, electron channeling contrast imaging (ECCI) technique was used as an effective method for the high-resolution microstructure observation especially for the thin α″ martensitic plate. The BSE intensity

varies rapidly on the orientation of the crystal lattice planes with the electron channeling mechanism. Thus the slight distortion of crystal lattice caused by strain fields could be identified as the change of BSE signal by effective BSE detectors. Based on this, ECCI could record the crystal defects in high-resolution even dislocations could be clearly identified in SEM machine [2]. Fig. 2-4 (a) shows the mechanism of ECCI technique [3] and Fig. 2-4 (b) shows an example of ECCI image of single dislocations in a lightly deformed FeSi alloy [2]. In the present study, ECCI observations were carried out in the Σigma-Zeiss FE-SEM with a voltage between 5 kV and 10 kV and the working distance ranging from 5 mm to 10 mm with sample slightly tilting less than 3°.

2.3.3 Focused ion beam

For TEM observations, the site-specific samples were prepared using a dual-beam focused ion beam (FIB) technique in a FIB-SEM Auriga Zeiss instrument. An example is the secondary electron (SE) image by SEM shown in Fig. 2-5, where the in-depth TEM sample was fabricated in Ti-7.5Mo alloy. This sample was subsequently lifted out by a manipulator, then mounted onto a silicon grid and milled to become electron-transparent. A Pt layer was deposited on the sample surface before FIB milling to avoid any surface damage.

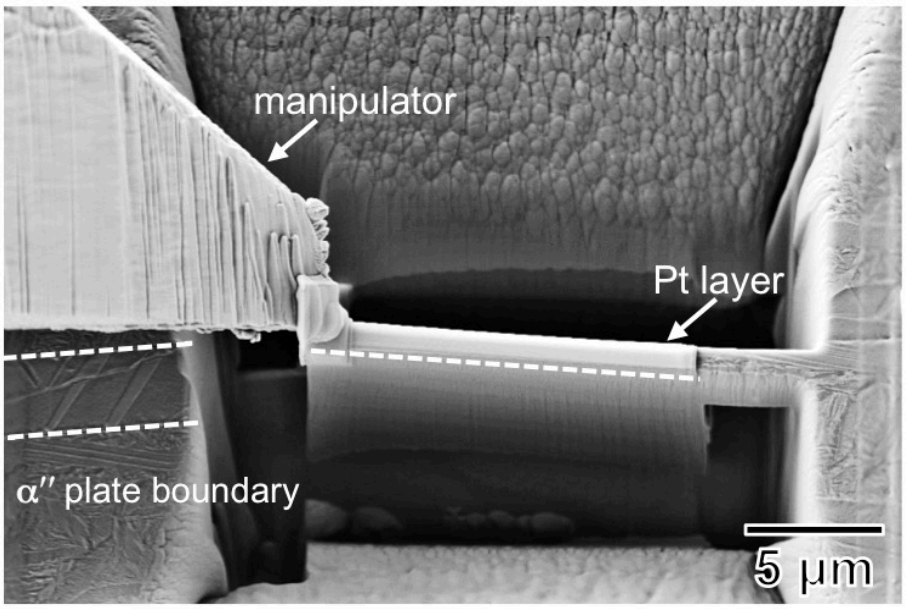

Fig. 2-5 An example of secondary electron (SE) image of TEM-sample taken from a α″ martensite plate in Ti-7.5Mo alloy.

2.3.4 Transmission electron microscope

TEM observations were performed using a JEOL JEM-2000FX and a JEOL JEM-2100F microscope operated at 200 kV. The goniometer on the JEOL JEM-2000FX can be tilted of ± 45° *x* and ± 30° *y*, which offers large space to obtain the electron diffraction patterns. High-resolution TEM (HRTEM) images were

taken on the JEOL JEM-2100F microscope with a probe size under 0.5 nm. TEM thin foils were prepared by a Struers Tenupol-3 twin-jet electropolishing machine. The specimens were firstly mechanically polished to a thickness of 100 μm and then disks of 3 mm diameter were punched. Then the twin-jet electron polishing was performed with a solution of methanol, 1-butanol, and perchloric acid (13:6:1 in volume) at ~238 K and at the voltage of 20 V.

2.4 Thermal stability measurements

In order to predict the phase transformation behavior, differential scanning calorimeter (DSC) measurements were carried out using a Netzsch STA-449F3 instrument at heating and cooling rate of 10 K/min in an Ar atmosphere. The sample with a mass of ~25 mg was put in an alumina crucible, while the reference crucible is generally kept empty during the measurement.

References

[1] M.J. Blackburn, J.A. Feeney, Stress-Induced Transformations in Ti-Mo alloys, J. Inst. Met. 99 (1971) 132–134.

[2] I. Gutierrez-Urrutia, S. Zaefferer, D. Raabe, Coupling of Electron Channeling with EBSD: Toward the Quantitative Characterization of Deformation Structures in the SEM, Jom. 65 (2013) 1229–1236.

[3] A.J. Wilkinson, P.B. Hirsch, Electron Diffraction Based Techniques in Scanning Electron Microscopy of Bulk Materials, 4328 (1997).

Chapter 3 Deformation twinning in as-quenched α" martensite in Ti-7.5Mo alloy

3.1 Introduction

β titanium alloys such as Ti-Mo, Ti-Nb, Ti-Ta-Nb-Zr, Ti-Zr alloys have been widely used in biomedical applications, due to their excellent properties such as low Young's modulus, superior biocompatibility, high corrosion resistance, and shape memory effect [1-3]. One characteristic of β-Ti alloys is the martensitic transformation from bcc-β to orthorhombic-α" upon quenching or deformation. The phase transformation strongly depends on the amount of β-stabilizing elements such as Mo, Nb, and Ta [4-7]. The orthorhombic-α" martensite has been reported to play an important role in characteristic mechanical properties of β-Ti alloys [4-9]. For example, the shape memory effect and superelasticity of Ti-Nb alloys are associated with their reversible martensitic transformation between the β phase and α" martensite phase [7, 10]. Meanwhile, the α" martensite has been found to decrease Young's modulus of β-Ti alloys close to the values of human bones (~30 GPa), which is critical for the design of advanced biomaterial [4,11–13]. Ho et al. [4] reported that the Ti-7.5Mo (wt.%) alloy with fully α" martensite has the lowest Young's modulus (~65 GPa) in the Ti-Mo binary alloy system. In addition, this alloy also exhibits good bone-implant interaction [14], which makes it as a promising candidate for implant applications [15,16].

Extensive studies have been focused on the crystal structure and morphology of α" martensite [17–20]. Brown et al. [17] have reported that α" martensite contains a disordered crystal structure with the space group of *Cmcm*. The lattice parameters of α" martensite are strongly sensitive to the alloy composition [7,9,18,21]. On the other hand, the occurrence of an internal transformation twinning structure in the α" martensite has been commonly reported. This structure is associated with the accommodation of the transformation strain from β to α" martensitic transformation [22]. Different transformation twinning modes have been reported such as $\{111\}_{\alpha''}$-type I [19,23–25], $<211>_{\alpha''}$-type II [19,26], and $\{110\}_{\alpha''}$-compound twinning [19,27,28]. The activation of these twinning modes strongly depends on the lattice parameters of β and α" martensite phases and hence on the alloy compositions [19,29]. For instance, Inamura et al. [19] investigated the transformation twinning modes in a Ti-(33-46)Nb-3Al (wt.%) alloys and found that, $\{111\}_{\alpha''}$-type I and $<211>_{\alpha''}$-type II twinning were formed in lower Nb content (< 37 wt.%) and $\{110\}_{\alpha''}$-compound twinning in higher Nb content (> 37 wt.%).

Despite the advantages of low Young's modulus and good biocompatibility, the metastable Ti-Mo alloys with fully α" martensite exhibits the main drawback, which is the relatively lower mechanical strength compared to stable β-Ti alloys [30,31]. Excellent mechanical properties, combining high strength and low Young's modulus, are required for the design of biomaterials [2]. In β-Ti alloys, it has been reported that deformation mechanisms such as $\{332\}<113>_{\beta}$ deformation twinning have a key role on the work-hardening behavior and hence on the mechanical properties by the so-called twinning-induced plasticity (TWIP) effect [33–35]. In metastable β-Ti alloys, a better understanding of the deformation mechanisms of α" martensite is

essential for the enhancement of mechanical properties. So far few reports have analyzed the deformation twinning of α" martensite, mainly in Ti-Nb [28,36] and Ti-Ta-Nb [26] alloy systems. However, to the authors' knowledge, the deformation mechanisms of α" martensite in the Ti-Mo alloy system has not yet been investigated.

Therefore, the aim of this study is to investigate the deformation twinning structure of α" martensite in the metastable β Ti-Mo alloy system. We have analyzed the as-quenched and deformed microstructures of α" martensite in a Ti-7.5Mo (wt.%) alloy by an experimental approach combining SEM and TEM. A microstructural patch of interest was tracked upon tensile deformation to a strain level of 5% by SEM, followed by TEM characterization of deformed microstructure in a FIB-fabricated sample. The as-quenched α" martensite consists of $\{111\}_{\alpha''}$-type I transformation twinning. Upon straining, a new deformation twinning mode, namely, $\{112\}_{\alpha''}$-type I twinning, was identified for the first time in metastable β-Ti alloys. The possible twinning modes in the orthorhombic-α" martensite were analyzed based on the crystallographic twinning theory by Bilby and Crocker [37,38]. The mechanism of the observed $\{112\}_{\alpha''}$-type I twinning mode is explained based on the characteristic atomic shears and shuffles.

3.2 Results

The deformation mechanisms of as-quenched α″ martensite were investigated by the correlative SEM/TEM method schematically shown in Fig.1. The as-quenched state was firstly evaluated by BSE and EBSD. Subsequently, the sample was tensile deformed to 5% strain and an area of interest was tracked by BSE and EBSD without any additional grinding or polishing. Thereafter, a TEM sample was cut from a martensite plate and lifted out by a manipulator by using a dual-beam FIB in a FIB-SEM Auriga Zeiss instrument. A Pt layer was deposited on the sample surface before FIB milling to avoid any surface damage.

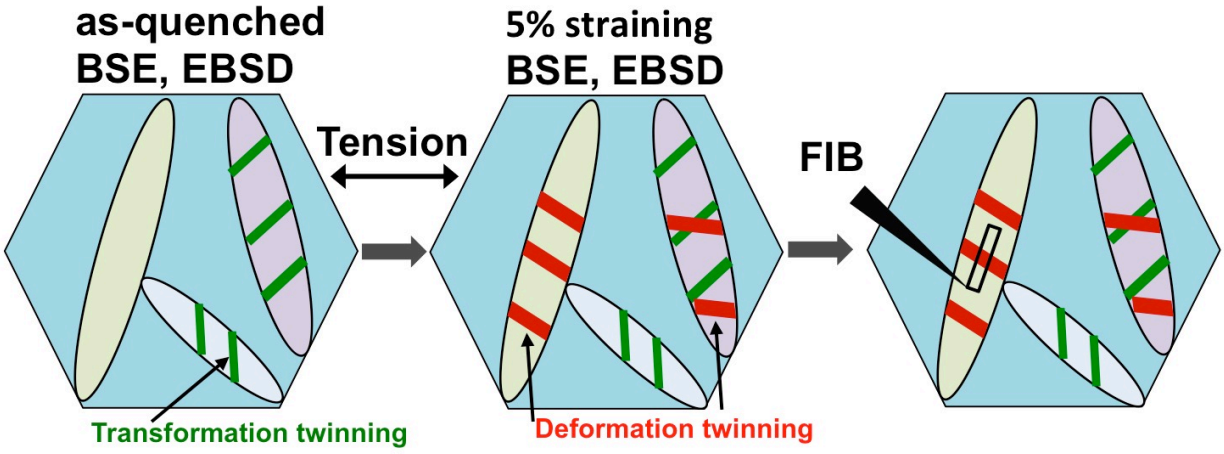

Fig. 3-1 Experimental method for the characterization of deformation microstructure.

3.2.1 As-quenched microstructure

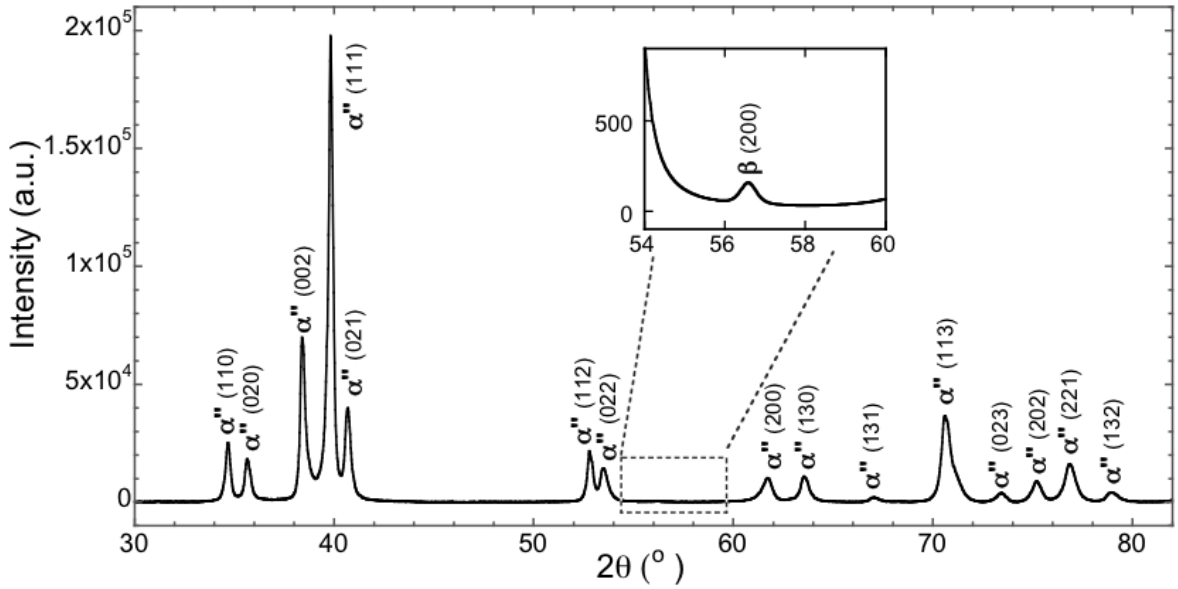

Fig. 3-2 X-ray diffraction profile of as-quenched Ti-7.5Mo alloy.

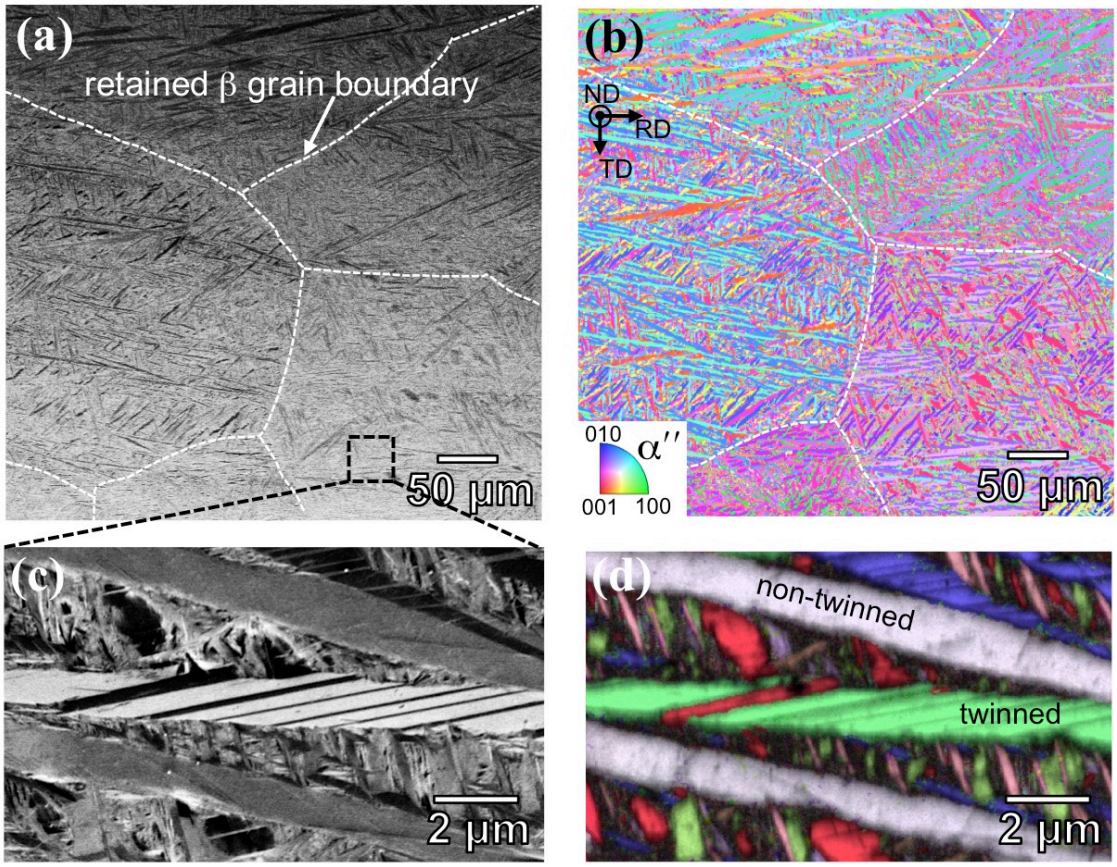

Fig. 3-3 (a) Backscattered electron (BSE) image showing the as-quenched microstructure. (b) Corresponding inverse pole figure (IPF) map of the region in (a). (c) Higher magnification of the α′′ plates taken from the region indicated in (a), and its IPF combined with image quality (IQ) map is shown in (d).

Fig. 3-2(a) shows the XRD profile of the as-quenched Ti-7.5Mo alloy from 1173 K. The result reveals that the as-quenched state mainly consists of the orthorhombic-α" martensite phase with lattice parameters of aα" = 0.3002 ± 0.0001 nm, bα" = 0.5033 ± 0.0005 nm, and cα" = 0.4680 ± 0.0005 nm. Furthermore, the inset of Fig. 2(a) indicates the existence of retained bcc-β phase, as shown from the $(200)_\beta$ reflection at 2θ = 55.8°. This indicates that the β→α″ phase transformation is almost completed upon quenching, which agrees with former reports [4,39]. The BSE image (Fig. 3-3(a)) and EBSD- IPF map (Fig. 3-3(b)) reveal the acicular morphology of α″ martensite plates, which are uniformly distributed throughout the parent β grain. In particular, EBSD reveals that a low fraction (<5 %) of β phase is retained at the parent grain boundaries (indicated by dashed lines in Fig. 3-3(b)). The higher magnification images of Figs. 3-3(c) and Figs. 3-3(d) indicate that the α″ martensite plates with an average thickness of about 2 μm contain internal twinning structures. These twinning structures are believed to accommodate the transformation strains from bcc-β to orthorhombic-α″ upon quenching, hereafter named as transformation twinning.

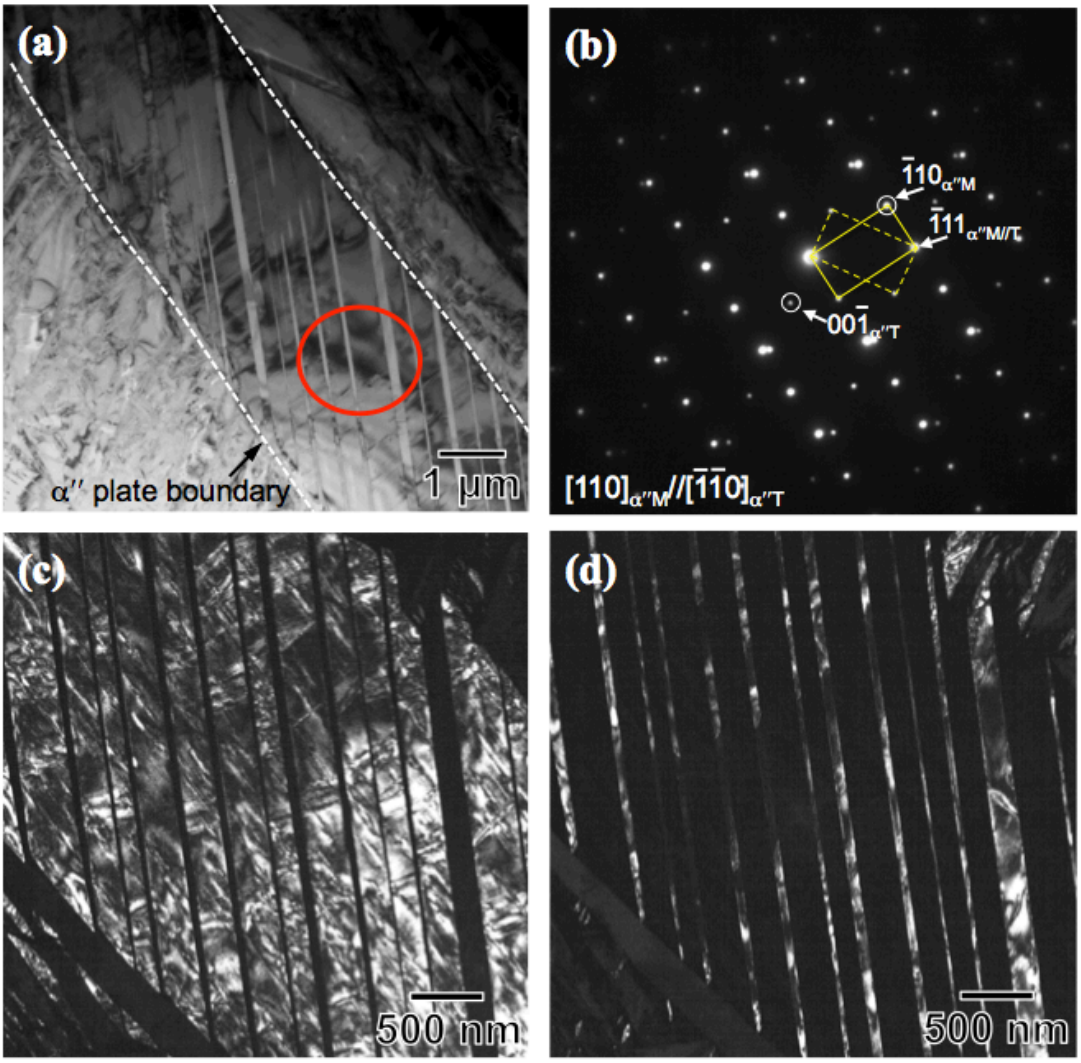

Fig. 3-4 (a) TEM image of the athermal α″ martensite with internal twinning structure. (b) SAED pattern of the red circled area in (a) with the zone axis of [110]α″. (c) and (d) Dark field (DF) images taken from matrix the diffraction spots of matrix and twin in (b), respectively. The subscripts "M" and "T" denote matrix and twin, respectively.

TEM characterizations were performed on the as-quenched Ti-7.5Mo alloy. The α″ martensite plate with internal twinning structure is shown in Fig. 3-4(a). Fig. 3-4(b) shows a SAED pattern taken from the region shown in Fig. 3-4(a). The SAED pattern consists of two sets of reflections from $[110]_{\alpha"M}$ and $[\bar{1}\bar{1}0]_{\alpha"T}$ crystallographic orientations (M: matrix; T: twin). It can be seen that the two crystal orientations contain a mirror symmetry with respect to the $(\bar{1}11)_{\alpha"M//T}$ plane. This result indicates that the internal twinning structure of α″ martensite plates contains a $\{111\}_{\alpha"}$ twinning plane, and accordingly, they are $\{111\}_{\alpha"}$-Type I twins [40]. Fig. 3-4(c) and Fig. 3-4(d) show the dark field (DF) images of the matrix and twin plates, which are taken from the circled spots in Fig. 3-4(b), respectively. As shown in Fig. 3-4(d), the twin plates are very thin (thickness between 20 and 150 nm) and fully aligned along $\{111\}_{\alpha"}$ planes. Fig. 3-5(a) shows the high-resolution TEM (HRTEM) image of the twin structure. The magnified HRTEM image of the matrix/twin interface is illustrated in Fig. 3-5(b). It can be observed that the lattice fringes of twin and matrix distribute symmetrically about the twin interphase ($(\bar{1}10)_{\alpha"M//T}$ plane), which indicates that the $\{111\}_{\alpha"}$ twinning plane is coherent, consistent with the previous reports [25,41]. In addition, the lattice fringes with the spacing of 0.47 nm corresponding to the $(001)_{\alpha"M}$ plane of α″ matrix is visible in Fig. 3-5(b), consistent with the results of $c_{\alpha''}$ calculated from XRD profile (Fig. 3-2). Fig. 3-5(c) shows the Fourier filtered transformation (FFT) image corresponding to the electron diffraction pattern, which indicates the $\{111\}_{\alpha"}$ twinning plane.

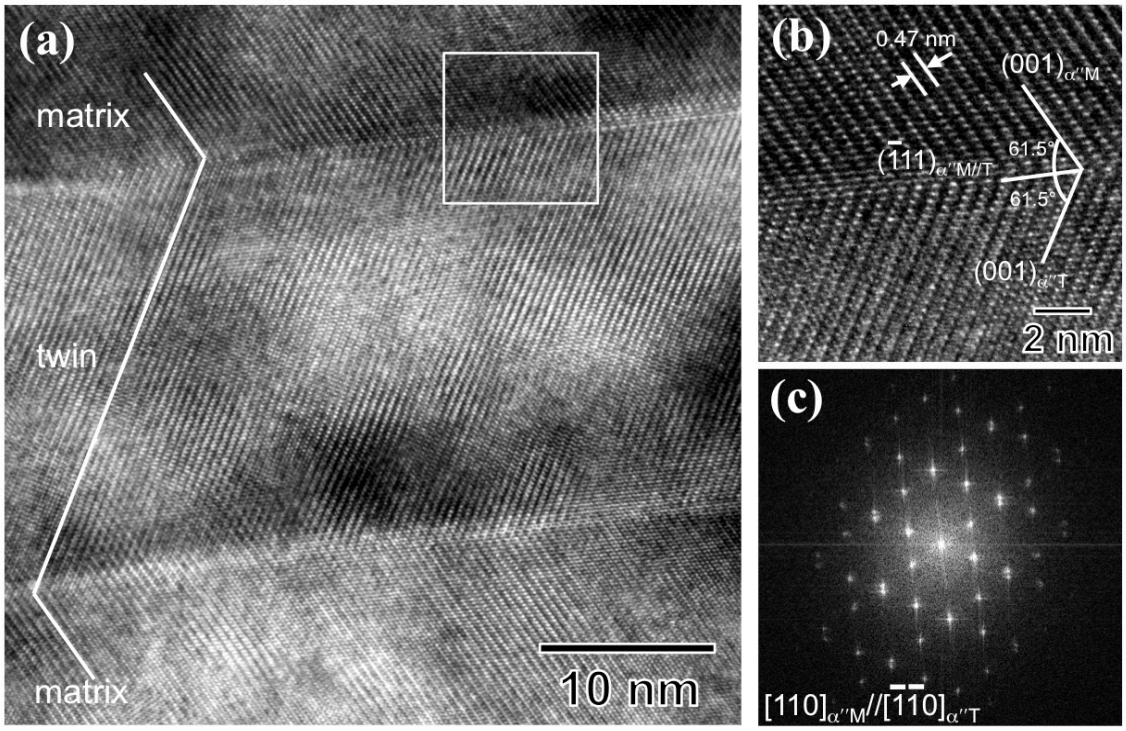

Fig. 3-5 (a) High resolution TEM (HRTEM) image of the twin interface structure. (b) Higher magnification of the α″ plates taken from the region indicated in (a). (c) Corresponding fast Fourier transformation (FFT) diffraction pattern of (a).

3.2.2 Tensile property

Fig. 3-6 shows the true stress-strain curve of the Ti-7.5Mo alloy with fully α″ phase tensile deformed at an initial strain rate of 2.8×10^{-4} s^{-1}. The corresponding work hardening rate ($\theta = d\sigma / d\varepsilon$, where σ and ε are the true stress and true strain, respectively) curve is also displayed in Fig. 3-6. The present Ti-7.5Mo alloy exhibits excellent tensile properties, combing high strength (ultimate tensile strength of 700 MPa), good ductility (uniform elongation close to 18% before the onset of necking, where σ equals θ) and significant work hardening (θ=2400 MPa at ε= 5%). The work hardening rate illustrates a sharply decreasing stage at strain up to 3%, followed by a gradually decreasing stage until the end of uniform plastic deformation (ε= 18%).

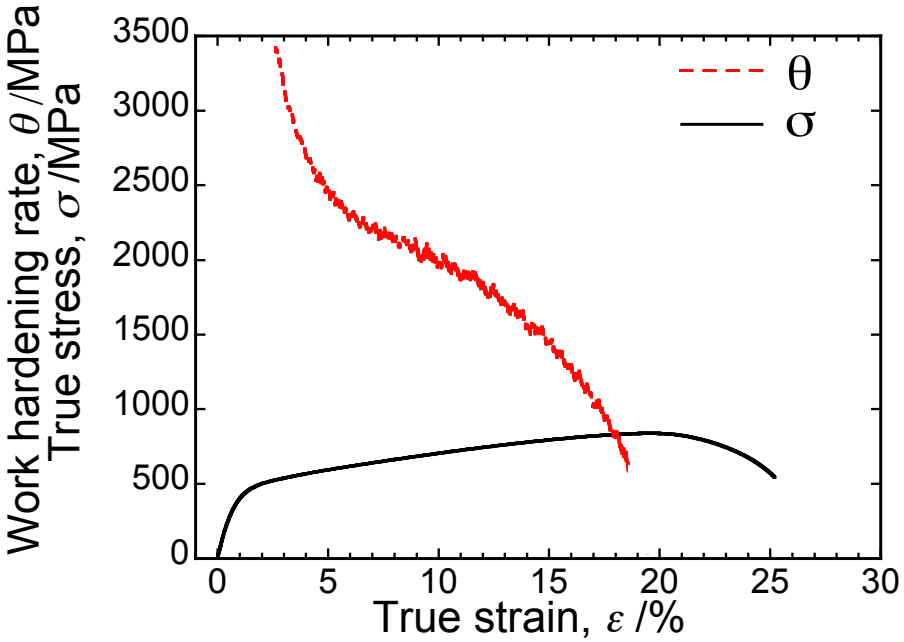

Fig. 3-6 True stress-strain curve of the Ti-7.5Mo alloy.

3.2.3 Deformation mechanism

3.2.3.1 Deformation twinning

Fig. 3-7 shows the results of ex-situ tensile test conducted on a pre-polished tensile sample. The ECCI image in Fig. 3-7(a) displays the as-quenched microstructure containing internal twined and non-twined plates. The corresponding microstructure with 5% strain is shown in Fig. 3-7(b). High magnification ECCI images of Fig. 3-7(c) and (d) are taken from the framed regions in Fig. 3-7(a) and (b), respectively, displaying the occurrence of several deformation bands (indicated by the red lines in Fig. 3-7(d)) induced by tension. The corresponding inverse pole figure (IPF) image (Fig. 3-7(e)) indicates a twinning relationship between the matrix and deformation-induced lamellas sharing different orientation. Two variants of deformation bands (V1 and V2) can be identified throughout the α" plate, as shown in Fig. 3-8(a). Fig. 3-8(b) shows the point-to-origin misorientation profile along the arrow in Fig. 3-8(b). The two variants of deformation bands (V1: $[2\bar{3}0]$//TA and V2: $[29\bar{1}]$//TA) have different orientations with the α" matrix

([305]//TA) and both have a misorientation angle of 86.5° with the α" matrix. These results indicate that the activated deformation twins have the same twinning system.

Further characterization was performed by TEM on a FIB lift-out specimen from the region marked in

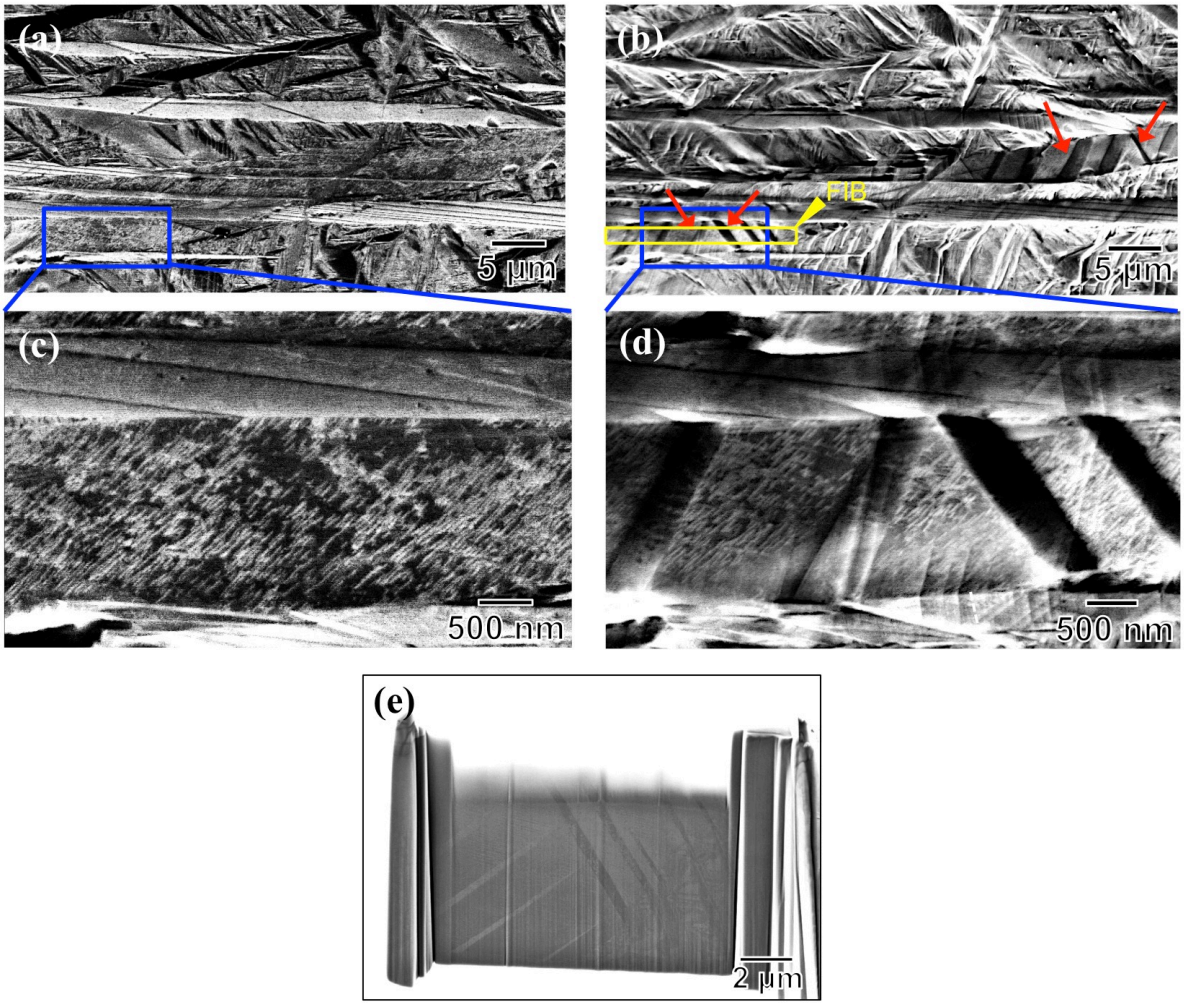

Fig. 3-7 Sequential electron channeling contrast images (ECCIs) showing the microstructure evolution of as-quenched state, (a), and 5% strain, (b). The tensile axis (TA) is horizontal respect to the images. The deformation band structures are indicated by red arrows. Higher magnification images of (c) and (d) taken from the white boxed regions in (a) and (b), respectively. (e) SE image of FIB-fabricated sample taken from the region shown in (b).

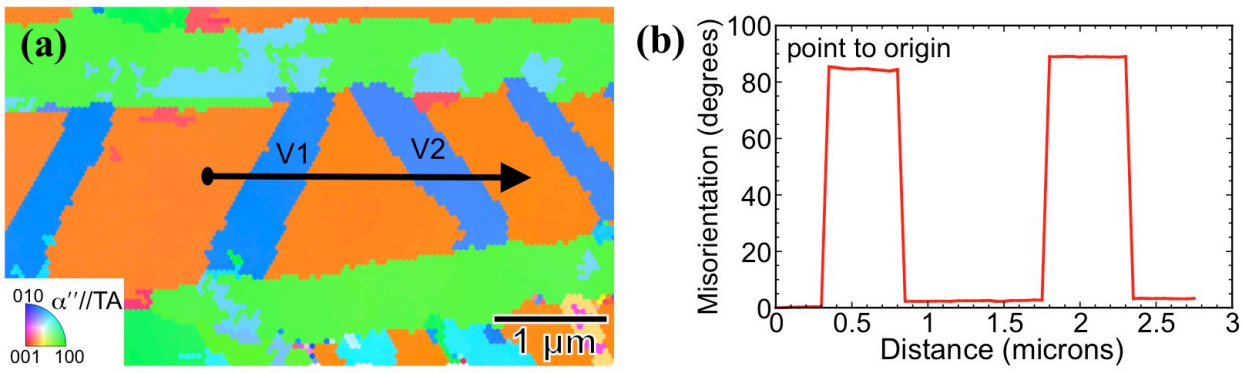

Fig. 3-8 (a) Corresponding IPF image of Fig. 3-7(d). (b) Misorientation angles of the points along the arrow shown in (e).

Fig. 3-7(d), and the results are displayed in Fig. 3-9 and Fig. 3-10. Fig. 3-9(a) shows a low magnification overview of the deformation band. The SAED pattern (Fig. 3-9(d)) and its key diagram (Fig. 3-9(e)) reveal a twinning relationship between the deformation band and α″ matrix. More specifically, the twinning plane is indexed as $(112)_{\alpha"}$. This result indicates that the observed deformation bands accordingly corresponds to $\{112\}_{\alpha"}$-Type I deformation twins. It is consistent with the results of Figs. 3-10(a) and 3-10(b), which show the HRTEM image of the twin/matrix interface and the corresponding SAED pattern with zone axis of $[\bar{1}10]_{\alpha"M}//[1\bar{1}0]_{\alpha"T}$, respectively. The HRTEM image of Fig. 3-10(a) also indicates the mirror inversion symmetry around the reciprocal direction of $(112)_{\alpha"M//T}$. Therefore, the deformation bands can be characterized as $\{112\}_{\alpha"}$-type I deformation twins. To the authors' knowledge, the activated deformation twinning mode, *i.e.*, $\{112\}_{\alpha"}$-type I deformation twinning, has never been reported in the α″ martensite in β-Ti alloys. Furthermore, Fig. 3-10(a) shows that the angle between $(110)_{\alpha"M}$ and $(110)_{\alpha"T}$ lattice planes is about 86.5°. The SAED pattern (Fig. 3-10(b)) reveals a rotation of 86.5° about the $[\bar{1}10]_{\alpha"}$ crystallographic axis between the crystal matrix (solid line) and the twin (dashed line), consistent with the misorientation angle measured by EBSD as shown in Fig. 3-8(b). In addition, Fig. 3-9(a) also exhibits the occurrence of parallel striations along the α" matrix, as indicated by white arrows. These structures have been frequently observed in the as-quenched α" martensite in β-Ti alloys and have been ascribed to the formation of stacking faults due to basal plane shuffling [19,41–43].

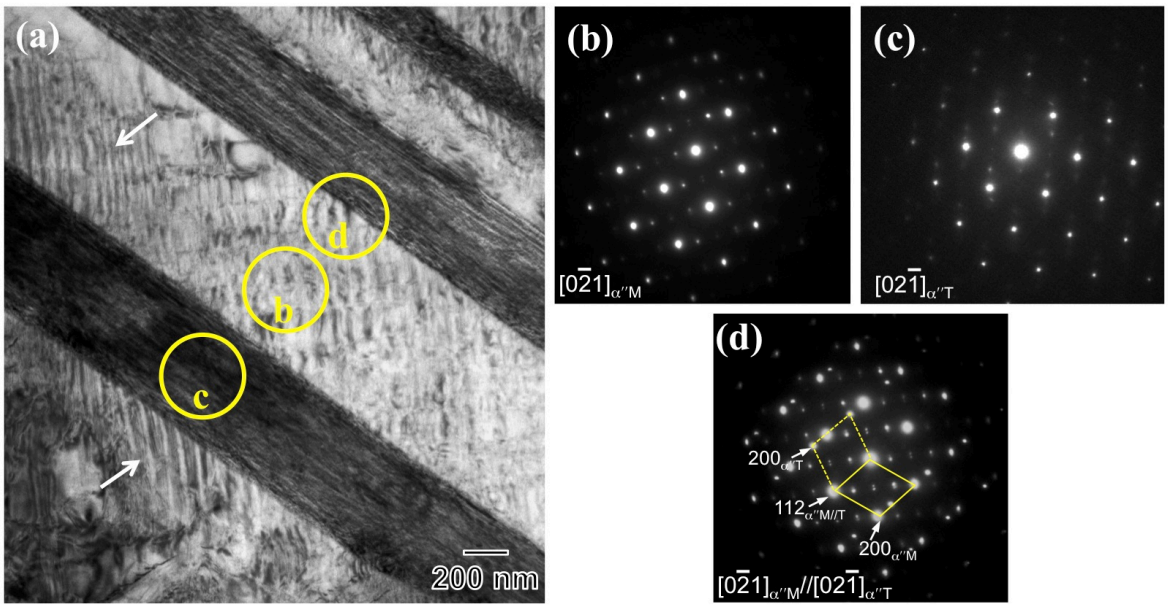

Fig. 3-9 (a) TEM image of the lamella prepared by FIB from the location indicated in Fig. 3-7(b). (b-d) SAED patterns taken from the circled regions indicated in (a). The incident beam is parallel to $[\mathbf{0\bar{2}1}]_{\alpha"M}//[\mathbf{02\bar{1}}]_{\alpha"T}$.

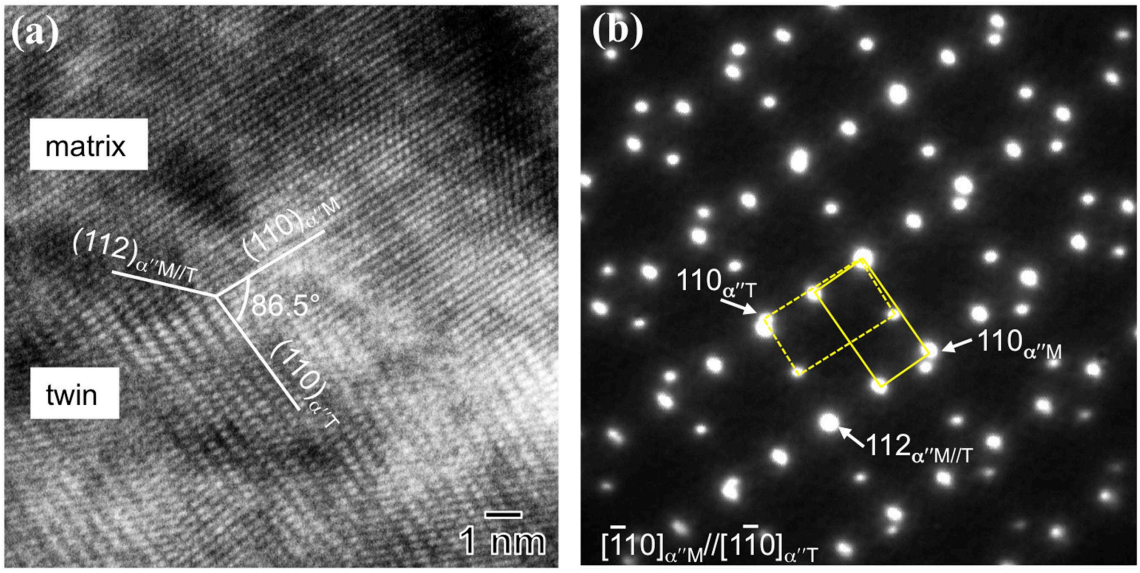

Fig. 3-10 (a) HRTEM image of deformation twin shown in Fig. 3-8(a). (b) Corresponding SAED pattern with the zone axis of $[\bar{\mathbf{1}}\mathbf{10}]_{\alpha''M}//[\mathbf{1}\bar{\mathbf{1}}\mathbf{0}]_{\alpha''T}$.

3.2.3.2 Twin-Twin intersection

The deformation twinning structures were not only observed in the non-twinned α″ plate (Fig. 3-10(b)), also demonstrated in the α″ plate containing pre-existed transformation twinning. An example of the α″ plate is shown in Fig. 3-11. The ECCI image in Fig. 3-11(a) displays the as-quenched α″ plate, containing alternating transformation twins. The corresponding microstructure with 5% strain is in shown in Fig. 3-11(b). Deformation twinning structures are activated upon deformation. A higher magnification ECCI image taken from the region marked in Fig. 3-11(b), displaying the configuration of interaction between deformation twinning and transformation twinning. Here the transformation twinning is crossed twinning with twin boundaries indicated by green lines, while the deformation twinning is crossing twinning with twin boundaries indicated by red lines. It is clear that the intersection of deformation twinning and transformation twinning is accomplished by the activation of secondary twinning (indicated by yellow lines) in the crossed twin. For the identification of the twinning structures in the intersection region, further characterization such as TEM observation is necessary.

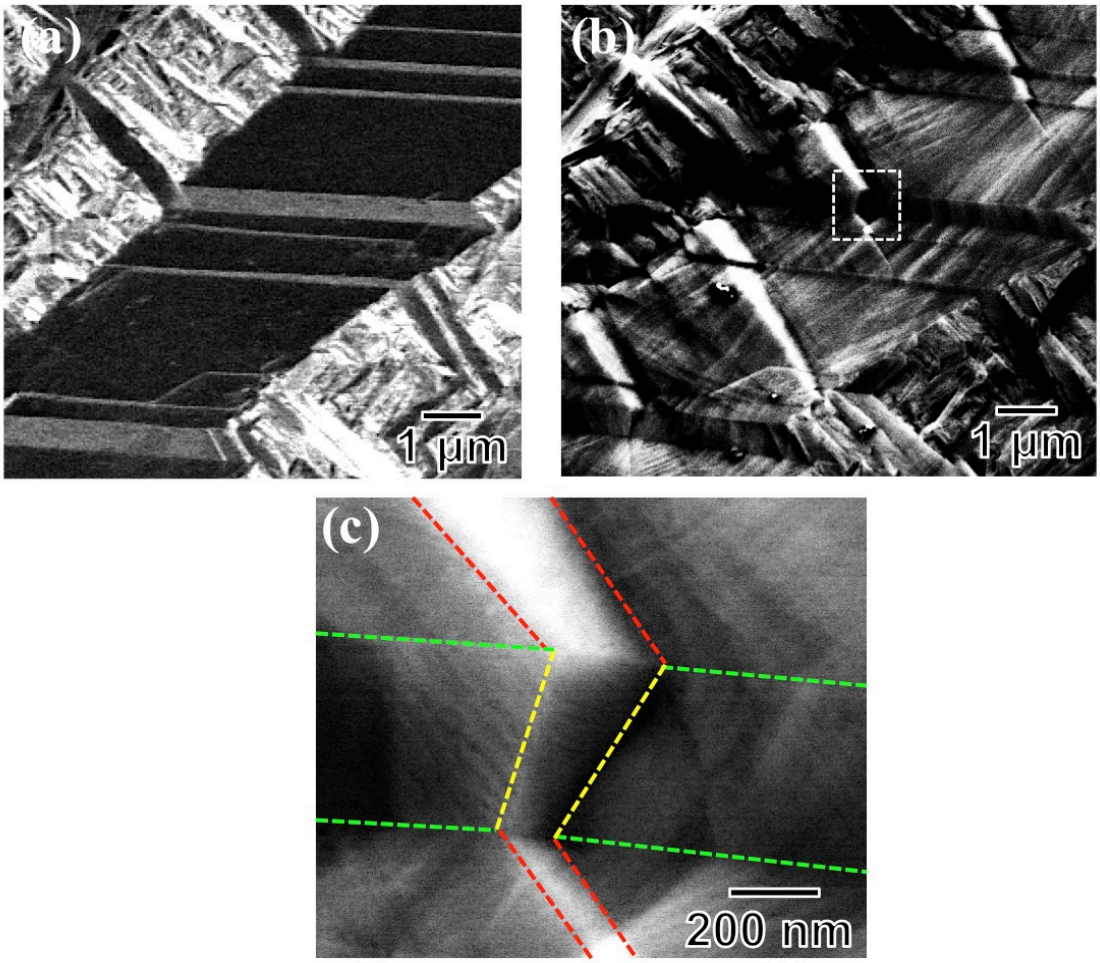

Fig. 3-11 (a) ECCI figure showing the as-quenched α″ martensite with internal transformation twins. (b) Corresponding deformation microstructure of (a) with 5% strain. The tensile axis is horizontal to the images. (c) Magnified ECCI of the frame region shown in (b). The secondary twin (yellow) is observed in the crossed transformation twin (green) after the intersection of crossing deformation twin (red) and transformation twin.

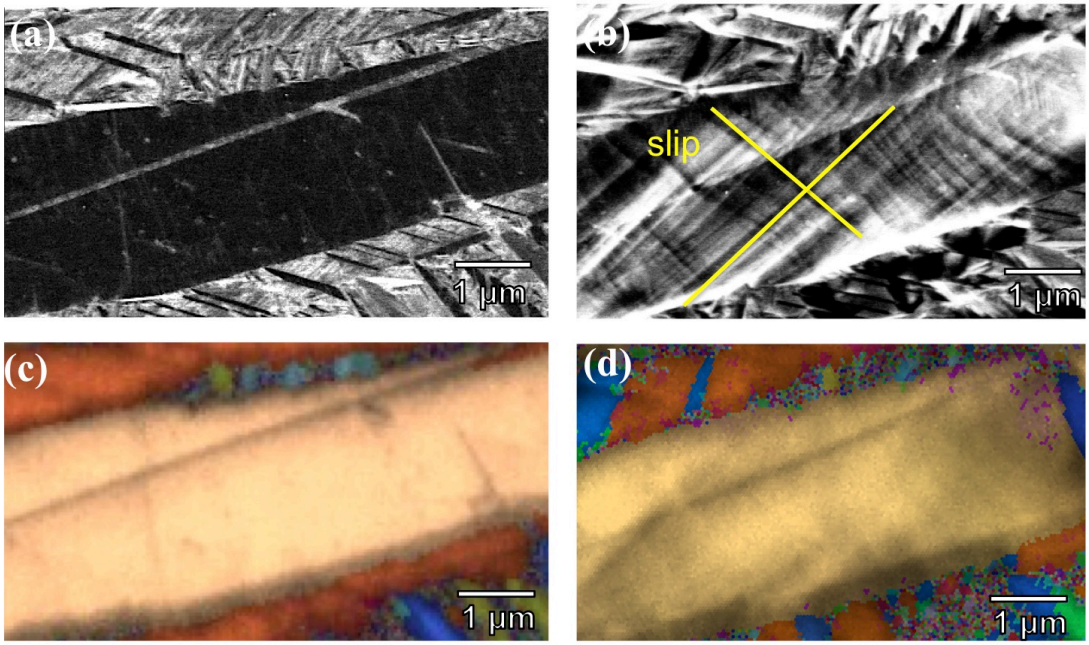

Fig. 3-12 (a) ECCI figure showing the as-quenched α″ martensite plate. (b) Corresponding deformation microstructure of (a) with 5% strain. The tensile axis is horizontal to the images. (c) and (d) Corresponding IPF combined with image quality (IQ) maps of (a) and (b), respectively.

3.2.3.3 Dislocation slip

In addition to the deformation twinning, the dislocation slips have also been induced by deformation. An example is shown in Fig. 3-12. Fig. 3-12(a) shows ECCI image of an as-quenched α″ martensite plate and Fig. 3-12(c) shows the corresponding IPF with image quality (IQ) map. With 5% strain, the ECCI image of deformation microstructure is shown in Fig. 3-12(b) and the IPF+IQ image is shown in Fig. 3-12(d). The high density of dislocation slips can be observed, which shear the same orientation with the α″ matrix. Meanwhile, two slip systems are activated upon deformation, as indicated by yellow lines in Fig. 3-12(b).

3.3 Discussion

The present study reveals that two different twinning modes are activated in the orthorhombic-α" martensite structure, *i.e.*, $\{111\}_{\alpha"}$-Type I transformation twinning and $\{112\}_{\alpha"}$-Type I deformation twinning. Crystallographic analysis of these two twinning modes will be discussed individually.

3.3.1 $\{111\}_{\alpha"}$-Type I transformation twinning

From a crystallographic standpoint, the twinning structure is formed as a result of a lattice invariant shear (LIS) to accommodate the martensitic transformation strain [44,45]. In the orthorhombic-α″ martensite structure, Inamura *et al*. [19] have proposed an approach to predict the transformation twinning system for LIS, which is based on the infinitesimal deformation theory [46]. The principal strains of the lattice correspondence variant between β and α″ phase are given as follows:

$$\varphi_1 = \frac{a_{\alpha"} - a_\beta}{a_\beta} \qquad 3-1$$

$$\varphi_2 = \frac{b_{\alpha"} - \sqrt{2}a_\beta}{\sqrt{2}a_\beta} \qquad 3-2$$

$$\varphi_3 = \frac{c_{\alpha"} - \sqrt{2}a_\beta}{\sqrt{2}a_\beta} \qquad 3-3$$

where $a_{\alpha"}$, $b_{\alpha"}$, $c_{\alpha"}$, are the lattice parameters of α″ martensite and a_β is the lattice parameter of β phase. Based on the Inamura-approach, the transformation twinning depends significantly on the sign of φ_3. $\{111\}_{\alpha"}$-Type I twinning or $<211>_{\alpha"}$-Type II twinning are possible when $\varphi_3 > 0$, otherwise $\{011\}_{\alpha"}$-compound twinning is activated when $\varphi_3 < 0$. However, $<211>_{\alpha"}$-Type II twinning is not considered here since it has been rarely observed in previous reports [19,36,47]. Considering the lattice parameters of the present alloy ($c_{\alpha"}$ = 0.4680 nm; a_β = 0.3272 nm [48]), we obtain $\varphi_3 = 0.011$. Accordingly, $\{111\}_{\alpha"}$-Type I twinning is favored in the present Ti-7.5Mo alloy, which agrees with the results shown in Fig. 3-4 and Fig. 3-5.

3.3.2 $\{112\}_{\alpha''}$-Type I deformation twinning

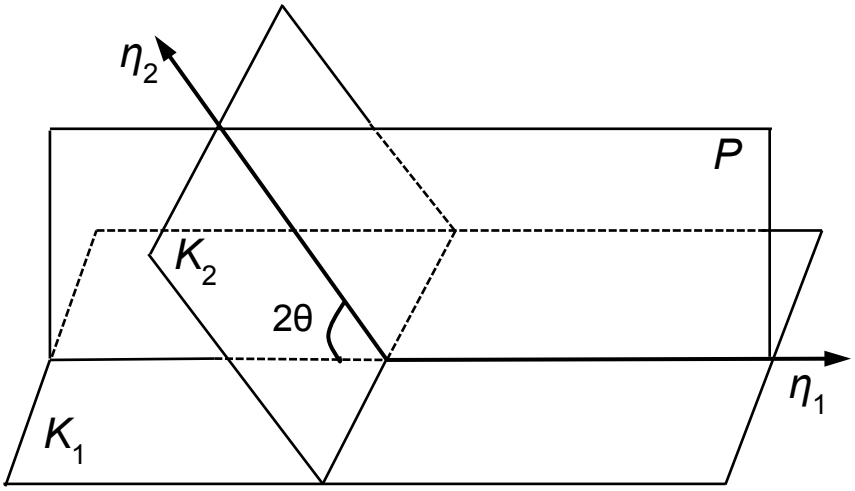

Fig. 3-13 The four crystallographic twinning elements. The twinning and the conjugate twinning planes are K_1 and K_2 and the twinning and conjugate twinning directions are η_1 and η_2, respectively. The directions η_1 and η_2 and the normals to K_1 and K_2 are all contained in the plane of shear P.

The crystallographic analysis of deformation twinning is commonly treated by the Bilby-Crocker model [49]. This model has been widely used to analyze the twinning modes in different lattice structures such as fcc [50], bcc [51], hcp [52] and lower symmetry structures [28,38]. In this model, deformation twinning is described by four crystallographic elements, namely, K_1, K_2, η_1 and η_2 (Fig. 3-13), where K_1 is the twinning plane, η_1 is the twinning direction, K_2 is the reciprocal or conjugate twinning plane, and η_2 is the reciprocal or conjugate twinning direction. In particular, the Bilby-Crocker model predicts that there are 82 possible twinning modes including 41 twinning modes and their reciprocals in the orthorhombic double lattice crystal structure [38]. Five of these twinning modes have been experimentally reported in α-uranium [53], which has an orthorhombic structure. In the present case, we describe the α" martensitic structure as an orthorhombic-α″ structure double lattice crystal structure and hence analyze the twinning modes by the Bilby-Crocker model. The crystallographic analysis is as follows.

The β→α″ martensitic transformation in β-Ti alloys has been reported with Au-Cd type lattice correspondence (Fig. 3-14(a)) [19]. The α" martensitic structure has been described as a disordered orthorhombic structure with the space group *Cmcm*, Fig. 3-14b [17,54]. The atoms at the face-centered positions (red circles in Fig. 3-13(b)) are shifted to complete the β → α″ martensitic transformation. The magnitude of this shift is δ along the *b*-axis (black arrows in Fig. 3-14(b)). According to previous reports [8,18], the orthorhombic-α″ structure in β-Ti alloys can be described as a transitional phase between the hcp-α' (δ = 1/6) and bcc-β (δ = 0) phases. The magnitude of δ in the α″ structure is restricted to $0 < \delta < 1/6$. In the present alloy, we have estimated the value of δ from the HRTEM image of the as-quenched α″ structure shown in Fig. 3-14(c). From the intensity profile shown in Fig. 3-14(d), we obtain a value of $1/2\text{-}\delta \sim 0.35$ and hence, we take δ as 0.15. This result agrees with the value of δ (~0.157) determined by Li *et al.* [18] by first-principles calculation for the Ti-7.5Mo alloy system. Subsequently, the shifted atoms result in the combination of two interpenetrating orthorhombic lattices. Thus, we consider that the disordered

orthorhombic structure can be regarded as a double lattice structure. It consists of motif units of two atoms arranged symmetrically about the lattice points of a single Bravais space lattice. Here, the motif pairs of atoms are assumed to shear as rigid bodies before the atoms shuffle to form the twinning structure.

The motif arrangement is then described as a combination of shear and shuffle. The shear magnitude s is determined by $s = 2 \cot(2\theta)$, where (2θ) is the angle between K_1 and K_2 planes (Fig. 3-13). The

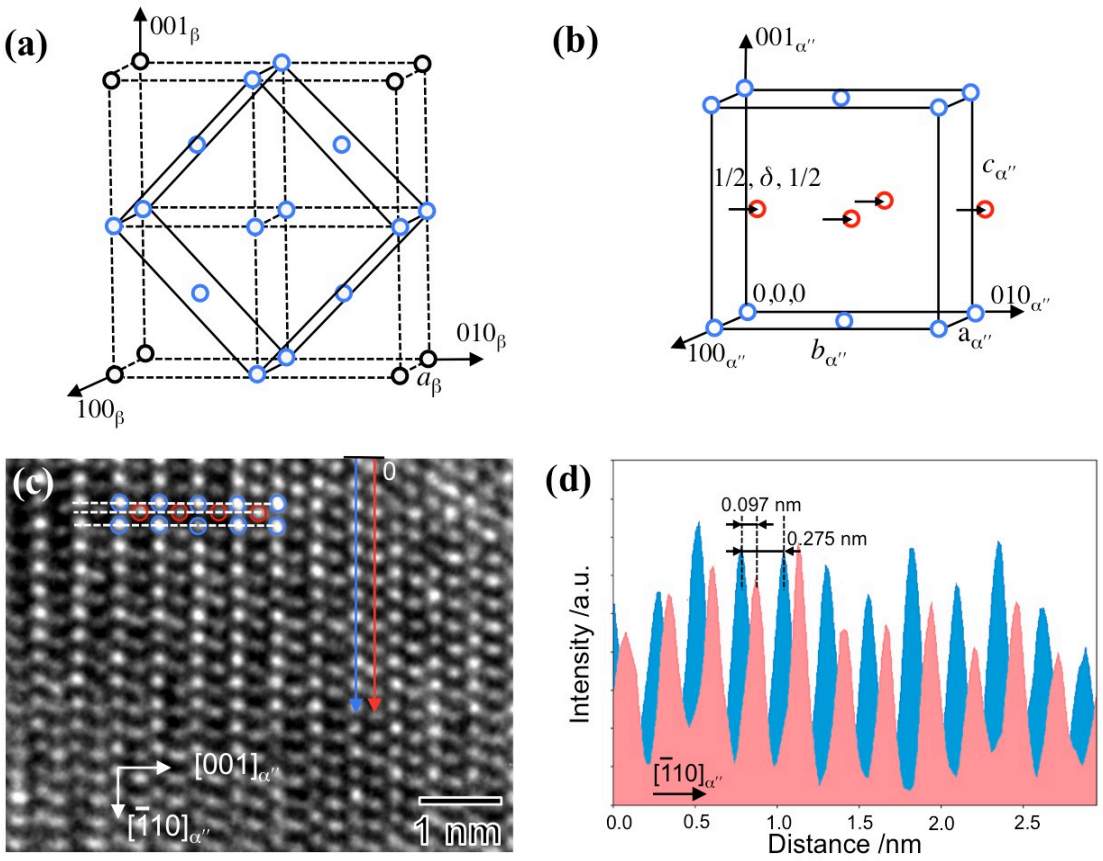

Fig. 3-14 (a) The Au-Cd type lattice correspondence between β phase and α″ phase [57]. The atoms involved in the formation of α″ phase are shown in blue circles while the corner atoms are black circles. (b) Orthorhombic structure of α″ martensite reported by Brown *et al.* [17]. The red circles indicate the shifted atoms. (c) HRTEM image of the as-quenched α″ martensite along $[110]_{\alpha''}$ zone axis. (d) Intensity profile along the lines indicated in (c).

complexity of the shuffling mechanism is directly related to the number of lattice planes (denoted by q) parallel to K_1 that are intersected by η_2 for Type I twinning, and the number of lattice planes parallel to K_2 that are intersected by η_1 for Type II twinning. In single crystal structures, each point of the Bravais lattice is sheared to its correct twin position for twinning modes with $q = 1$ or 2 and no shuffle is needed. For $q > 2$, a fraction q^{-1} of the lattice points is sheared correctly when q is odd, and a fraction $2q^{-1}$ when q is even. The remainder of the lattice points must shuffle to reach their twin positions. Therefore, small values of q are associated with simple shuffle mechanisms, which are more likely to occur. The shuffling mechanisms in the double lattice structure have been explained by the Bilby-Crocker model. The simple shuffling mechanisms with $q = 1$, 2 or 4 are schematically illustrated in Fig. 3-15. According to the Bilby-Crocker model [37], the twinning in the double lattice structures is formed first by the shears of the lattice points, and then by shuffling which include the rearrangement or disruption of the motif units. Fig. 3-15 illustrates the shuffle mechanisms for $q = 1$ and $q = 4$. As for $q = 1$, the motif units is first sheared, as shown in Fig. 3-15(a). Then

the non-disruptive rearrangement of the atoms in each pair must take place by means of the mechanisms Ia or Ib to produce the Type I twin (Fig. 3-15(b)) or by means of IIa or IIb to produce Type II twin (Fig. 3-15(c)). The shuffles involved in q = 2 are identical to those in q = 1 modes. This also applies to the non-disruptive rearrangements of the motif units at half of the lattice points in q = 4 modes. The remainders of the q = 4 are required to disrupt and form new motif units with Ic or Id for Type I twinning (Fig. 3-15 (e-f)) or with IIc or IId for Type II twinning (Fig. 3-15 (g-h)).

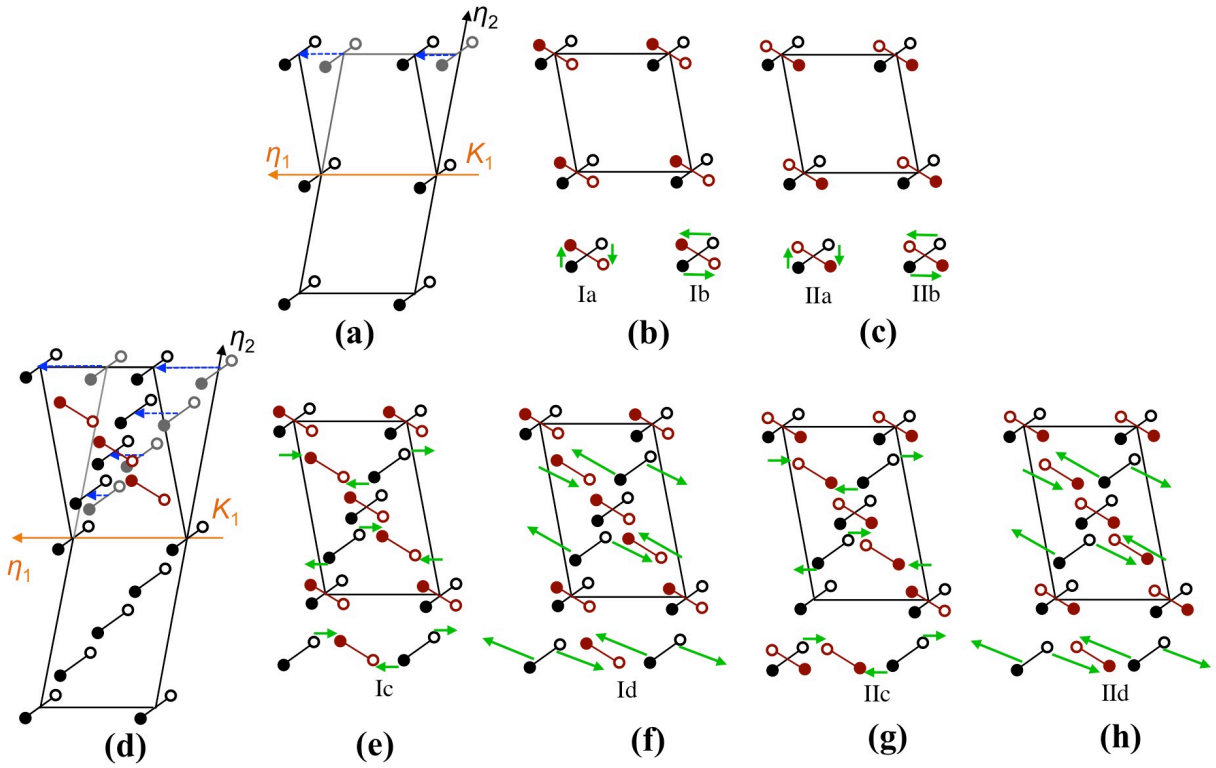

Fig. 3-15 Schematically illustration of twinning modes with q=1 (a-c) and q=4 (d-h) in double lattice structures [37]. Shear of the lattice points with q=1 (a) and q=4 (d). Shuffle mechanisms corresponding to the rearrangement of the motif units to form type I twin (b) and type II twin (c), and the disruption of the motif units to form type I twin (e and f) and type II twin (g and h). The atoms represented by closed and open circles lie above and below the paper, respectively.

First, we have calculated the twinning elements of the $\{112\}_{\alpha''}$-Type I twinning by the Bilby-Crocker theory using the lattice parameters of the α″ martensite in the present Ti-7.5Mo alloy, and they are listed in Table 3-1. The K_2 and η_1 elements have irrational Miller indices. Meanwhile, this table also shows that experimentally observed $\{112\}_{\alpha''}$-Type I twinning has the shear magnitude (s) of 0.199, which is regarded as reasonable [36-38]. For instance, Tobe *et al* [36] have reported the deformation twinning of $\{111\}_{\alpha''}$-Type I twinning in Ti-20Nb alloy with s = 01613. The mechanism of $\{112\}_{\alpha''}$-Type I twinning with q = 4 is further discussed in terms of atomic shuffles involved in the formation of deformation twinning.

Table 3-1 The twinning elements (K_1, K_2, η_1, and η_2) of the observed $\{112\}_{\alpha''}$-type I twinning in Ti-7.5Mo alloy.

K_1	K_2	η_1	η_2	*Type*	*q*	*s*
{1 1 2}	{-2.586, -1, 4.379}	<-6.463, -1, 3.732>	<3 1 2>	I	4	0.199

In order to achieve the smallest shuffle magnitude (termed Δ), the choice of the motif unit is relevant. From crystallographic standpoint, there are six distinct pairs of atoms comprising the motif unit in the disordered orthorhombic-α" structure, namely κ, λ, μ, ν, o and ξ [38]. The projection of the motif units along the $[001]_{\alpha''}$ direction is shown in Fig. 3-16. The units of κ and ξ have two equivalent variants and the units of λ, μ, o and v have four each. Accordingly, there are a total of twenty possible units and they are listed in Table 3-2, together with the vector joining the motif unit represented with [*xyz*]. The possible motif units are chosen based on the criterion that they lie almost parallel to the twinning plane and resulting in small shuffle magnitudes [38,51]. As for $\{112\}_{\alpha''}$-type I twinning with q = 4, the shuffle mechanism consists of non-disruptive (Ia or Ib) and disruptive (Ic or Id) rearrangements, as shown in Fig. 3-15. The equations for the shuffle magnitudes are shown in Table 3-3 [38]. (hkl) are the Miller indices of the twin plane K_1 for Type I twinning. In order the specify the shuffle magnitudes of Ic and Id modes, in which η_1 is irrational, a lattice vector [efg] lying in K_1 is chosen to defines the relative positions of the parent motif units. In this condition, he + kf + lg = 0 must be satisfied. In order to involve the smallest shuffle magnitudes, we set the vector [efg] to $\frac{1}{2}[20\bar{1}]$ for the $\{112\}_{\alpha''}$-type I twinning mode. Here, the shuffle mechanism with the smallest magnitude of shuffle is considered as the most possible shuffle mechanism. According to the results, the most possible motif units is decided as λ_2 with the shuffle magnitude Δ = 0.61 Å for Ia, and Δ = 1.25 Å for Ic, which is regarded as reasonable values to occur in practice [37, 38].

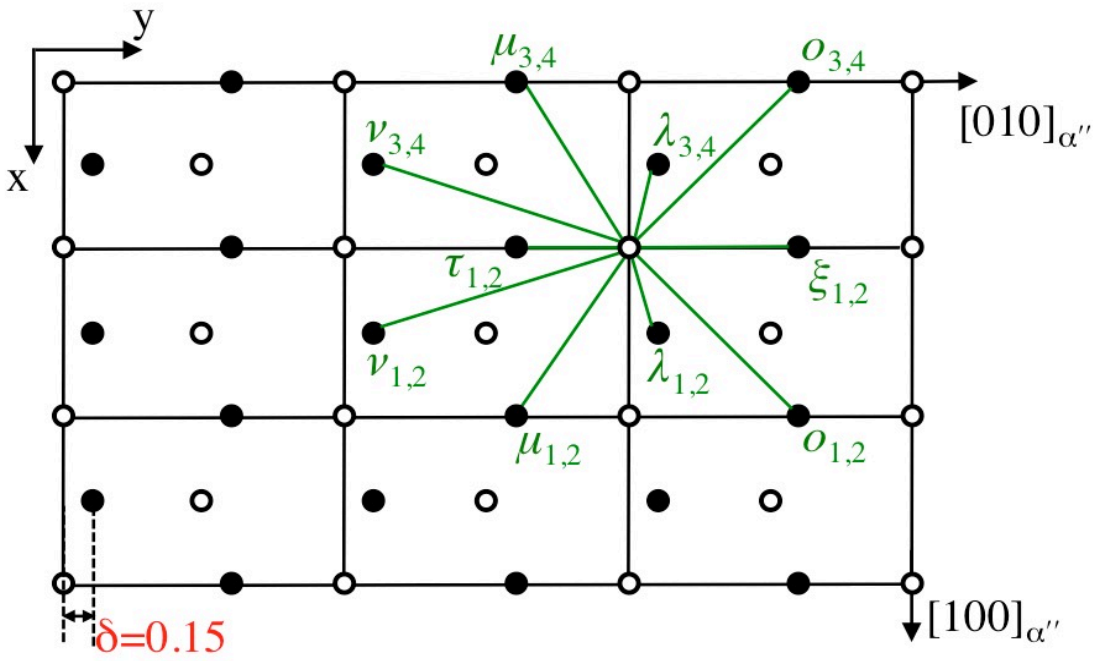

Fig. 3-16 $[001]_{\alpha''}$ Projection of the possible motif units. Open circles represent atoms in the projection plane, and close circles are atoms 1/2 c above or below the projection.

Table 3-2 Possible motif units: [*xyz*].

Unit	*x*	*y*	*z*
λ_1	0.50	0.15	0.50
λ_2	0.50	0.15	-0.50
λ_3	-0.50	0.15	0.50
λ_4	-0.50	0.15	-0.50
τ_1	0.00	-0.35	0.50
τ_2	0.00	-0.35	-0.50
ξ_1	0.00	0.65	0.50
ξ_2	0.00	0.65	-0.50
μ_1	1.00	-0.35	0.50
μ_2	1.00	-0.35	-0.50
μ_3	-1.00	-0.35	0.50
μ_4	-1.00	-0.35	-0.50
o_1	1.00	0.65	0.50
o_2	1.00	0.65	-0.50
o_3	-1.00	0.65	0.50
o_4	-1.00	0.65	-0.50
ν_1	0.50	-0.85	0.50
ν_2	0.50	-0.85	-0.50
ν_3	-0.50	-0.85	0.50
ν_4	-0.50	-0.85	-0.50

Table 3-3 Equations for shuffle magnitudes in double lattice orthorhombic structure [38].

Shuffle	*Magnitude*
Ia	$(hx+ky+lz)(h^2a^{-2}+k^2b^{-2}+l^2c^{-2})^{-1/2}=A$
Ib	$[(x^2a^2+y^2b^2+z^2c^2)-A^2]^{1/2}$
Ic	$\{[(e-2x)^2a^2+(f-2y)^2b^2+(g-2z)^2c^2]/4-A^2\}^{1/2}$
Id	$[(e^2a^2+f^2b^2+g^2c^2)-A^2]^{1/2}$

As a result, the most possible mechanism of $\{112\}_{\alpha''}$-type I twinning in Ti-7.5Mo alloy is schematically shown with the projection along the $[02\bar{1}]_{\alpha''}$ direction (Fig. 3-17). The twin plane is set in the middle of the two planes in order to have smaller interplanar spacing. The motif unit (λ_2) is illustrated with dashed lines comprised of two atoms. The atomic shear is indicated by blue arrows, and the shuffle mechanisms including non-disruptive (Ia) and disruptive (Ic) are shown in green arrows.

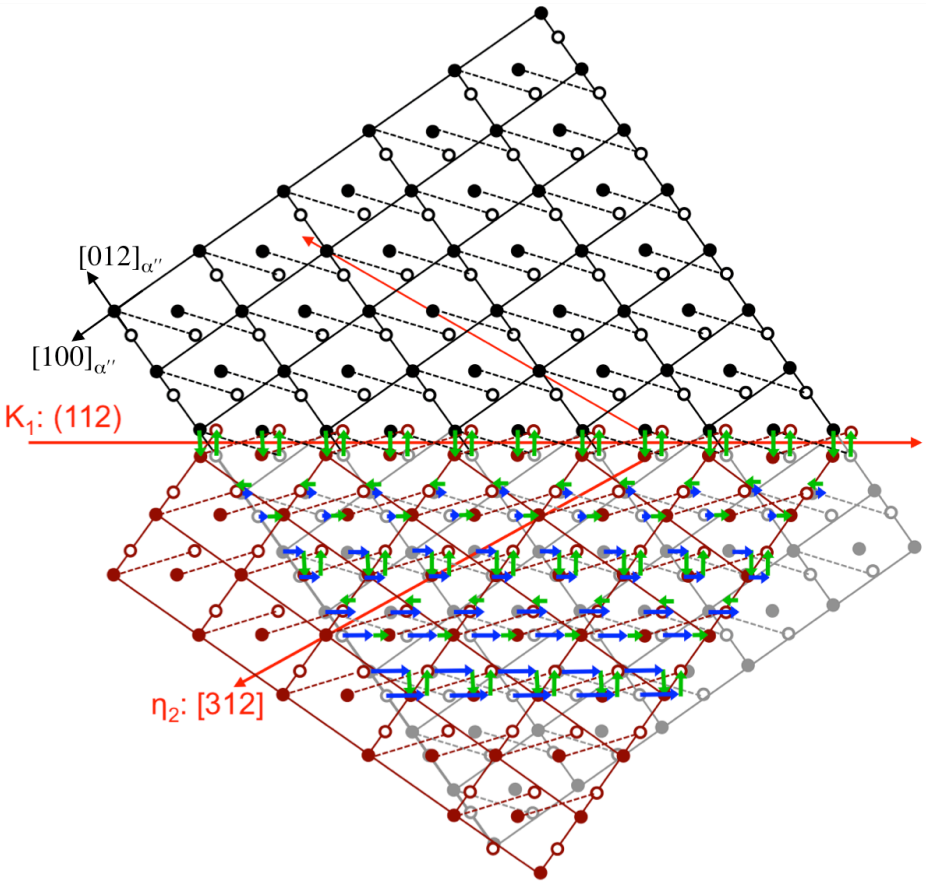

Fig. 3-17 $[02\bar{1}]_{\alpha''}$Projection of the $\{112\}_{\alpha''}$-type I twinning in the disordered orthorhombic-α" structure with δ = 15. Open circles represent atoms in the projection plane, and close circles are atoms 1/2 c above or below the projection. The blue and green arrows indicate the shear and shuffle of the motif units, respectively.

3.5. Conclusion

We have investigated the deformation behaviors of orthorhombic-α″ martensite in β Ti-7.5Mo (wt.%) alloy. Microstructure characterization was performed by using TEM and SEM (BSE and EBSD). The as-quenched α″ martensite with transformation twins was subjected into tension and deformation twins were observed. The mechanisms of deformation twinning in orthorhombic-α″ martensite were discussed. The main conclusions are drawn as follows:

(1) The as-quenched orthorhombic-α″ martensite contains $\{111\}_{\alpha''}$-Type I transformation twinning. According to the Inamura-approach related with the crystallographic features of transformation twinning in α″ martensite, the $\{111\}_{\alpha''}$-Type I twinning is induced as a lattice invariant shear to accommodate the β→α″ martensitic transformation.

(2) With 5% strain, the activation of $\{112\}_{\alpha''}$-Type I deformation twinning and dislocation slips can be identified. This twinning mode has never been reported in the orthorhombic-α″ martensite in β-Ti alloys.

(3) Based on the Bilby-Crocker model related with the crystallographic analysis of deformation twinning, the twinning mechanism the $\{112\}_{\alpha''}$-Type I twinning have been analyzed in terms of atomic shears and shuffles.

References

[1] M. Long, H.J. Rack, Titanium alloys in total joint replacement-a materials science perspective., Biomaterials. 19 (1998) 1621–1639.
[2] M. Geetha, A.K. Singh, R. Asokamani, A.K. Gogia, Ti based biomaterials, the ultimate choice for orthopaedic implants - A review, Prog. Mater. Sci. 54 (2009) 397–425.
[3] M. Niinomi, Mechanical properties of biomedical titanium alloys, Mater. Sci. Eng. A. 243 (1998) 231–236.
[4] W.F. Ho, C.P. Ju, J.H. Chern Lin, Structure and properties of cast binary Ti–Mo alloys, Biomaterials. 20 (1999) 2115–2122.
[5] Y.L. Zhou, M. Niinomi, T. Akahori, Effects of Ta content on Young's modulus and tensile properties of binary Ti-Ta alloys for biomedical applications, Mater. Sci. Eng. A. 371 (2004) 283–290.
[6] R.P. Kolli, W.J. Joost, S. Ankem, Phase Stability and Stress-Induced Transformations in Beta Titanium Alloys, JOM. 76 (2015) 1273–1280.
[7] H.Y. Kim, Y. Ikehara, J.I. Kim, H. Hosoda, S. Miyazaki, Martensitic transformation, shape memory effect and superelasticity of Ti–Nb binary alloys, Acta Mater. 54 (2006) 2419–2429.
[8] S. Banumathy, R.K. Mandal, A.K. Singh, Structure of orthorhombic martensitic phase in binary Ti-Nb alloys, J. Appl. Phys. 106 (2009).
[9] H.Y. Kim, S. Miyazaki, Martensitic Transformation and Superelastic Properties of Ti-Nb Base Alloys, Mater. Trans. 56 (2015) 625–634.
[10] H.Y. Kim, S. Hashimoto, J. Il Kim, H. Hosoda, S. Miyazaki, Mechanical Properties and Shape Memory Behavior of Ti-Nb Alloys, Mater. Trans. 45 (2004) 2443–2448.
[11] Y.L. Hao, S.J. Li, S.Y. Sun, C.Y. Zheng, Q.M. Hu, R. Yang, Super-elastic titanium alloy with unstable plastic deformation, Appl. Phys. Lett. 87 (2005) 2003–2006.
[12] S. Cai, J.E. Schaffer, Y. Ren, Deformation of a Ti-Nb alloy containing ??-martensite and omega phases, Appl. Phys. Lett. 106 (2015) 1–6.
[13] H. Matsumoto, S. Watanabe, S. Hanada, Beta TiNbSn Alloys with Low Young's Modulus and High Strength, Mater. Trans. 46 (2005) 1070–1078.
[14] D.J. Lin, C.C. Chuang, J.H. Chern Lin, J.W. Lee, C.P. Ju, H.S. Yin, Bone formation at the surface of low modulus Ti–7.5Mo implants in rabbit femur, Biomaterials. 28 (2007) 2582–2589.
[15] A.L.A. Escada, D. Rodrigues, J.P.B. Machado, A.P.R.A. Claro, Surface characterization of Ti-7.5Mo alloy modified by biomimetic method, Surf. Coatings Technol. 205 (2010) 383–387.

[16] Y.C. Chen, J.H.C. Lin, C.P. Ju, Effects of post-aging cooling condition on structure and tensile properties of aged Ti–7.5Mo alloy, Mater. Des. 54 (2014) 515–519.
[17] A.R.G. Brown, D. Clark, J. Eastabrook, K.S. Jepson, The Titanium–Niobium System, Nature. 201 (1964) 914–915.
[18] C.X. Li, H. Bin Luo, Q.M. Hu, R. Yang, F.X. Yin, O. Umezawa, L. Vitos, Lattice parameters and relative stability of α″ phase in binary titanium alloys from first-principles calculations, Solid State Commun. 159 (2013) 70–75.
[19] T. Inamura, J.I. Kim, H.Y. Kim, H. Hosoda, K. Wakashima, S. Miyazaki, Composition dependent crystallography of α ″-martensite in Ti–Nb-based β-titanium alloy, Philos. Mag. 87 (2007) 3325–3350.
[20] T. Inamura, H. Hosoda, H. Young Kim, S. Miyazaki, Antiphase boundary-like stacking fault in α″-martensite of disordered crystal structure in β-titanium shape memory alloy, Philos. Mag. 90 (2010) 3475–3498.
[21] A. V. Dobromyslov, G. V. Dolgikh, Y. Dutkevich, T.L. Trenogina, Phase and structural transformations in Ti-Ta alloys, Phys. Met. Metallogr. 107 (2009) 502–510.
[22] A.G. Crocker, Twinned martensite, Acta Metall. 10 (1962) 113–122.
[23] C. Li, G. Li, Y. Yang, M. Varlioglu, K. Yang, α″ Martensitic Twinning in Alpha + Beta Ti-3.5Al-4.5Mo Titanium Alloy, J. Metall. 2011 (2011) 1–5.
[24] C.H. Wang, C.D. Yang, M. Liu, X. Li, P.F. Hu, A.M. Russell, G.H. Cao, Martensitic microstructures and mechanical properties of as-quenched metastable β-type Ti–Mo alloys, J. Mater. Sci. 51 (2016) 6886–6896.
[25] Y.W. Chai, H.Y. Kim, H. Hosoda, S. Miyazaki, Self-accommodation in Ti-Nb shape memory alloys, Acta Mater. 57 (2009) 4054–4064.
[26] E. Bertrand, P. Castany, Y. Yang, E. Menou, T. Gloriant, Deformation twinning in the full-α″ martensitic Ti-25Ta-20Nb shape memory alloy, Acta Mater. 105 (2016) 94–103.
[27] S.Q. Wu, D.H. Ping, Y. Yamabe-Mitarai, T. Kitashima, G.P. Li, R. Yang, Microstructural characterization on martensitic α″ phase in Ti-Nb-Pd alloys, J. Alloys Compd. 577 (2013) 2011–2014.
[28] D.H. Ping, Y. Yamabe-Mitarai, C.Y. Cui, F.X. Yin, M. a. Choudhry, Stress-induced α″ martensitic (110) twinning in β-Ti alloys, Appl. Phys. Lett. 93 (2008) 151911.
[29] K.A. Bywater, J.W. Christian, Martensitic transformations in titanium-tantalum alloys, Philos. Mag. 25 (1972) 1249–1273.
[30] C.C. Chung, S.W. Wang, Y.C. Chen, C.P. Ju, J.H. Chern Lin, Effect of cold rolling on structure and tensile properties of cast Ti-7.5Mo alloy, Mater. Sci. Eng. A. 631 (2015) 52–66.
[31] D.J. Lin, J.H. Chern Lin, C.P. Ju, Structure and properties of Ti–7.5Mo–xFe alloys, Biomaterials. 23 (2002) 1723–1730.
[32] Y.L. Hao, R. Yang, M. Niinomi, D. Kuroda, Y.L. Zhou, K. Fukunaga, A. Suzuki, Young's modulus and mechanical properties of Ti-29Nb-13Ta-4.6Zr in relation to α″ martensite, Metall. Mater. Trans. A. 33 (2002) 3137–3144.
[33] X.H. Min, X.J. Chen, S. Emura, K. Tsuchiya, Mechanism of twinning-induced plasticity in β-type Ti–15Mo alloy, Scr. Mater. 69 (2013) 393–396.
[34] S. Hanada, O. Izumi, Correlation of tensile properties, deformation modes, and phase stability in commercial β-phase titanium alloys, Metall. Trans. A. 18 (1987) 265–271.
[35] X. Ji, S. Emura, X. Min, K. Tsuchiya, Strain-rate effect on work-hardening behavior in β-type Ti-10Mo-1Fe alloy with TWIP effect, Mater. Sci. Eng. A. 707 (2017) 701–707.
[36] H. Tobe, H.Y. Kim, T. Inamura, H. Hosoda, T.H. Nam, S. Miyazaki, Effect of Nb content on deformation behavior and shape memory properties of Ti–Nb alloys, J. Alloys Compd. 577 (2013) S435–S438.
[37] B.A. Bilby, A.G. Crocker, The Theory of the Crystallography of Deformation Twinning, Proc. R. Soc. A. 288 (1965) 240–255.
[38] A.G. Crocker, The crystallography of deformation twinning in alpha-uranium, J. Nucl. Mater. 16 (1965) 306–326.
[39] W.F. Ho, A comparison of tensile properties and corrosion behavior of cast Ti-7.5Mo with c.p. Ti, Ti-15Mo and Ti-6Al-4V alloys, J. Alloys Compd. 464 (2008) 580–583
[40] Y.W. Chai, H.Y. Kim, H. Hosoda, S. Miyazaki, Interfacial defects in Ti-Nb shape memory alloys, Acta Mater. 56 (2008) 3088–3097.
[41] Y.F. Zheng, W. Cai, J.X. Zhang, L.C. Zhao, H.Q. Ye, Microstructural development inside the stress induced martensite variant in a Ti-Ni-Nb shape memory alloy, Acta Mater. 48 (2000) 1409–1425.

[42] T. Ahmed, H.J. Rack, Martensitic transformations in Ti- (16-26 at %) Nb alloys, J. Mater. Sci. 31 (1996) 4267–4276.
[43] K.M. Knowles, D.A. Smith, The nature of the parent-martensite interface in titanium-manganese, Acta Metall. 29 (1981) 1445–1466.
[44] J.. Bowles, J.. Mackenzie, The crystallography of martensite transformations I, Acta Metall. 2 (1954) 129–137.
[45] J.S. Bowles, J.K. Mackenzie, The crystallography of martensite transformations III. Face-centred cubic to body-centred tetragonal transformations, Acta Metall. 2 (1954) 224–234.
[46] Y. Liang, H. Kato, M. Taya, T. Mori, Infinitesimal approach to the crystallography of martensitic transformation: application to Ni-Ti, Scr. Mater. 43 (2000) 535–540.
[47] K.A. Bywater, J.W. Christian, Martensitic transformations in titanium-tantalum alloys, Philos. Mag. 25 (1972) 1249–1273.
[48] B. Predel, Mo-Ti, in: O. Madelung (Ed.), Landolt-Börnstein - Gr. IV Phys. Chem., Springer Berlin Heidelberg, Berlin/Heidelberg, 1997: pp. 1–3.
[49] J.W. Christian, S. Mahajant, Deformation Twinning, Prog. Mater. Sci. 39 (1995) 1–157.
[50] N. Marek, Dislocations and twinning in face centered cubic crystals, in: F.R.N. Nabarro, J.P. Hirth (Eds.), Dislocations in Solids, Elsevier Science, 2007: pp. 263–364.
[51] H. Tobe, H.Y. Kim, T. Inamura, H. Hosoda, S. Miyazaki, Origin of {332} twinning in metastable β-Ti alloys, Acta Mater. 64 (2014) 345–355.
[52] R.C. Pond, J.P. Hirth, A. Serra, D.J. Bacon, Atomic displacements accompanying deformation twinning: shears and shuffles, Mater. Res. Lett. 4 (2016) 185–190.
[53] J.S. Daniel, B. Lesage, P. Lacombe, The influence of temperature on slip and twinning in uranium, Acta Metall. 19 (1971) 163–173.
[54] R. Davis, H.M. Flower, D.R.F. West, Martensitic transformations in Ti-Mo alloys, J. Mater. Sci. 14 (1979) 712–722.

Chapter 4 Effect of oxygen addition on microstructures and mechanical properties of Ti-7.5Mo alloy

4.1 Introduction

Titanium and its alloys have been extensively developed in biomedical applications with their advantages such as light weight, low Young's modulus, high corrosion resistance and superior biocompatibility [1-3]. For example, the well-known Ti-6Al-4V alloy has a Young's modulus about 110 GPa, which is much lower than that of other alloys, such as stainless steel (~200 GPa) or Co-Cr-Mo alloys (~210 GPa) [4]. However, the release of Al and V ions has been considered with long-term health issues [5]. Meanwhile, the modulus of Ti-6Al-4V is still relatively higher than that of our human bones (~30 GPa), which may contribute to "stress shielding" effect [1,6]. Recently, several novel β-Ti alloys have been developed as biomaterials with lower modulus, superior formability and non-toxic elements (*i.e.* Al- and V-free), such as Ti-7.5Mo (wt.%) [7,8], Ti-15Mo (wt.%) [9], Ti-29Nb-13Ta-4.6Zr (wt.%, TNTZ) [3] and Ti–24Nb–4Zr–7.9Sn (wt.%) [10] alloys. In particular, with the low Young's modulus (~65 GPa) [11] and excellent bone-implant interaction [12], the Ti-7.5Mo alloy with an orthorhombic crystal structure (α" martensite) has been regarded as a promising candidate for biomedical applications. The orthorhombic-α" phase in Ti-7.5Mo alloy is obtained through martensitic transformation from bcc-β matrix upon water quenching [13]. However, the main drawback of this alloy is the relatively low mechanical strength in as-quenched state. These alloys with high mechanical strength, low modulus together with good biocompatibility are always needed for the further development of biomedical applications.

It is well acknowledged that the mechanical properties of titanium alloys are significantly dependent on the interstitial atoms such as oxygen, nitrogen, carbon and hydrogen [14-16]. Extensive studies have revealed oxygen as an effective element to improve the strength of titanium alloys with solid-solution strengthening effect [17-19]. For example, the tensile strength of Ti-29Nb-13Ta-4.6Zr alloy has been revealed intensely increasing with increasing the oxygen content (0.1~0.4 wt.%) [20]. Moreover, the oxygen has been reported to play an important role in the β→α″ martensitic transformation [17,21,22]. For example, the suppression of β→α″ martensitic transformation as a result of the addition of oxygen atoms has been invesitigated in Ti-Nb-based alloys [22]. However, the effects of oxygen on the mechanical properties and microstructures of orthorhombic-α" martensite in Ti-Mo alloys are still not understood.

The aim of the present study is to investigate the effect of oxygen on the microstructure and mechanical properties of Ti-7.5Mo alloy. We developed a series of Ti-7.5Mo alloys with various oxygen additions (0~0.5 wt.%). The microstructures were investigated by SEM and TEM. The crystal structure and phase stability of α" martensite in the developed alloys was examined on the basis of XRD and differential scanning calorimeter (DSC) techniques. Hardness and tensile tests were performed to illustrate strengthening

mechanism caused by different oxygen contents. With the results of the present study, we provide an effective method to develop novel alloys for biomedical application.

4.2 Results and discussion

4.2.1 Effect of oxygen on phase constitution

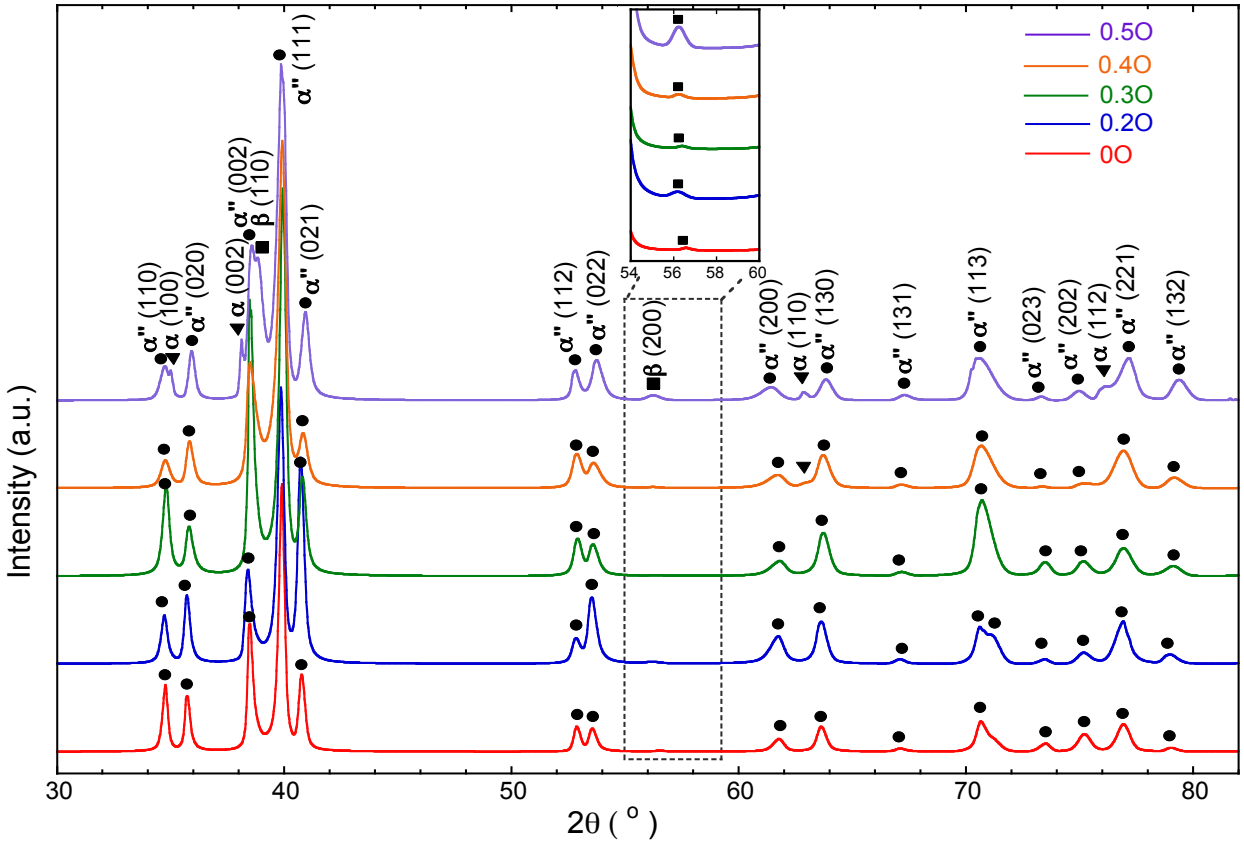

Fig. 4-1 XRD profiles of the as-quenched Ti-7.5Mo-xO (x = 0, 0.2, 0.3, 0.4 and 0.5 (wt.%)) alloys.

Fig. 4-1 shows the XRD profiles of the as-quenched Ti-7.5Mo-xO (x = 0, 0.2, 0.3, 0.4 and 0.5 (wt.%)) alloys. The orthorhombic-α″ martensite has been observed as the main phase in all the as-quenched samples. The bcc-β phase also exists in each sample, as can be seen from the inset, which enlarges the $(200)_\beta$ reflection at 2θ = 55.8°. The peak intensity may suggest that the volume fraction of prior β phase is much lower, as compared to those of α″ phase. This implies that the martensitic transformation β→α″ seems to almost complete upon water quenching. It is worth noting that the $(200)_\beta$ peak intensity is significantly increased in 0.5O alloy. Furthermore, the additional $(110)_\beta$ reflection at 2θ = 38.7° is identified in 0.5O alloy. These results imply that the high oxygen content (~0.5 wt.%) may lead to the suppression of β→α″ martensitic transformation, which consists with the previous reports [21,23]. According to the theory related with martensitic nucleation proposed by Ghosh and Olson [24,25], the interstitial elements (such as oxygen in the present study) may induce extra local strain fields, which act as obstacles to the dislocation movement and thus increase the frictional work against the motion of martensite interface.

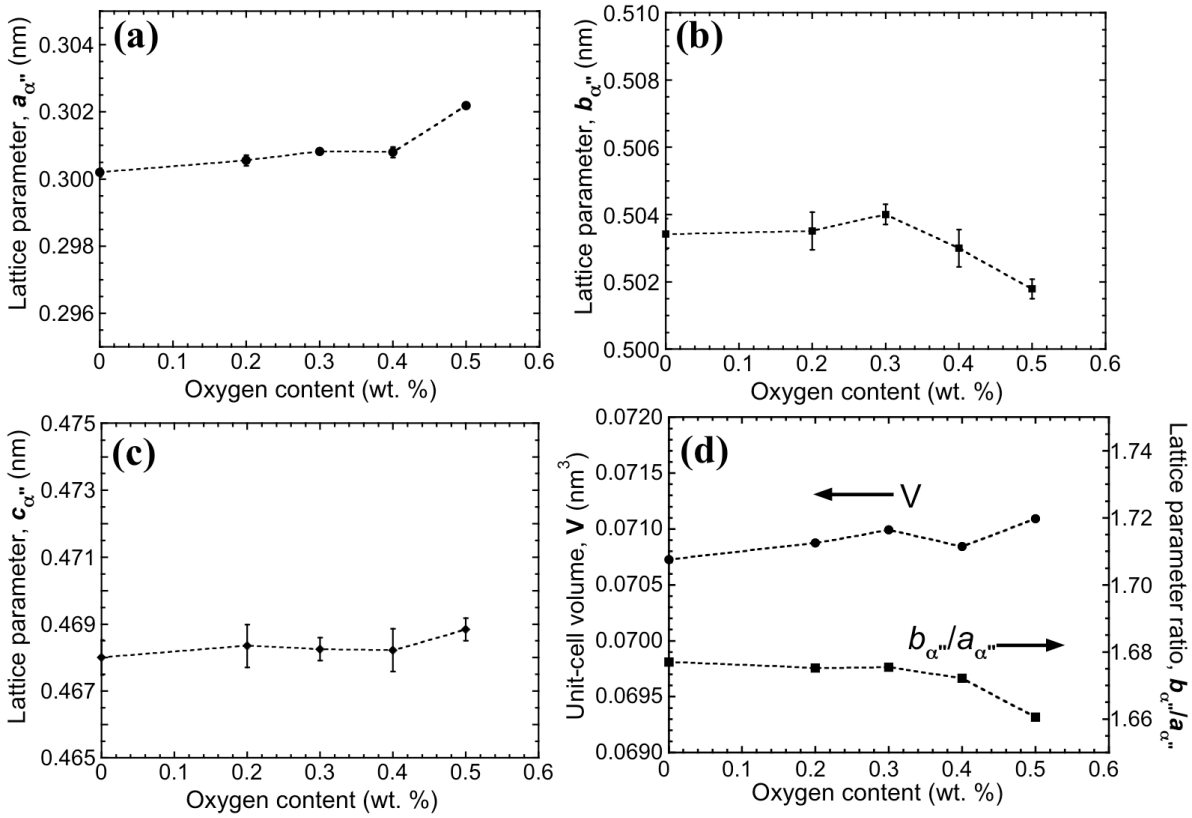

Fig. 4-2 The lattice parameters of orthorhombic-α″ martensite: (a) $a_{\alpha''}$-axis, (b) $b_{\alpha''}$-axis, (c) $c_{\alpha''}$-axis, and (d) the unit cell volume (V) and the axis ratio $b_{\alpha''}/a_{\alpha''}$.

It is worth noticing that in Fig. 4-1 an additional $(11\bar{2}0)_{\alpha}$ reflection, which locates at $2\theta = 62.8°$, has been identified in the as-quenched 0.4O sample. More α phase exist in the 0.5O sample, as shown by the increasing number and intensity of α peaks with increasing the oxygen additions to 0.5 wt.%. This may suggest that the β transus of Ti-7.5Mo alloy is increased by the addition of interstitial oxygen.

Lattice parameters of α″ martensite in the 0~0.5O alloys were measured by the XRD profiles and the results are displayed in Fig. 4-2. The $a_{\alpha''}$ and $c_{\alpha''}$ of the orthorhombic-α″ phase slightly increase whereas the $b_{\alpha''}$ decreases with increasing oxygen additions. The unit-cell volume of the orthorhombic-α″ phase in Fig. 4-2(d) increases with increasing the oxygen additions, suggesting that the oxygen dissolves in the α″ martensite as interstitial element [26]. Orthorhombic-α″ martensite is regarded as a transitional phase between bcc-β ($b/a = \sqrt{2}$) and hcp-α/α′ (($b/a = \sqrt{3}$). As indicated in Fig. 4-2(d), the orthorhombicity, *i.e.*, $b_{\alpha''}/a_{\alpha''}$, decreases with increasing the oxygen contents.

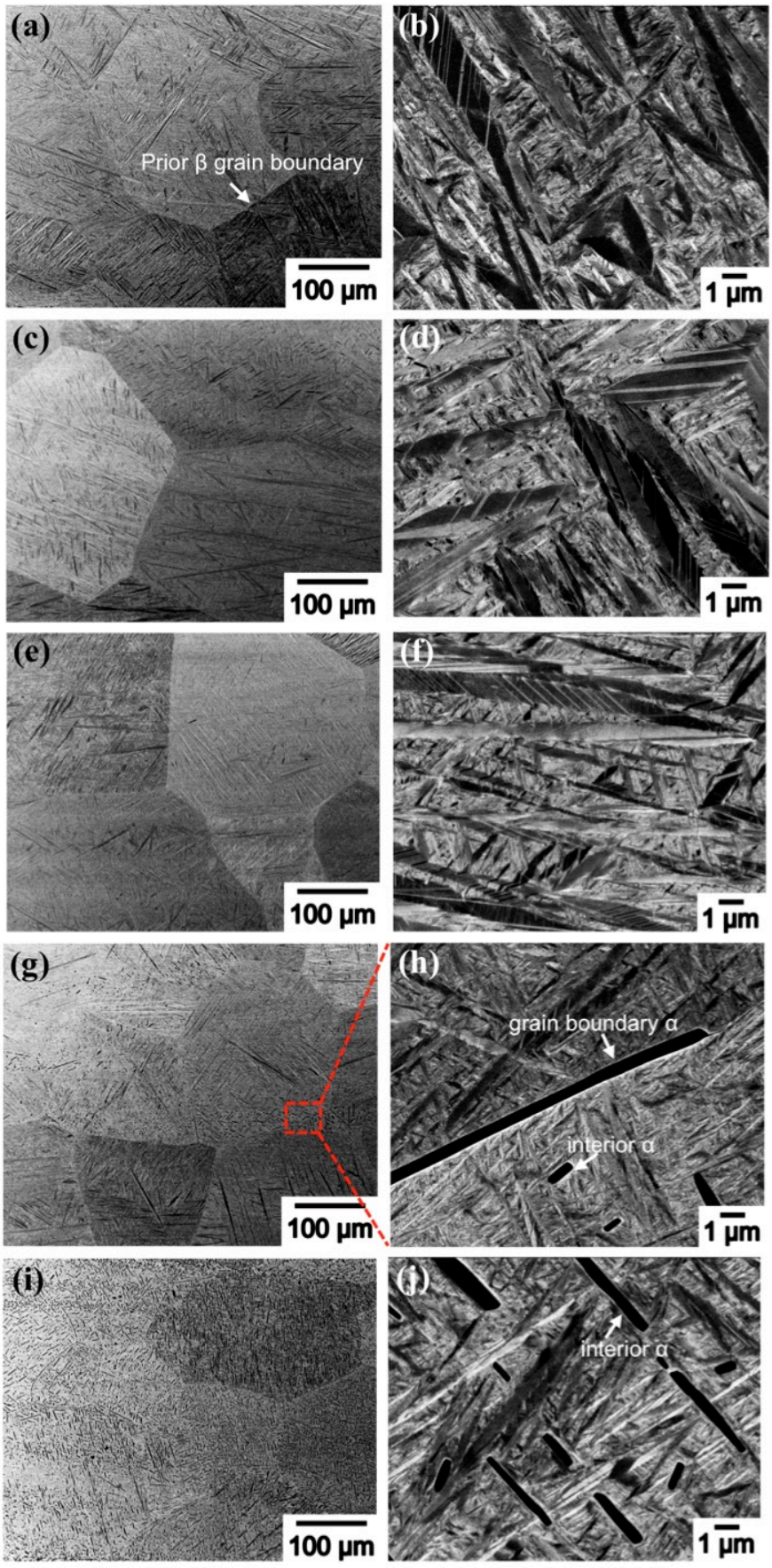

Fig. 4-3 Low- and high-magnification BSE images of the as-quenched microstructures of Ti-7.5Mo alloys with different oxygen contents: (a)-(b) 0O, (c)-(d) 0.2O, (e)-(f) 0.3O, (g)-(h) 0.4O, ((h) is taken from the grain boundary area as indicated by the red box in (g)), and (i)-(j) 0.5O.

4.2.2 Effect of oxygen on microstructures

Fig. 4-3 shows BSE images of the as-quenched Ti-7.5Mo alloys with different levels of oxygen. The prior β grain boundaries can be identified in each sample. For instance, one of the boundaries is indicated by the white arrow in Fig. 4-3(a). Fine, acicular α″ martensite plates are observed distributing homogeneously over the prior β matrix grains. From the corresponding high-magnification images, *i.e.*, Fig. 4-3(b) of 0O, Fig. 4-3(d) of 0.2O, and Fig. 4-3(f) of 0.3O alloy, it can be clearly observed that the α″ martensite plates with an average thickness of ~1 μm have internal lamellas. Fig. 4-3(h) displays the microstructure taken from the grain boundary area in Fig. 4-3(g) of 0.4O alloy. The precipitated α plates are shown along the grain boundary and in the grain interior. This agrees with the XRD result shown in Fig. 4-1, where the additional α peak is firstly identified in 0.4O alloy. Moreover, the α precipitates in Fig. 4-3(h) display lenticular morphology with the size of a few micrometers in length and a few hundred nanometers in thickness. Fig. 4-3(i) and (j) indicate the microstructures of 0.5O alloy. The α plates uniformly distribute in the grain interior and along the grain boundary. As measured by the Image J software, the area fraction of α phase is ~7%, which is higher than that of 0.4O (~2%). The increasing area fraction of α phase with increasing oxygen additions is also consistent with the XRD result shown in Fig. 4-1.

In order to identify the substructure of α″ martensite plates, TEM observations were carried out on the 0O (Fig. 4-4) and 0.5O (Fig. 4-5) alloys. Fig. 4-4(a) shows the bright-field (BF) image of the α" plate in 0O

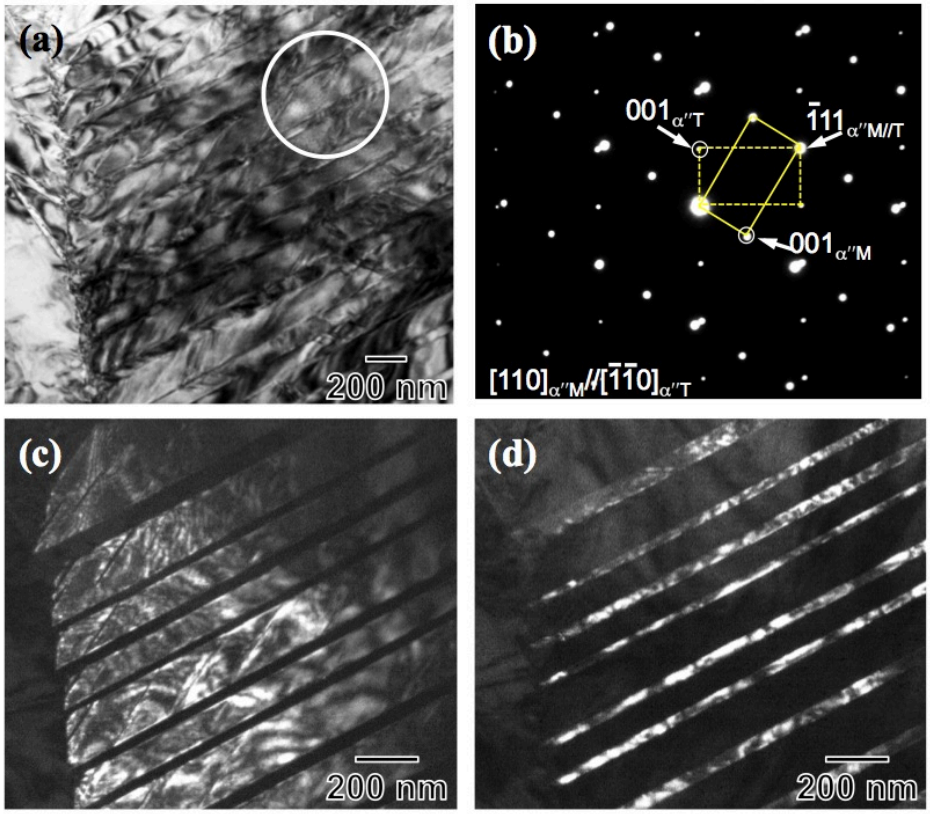

Fig. 4-4 (a) Bright field (BF) image of the as-quenched α″ phase with internal lamellas in the 0O alloy. (b) SAED pattern taken from the white circled region in (a). (c) and (d) DF images taken from spots indicated by the white circles in (b). The subscripts "M" and "T" indicate matrix and twin, respectively.

alloy. It has internal lamellas with a thin thickness of ~40 nm. Fig. 4-4(b) indicates the SAED pattern taken from the white circle in Fig. 4- 4(a). The diffraction pattern indicates two sets of spots of the $[110]_{\alpha''}$ zone axis, which have a twinning relationship with the twin plane of $(\bar{1}11)_{\alpha''}$. Fig. 4-4(c) and Fig. 4-4(d) show the corresponding DF images, in which the plates with bright contrast correspond to twin crystals. These results suggest that the internal lamellas have a $\{111\}_{\alpha''}$ twinning plane with the α″ matrix, and accordingly, they are $\{111\}_{\alpha''}$-Type I twins [27]. This is consistent with previous reports of α″ martensite in several β-Ti alloys such as Ti-Mo [28-30], Ti-Nb [22,27], and Ti-Ta [31] alloys.

TEM image in Fig. 4-5(a) shows the microstructure of the as-quenched 0.5O sample, which includes orthorhombic-α″ and hcp-α plates. Fig. 4-5(b) displays the SAED pattern of the $[\bar{2}4\bar{2}3]_{\alpha}$ zone taken from the circled region in Fig. 4-5(a). The corresponding DF image (Fig. 4-5(c)) shows the morphology of α phase with the length of ~4.3 μm and the thickness of ~450 nm. This is consistent with those of the α plates in BSE images (Fig. 4-3(g)-(j)). The SAED pattern of Fig. 4-5(d) and the corresponding DF images of Fig. 4-5(e) and (f) imply that the substructure in the α" plate of 0.5O alloy has the identical twinning system as that of 0O alloy, which is $\{111\}_{\alpha''}$-Type I twinning.

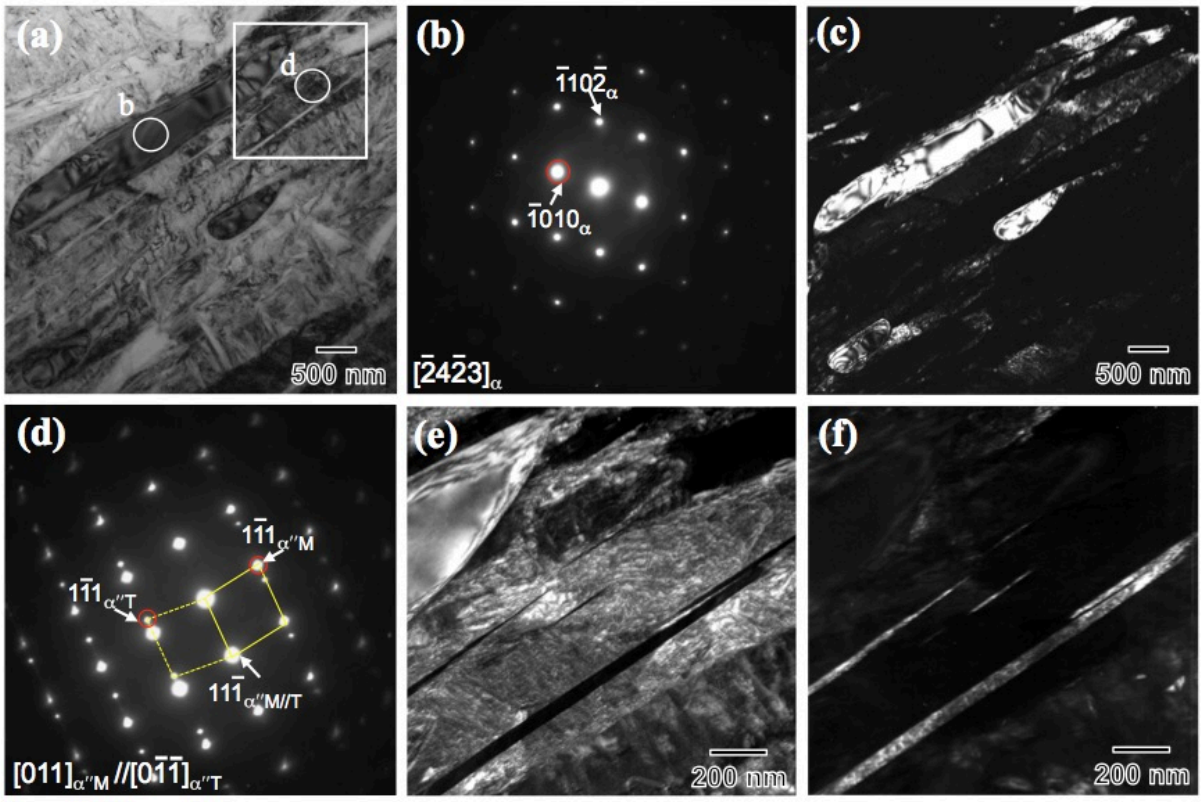

Fig. 4-5 (a) TEM image of the as-quenched microstructure of 0.5O alloy. (b) SAED pattern of the $[\bar{2}4\bar{2}3]_{\alpha}$ zone axis taken from the white circled region marked by "b" in (a). (c) Corresponding DF image taken from the spot indicated by red circle in (b). (d) SAED pattern taken from the region marked by "d" in (a) with the beam $[011]_{\alpha''M}//[0\bar{1}\bar{1}]_{\alpha''T}$. (e) and (f) DF images taken from the spots of matrix and twin indicated by red circles in (d), respectively. The images of (e) and (f) are taken from the white-boxed region in (a).

From a crystallographic standpoint, the internal twinning of α" plates are reported to accommodate the β→α" martensitic transformation strain [32]. In the orthorhombic-α″ martensite, the transformation twinning system can be estimated by an approach proposed by Inamura *et al.* [33], based on the infinitesimal

deformation theory [34]. According to this approach, one of the principal strains of the β→α″ transformation, termed $\varphi_3 = (c_{\alpha''} - \sqrt{2}a_\beta)/(\sqrt{2}a_\beta)$, is calculated ($c_{\alpha''}$ is the c-axis lattice constant of orthorhombic-α″ martensite and a_β is the lattice constant of bcc-β phase). As discussed in 3-3-1, we obtain φ_3 = 0.011 for 0O alloy. Consequently, $\{111\}_{\alpha''}$-Type I twinning is preferred. The lattice constants of α" and β phases depends significantly on the chemical composition [35,36,37]. As indicated in Fig. 4-2(c), the $c_{\alpha''}$ of 0.5O alloy slightly increases with the addition of oxygen. While it is not easy to estimate the value of a_β in 0.5O alloy, the identical twinning system is observed in 0.5O alloy, *i.e.*, $\{111\}_{\alpha''}$-Type I twinning displayed in Fig. 4-5(d). Based on the SEM/TEM results, it is summarized that oxygen addition (0~0.5 wt.%) is less relevant in the crystallographic features of α″ martensite. However, it plays a role in promoting the precipitation of α phase in Ti-7.5Mo alloy during solution-treated at 1173 K.

4.2.3 Effect of oxygen on thermal stability of α", α and β phases

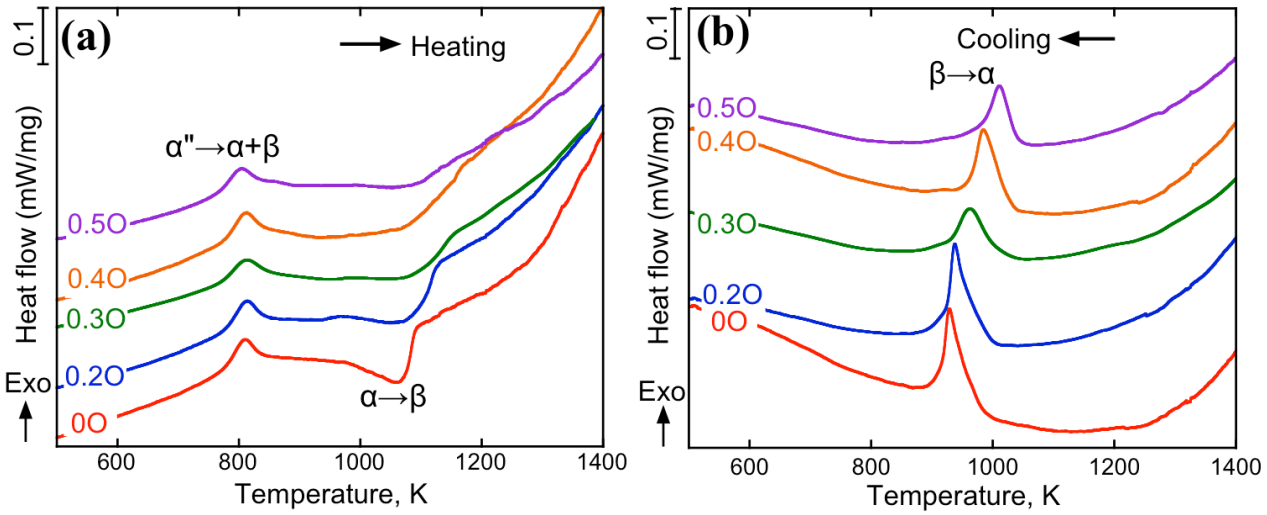

Fig. 4-6 Differential scanning calorimeter results of prepared Ti-7.5Mo alloys with different oxygen contents during (a) heating, and (b) cooling.

The thermal stability of the as-quenched Ti-7.5Mo-xO (x = 0, 0.2, 0.3, 0.4 and 0.5 (wt.%)) alloys has been investigated by DSC method. Fig. 4-6 displays the results of DSC measurements during heating (Fig. 4-6(a)) and cooling (Fig. 4-6(b)) curves. As shown in the heating process of Fig. 4-6(a), all the compared alloys show an exothermic reaction at the temperature around 810 K. This reaction is regarded as the decomposition of the metastable α″ phase into α and β phases, *i.e.*, α"→α+β [29]. The peak temperatures of 0~0.5O alloys are relatively similar. With increasing the temperature, the additional endothermic reactions can be clearly identified in 0O and 0.2O alloys. They refer to the diffusional α→β transformation [38], with the peak temperature of 0O alloy lower than that of 0.2O alloy. In the cooling process shown in Fig. 4-6(b), the exothermic reaction in all alloys corresponds to the β→α transformation. It is clear that with an increase in oxygen content, there is a significantly increase of the β→α peak temperature. As displayed in Fig. 4-6(b),

the peak temperature increases by ~90 K with increasing the oxygen content up to 0.5 wt.%. It suggests that the intestinal oxygen atoms stabilize α phase in Ti-7.5Mo alloy, which is consistent with the previous reports [39-41]. Furthermore, the DSC figures also explain the additional α phase detected in high oxygen alloys of 0.4O and 0.5O alloys (Figs. 4-1, 4-3 and 4-5). Based on the Ti-Mo phase diagram, the β transus of 0O alloy is estimated to be ~1083K [42]. With increasing the oxygen addition, the β transus of 0.4O and 0.5O alloys are expected to increase towards the solution-treatment temperature (~1173 K). Consequently, the precipitation of α phase occurs. It is worth noticing that with the stabilized α phase with increasing oxygen contents, the α→β reaction during heating becomes more difficult to be activated. This may explain the absence of endothermic α→β reaction of 0.3~0.5O alloys in Fig. 4-6(a).

4.2.4 Effect of oxygen on mechanical properties

4.2.4.1 Vickers micro-hardness

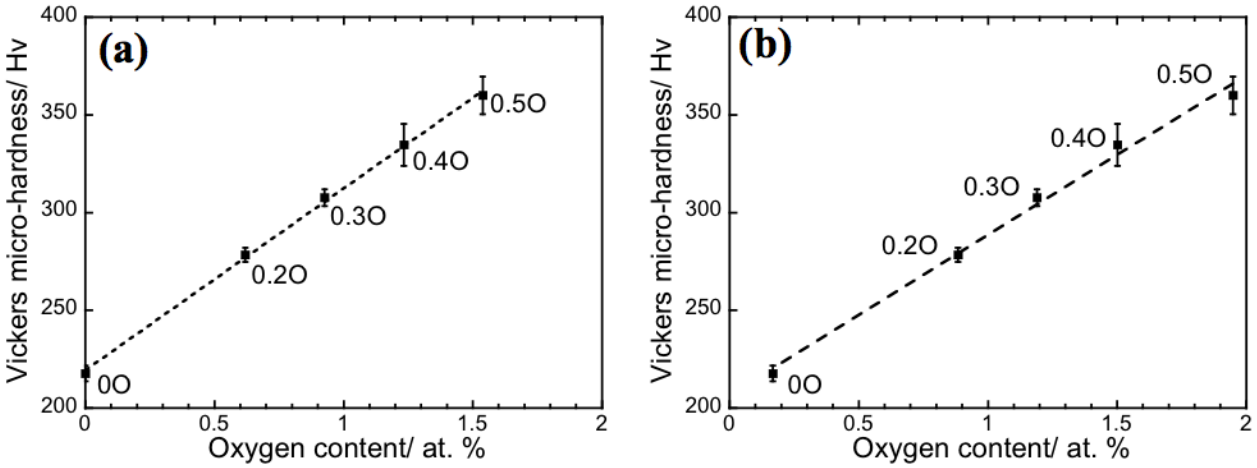

Fig. 4-7 The results of Vickers micro-hardness on the (a) nominal and (b) actual oxygen contents.

The Vickers micro-hardness of the prepared Ti-7.5Mo-xO alloys is plotted with the oxygen contents in Fig. 4-7, including the nominal (Fig. 4-7(a)) and measured (Fig. 4-7(b) values of oxygen contents. In particular, the oxygen content is expressed in atomic percent (at.%). The hardness increases linearly from 218 Hv of 0O alloy to 360 Hv of 0.5O alloy. The linear relationship in Fig. 4-7(a) is well fitted by the following equations:

$$Hv = 219.5 + 92.9\ [O],\ R^2 = 0.999 \quad 4\text{-}1$$

where H_V the hardness value, [O] is the oxygen content (in at.%) and R^2 is the regression coefficient. While the linear relationship in Fig. 4-7(b) is

$$Hv = 206.6 + 81.8\ [O],\ R^2 = 0.993 \quad 4\text{-}2$$

It can be observed that both equations exhibit high regression coefficients. The linearly increasing hardness with increasing the oxygen content can be attributed to the solid-solution strengthening effect caused by the addition of interstitial oxygen atoms [14,17-19]. It has been reported that the interstitial oxygen atoms

occupy the octahedral sites in the orthorhombic-α″ phase [36]. The lattice strain field induced by oxygen atoms interacts with the dislocations and therefore restricts the dislocation motion [43]. Furthermore, the small amounts of precipitated α plates in 0.4O (~2%) and 0.5O (~7%) alloys can also act as obstacles to block the dislocation motion, contributing to the increased hardness. This may also explain the slightly larger error bars of 0.4O and 0.5O alloys, compared to the others without the precipitated α phase in Fig. 4-7.

4.2.4.2 Tensile properties

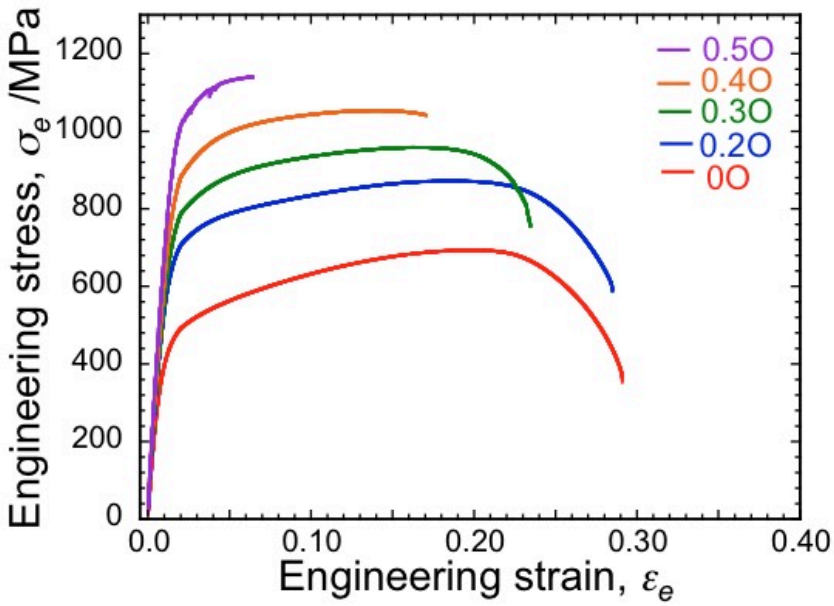

Fig. 4-8 Engineering stress-strain curves of the as-quenched Ti-7.5Mo alloys with different oxygen contents.

The engineering stress (σ_e)-strain (ε_e) curves of the prepared Ti-7.5Mo-xO (x = 0, 0.2, 0.3, 0.4 and 0.5 (wt.%)) alloys are plotted in Fig. 4-8. Sudden fracture can be identified in 0.4O and 0.5O alloys. Accordingly, the true stress (σ_t)-true strain (ε_t) curves and the calculated work-hardening rate ($\theta = \partial\sigma_t/\partial\varepsilon_t$) curves are plotted in Fig. 4-9. These alloys except for 0.5O show good ability of plastic deformation. Furthermore, the work-hardening rate curves of 0~0.4O alloys are very similar, which suggests the negligible effect of oxygen content (0~0.4 wt.%) on the plastic deformation of Ti-7.5Mo alloy. The tensile properties are summarized in Table 1. The 0.2% offset yield strength (YS) increases intensely from 386 MPa to 826 MPa with increasing the oxygen addition from 0 to 0.5 wt.%. The ultimate tensile strength (UTS) also shows an increasing tendency, however, the total elongation (tEL) and uniform elongation (uEL) decrease with the adding oxygen content. As indicated in Table 4-1, the Young's modulus (E) of 0O alloy shows the minimum value of 55.4 GPa. With increasing the oxygen addition, the E increases gradually to 73.9 GPa of 0.5O, which is still much lower than that of Ti-6Al-4V alloy (~110 GPa) [4].

Table 4-1
Tensile properties of 0.2% offset yield strength (YS), ultimate tensile strength (UTS), total elongation (tEL), uniform elongation (uEL) and Young's modulus (E) of the as-quenched Ti-7.5Mo alloys with different levels of oxygen.

Alloys	YS (MPa)	UTS (MPa)	tEL	uEL	E (GPa)
0O	386	694	0.29	0.18	55.4
0.2O	593	872	0.28	0.17	60.0
0.3O	643	958	0.24	0.15	61.3
0.4O	711	1054	0.17	0.13	67.3
0.5O	826	1140	0.06	-	73.9

The addition of oxygen atoms is suggested to be very effective to increase the strength (Table 4-1), which is also ascribed to the solid-solution strengthening effect. Fig. 4-10 shows the relationship between yield strength and Young's modulus (Fig. 4-10(a)), and also the relationship between total elongation and Young's modulus (Fig. 4-10(b) of Ti-7.5Mo-xO (x=0, 0.2, 0.3, 0.4 and 0.5 (wt.%)) alloys. The mechanical properties of some well-reported biomedical titanium alloys such as c.p. Ti [6], Ti-6Al-4V (annealed) [4], Ti-15Mo (annealed) [44] and Ti-13Zr-13Nb (aged) [45] are also shown for comparison. These alloys are classified into four groups based on their main phase constitutions, *i.e.,* α, α+β, β, and α" groups. Accordingly, the prepared Ti-7.5Mo-xO alloys belong to the α"-type. It can be seen that 0.2O and 0.3O alloys exhibit relatively lower Young's modulus (<65 GPa) than the other alloys, meanwhile, they also exhibit an outstanding combination of low Young's modulus and high yield strength, and lower Young's modulus and elongation. Furthermore, most of other alloys are multicomponent systems; the present alloys are designed based on simply binary alloys. This may be one advantage in terms of the materials cost and processing. Therefore, Ti-7.5Mo alloy with oxygen addition ≤ 0.3 wt.% is considered to have good potential for biomedical applications.

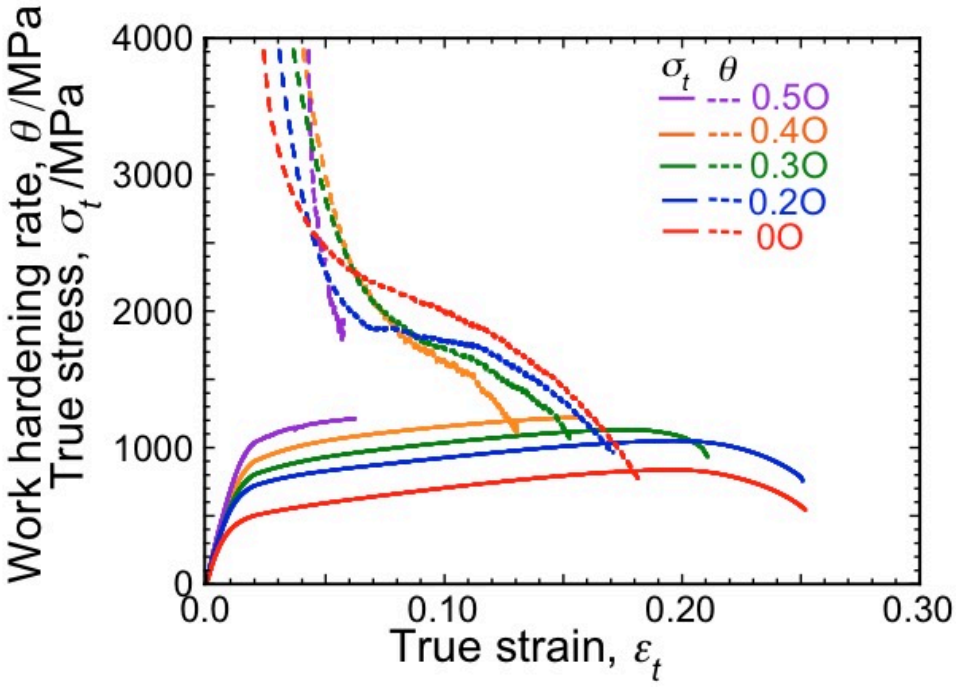

Fig. 4-9 True stress-strain and corresponding work-hardening rate curves of the as-quenched Ti-7.5Mo-xO (x = 0, 0.2, 0.3, 0.4 and 0.5 (wt.%)) alloys.

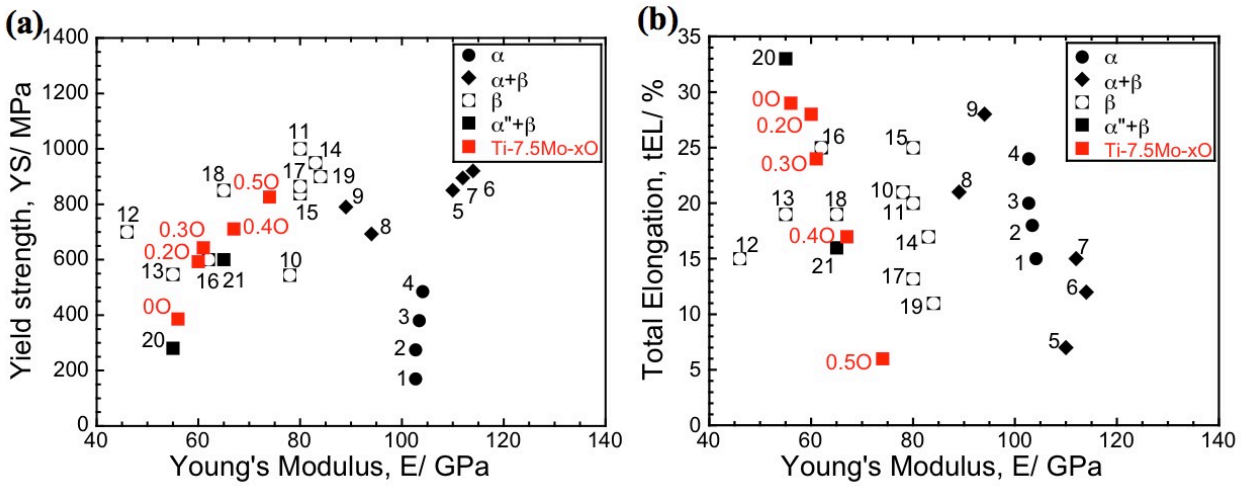

Fig. 4-10 Plots of yield strength vs. Young's modulus (a), and total elongation vs. Young's modulus (b) of Ti-7.5Mo-xO (x = 0, 0.2, 0.3, 0.4 and 0.5 (wt.%)) in the present study, as well as several typical titanium alloys for biomedical applications. α-type: #1-4 c.p. Ti grade 1-4 [6]; α+β-type: #5 Ti-6Al-4V (annealed) [4], #6 Ti-6Al-7Nb (wrought) [46], #7 Ti-5Al-2.5Fe (cast) [6]; β-type: #8 Ti-15Sn-4Nb-2Ta-0.2Pd (annealed) and #9 Ti-15Zr-4Nb-2Ta-0.2Pd (annealed) [47], #10 Ti-15Mo (annealed) [44], #11 Ti-12Mo-6Zr-2Fe (annealed) [48], #12 Ti-24Nb-4Zr-7.9Sn (hot-rolled) [10], #13 Ti-35Nb-7Zr-5Ta (annealed) [49], #14 Ti-15Mo-2.8Nb-0.2Si (annealed) and #15 Ti-15Mo-5Zr-3Al (solution-treated) [6], #16 Ti-29Nb-13Ta-4.6Zr (solution-treated) [50], #17 Ti-29Nb-13Ta-4.6Zr (aged) [3], #18 Ti-23Nb-0.7Ta-2Zr-1.2O (solution-treated) [51], #19 Ti-13Zr-13Nb (aged) [45]; α″+β-type: #20 Ti-23Nb-0.7Ta-2Zr (solution-treated) [18], and #21 Ti-29Nb-13Ta-4.6Cr (cold-rolled) [52].

4.2.4.3 Fracture surface morphology

The characterization of the fracture surface by SEM was performed on the as-quenched Ti-7.5Mo-xO (x = 0, 0.2, 0.3, 0.4 and 0.5 (wt.%)) alloys. The results are displayed in Fig. 4-11. The fracture surfaces of 0O (Fig. 4-11(a)), 0.2O (Fig. 4-11(b)) and 3O (Fig. 4-11(c)) alloys show equiaxed dimples, corresponding to a typical ductile fracture mode. The size of dimples of 0O alloy is similar to that of 0.2O alloy, and both larger than that of 0.3O alloy. This indicates the better ductility of 0O and 0.2O alloys, as shown in Table 4-1. The fracture surface of 0.4O (Fig. 4-11(d)) shows a mixture of dimples and intergranular facets, indicating the decrease of ductility. In 0.5O alloy, the fracture includes intergranular facets and fine dimples (Fig. 4-11(e)). The intergranular crack along the grain boundary is shown by the white arrow, contributing to the enhanced embrittlement. The intergranular fracture surfaces of 0.4O and 0.5O alloys might be related with the presence of α precipitates along prior β grain boundaries, as can be observed in SEM images (Fig. 4-3(g)-(j)). This can explain the premature fracture behavior and the dramatic decrease of elongation in 0.4O and 0.5O alloys (Fig. 4-8). The invesitigations of the fracture surfaces indicate that the tensile fracture mode of Ti-7.5Mo alloy transforms from ductile type to brittle intergranular type with increasing the oxygen content.

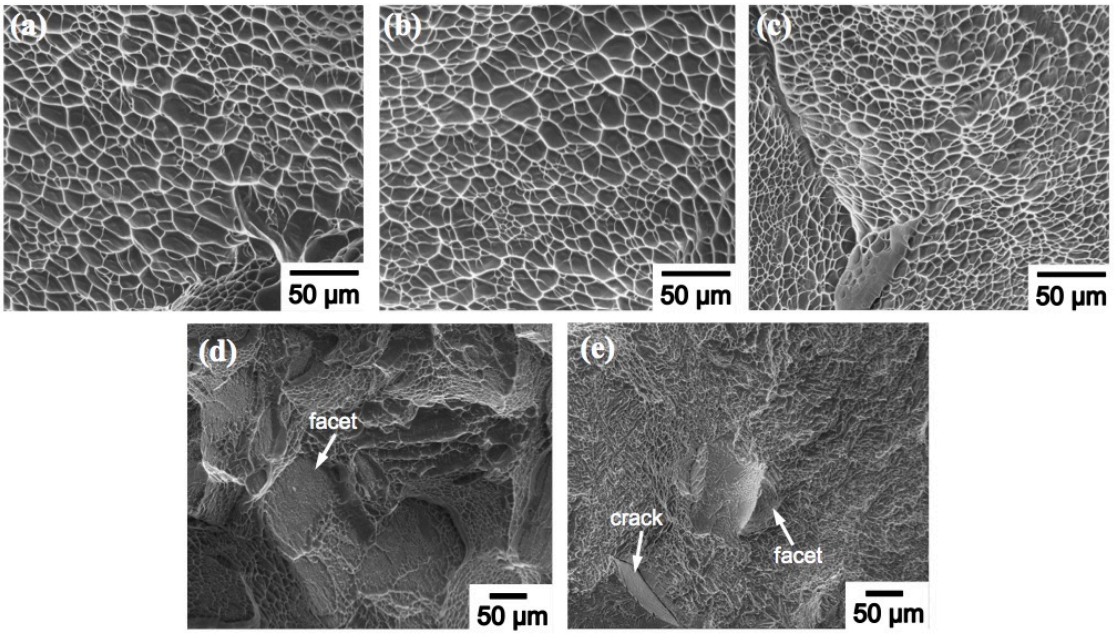

Fig. 4-11 SEM secondary electron images showing the fracture surfaces of (a) 0O, (b) 0.3O, (c) 0.4O, (d) 0.5O samples after the tensile test shown in Fig. 4-(8)

4.3 Conclusion

The effect of oxygen contents on the microstructures and mechanical properties of as-quenched Ti-7.5Mo (wt.%) alloy from 1173K has been investigated. The main results are summarized below:

(1) The as-quenched Ti-7.5Mo-xO (x = 0, 0.2, 0.3, 0.4 and 0.5 (wt.%)) alloys consist mainly of orthorhombic-α″ martensite. The high addition of oxygen (~0.5 wt.%) results in the increased β peak

intensity in X-ray diffraction profiles, suggesting the suppression of β→α″ martensitic transformation upon quenching. Additional α phase has been identified in 0.4O and 0.5O alloys, which is attributed to the α-stabilizing effect by the interstitial oxygen atoms.

(2) With increasing the oxygen content, the orthorhombicity ($b_{\alpha''}/a_{\alpha''}$ ratio) of orthorhombic-α″ phase decreases. The α″ plates in 0O and 0.5O alloys contain internal $\{111\}_{\alpha''}$-Type I twinning structure, which indicates that the oxygen addition (0~0.5 wt.%) has a negligible effect on the twinning system in α″ martensite of Ti-7.5Mo alloy.

(3) With increasing the oxygen content in Ti-7.5Mo alloy, the Vickers micro-hardness, yield strength, ultimate tensile strength, and Young's modulus increase, while the total elongation and uniform elongation decrease. This is due to the solid-solution strengthening by the interstitial oxygen atoms. The tensile fracture surfaces exhibit a transition from ductile dimple to brittle intergranular type, leading to a decrease in the ductility with increasing the oxygen content.

(4) In the present work, 0.2O and 0.3O alloys exhibit excellent combinations of high yield strength and elongation, as well as low Young's modulus values. The addition of oxygen (≤ 0.3 wt.%) is regarded as an effective method to improve the balance of tensile properties of Ti-7.5Mo alloy. Compared to other multicomponent alloys, the present alloys may be more cost effective and potential candidate materials for biomedical applications.

References

[1] M. Long, H.J. Rack, Titanium alloys in total joint replacement-a materials science perspective., Biomaterials. 19 (1998) 1621–1639.

[2] M. Geetha, A.K. Singh, R. Asokamani, A.K. Gogia, Ti based biomaterials, the ultimate choice for orthopaedic implants - A review, Prog. Mater. Sci. 54 (2009) 397–425.

[3] D. Kuroda, M. Niinomi, M. Morinaga, Y. Kato, T. Yashiro, Design and mechanical properties of new β type titanium alloys for implant materials, Mater. Sci. Eng. A. 243 (1998) 244–249.

[4] R.M. Pilliar, Modern metal processing for improved load-bearing surgical implants, Biomaterials. 12 (1991) 95–100.

[5] C.N. Elias, J.H.C. Lima, R. Valiev, M. a Meyers, Biomedical Applications of Titanium and its Alloys, J. Miner. Met. Mater. Soc. (2008) 46–49.

[6] M. Niinomi, Mechanical properties of biomedical titanium alloys, Mater. Sci. Eng. A. 243 (1998) 231–236.

[7] W.F. Ho, C.P. Ju, J.H. Chern Lin, Structure and properties of cast binary Ti–Mo alloys, Biomaterials. 20 (1999) 2115–2122.

[8] W.F. Ho, A comparison of tensile properties and corrosion behavior of cast Ti-7.5Mo with c.p. Ti, Ti-15Mo and Ti-6Al-4V alloys, J. Alloys Compd. 464 (2008) 580–583.

[9] L. Zardiackas, D. Mitchell, J. Disegi, Characterization of Ti-15Mo Beta Titanium Alloy for Orthopaedic Implant Applications, in: Med. Appl. Titan. Its Alloy. Mater. Biol. Issues, ASTM International, 100 Barr Harbor Drive, PO Box C700, West Conshohocken, PA 19428-2959, 1996: pp. 60–75.

[10] Y.L. Hao, S.J. Li, S.Y. Sun, C.Y. Zheng, R. Yang, Elastic deformation behaviour of Ti-24Nb-4Zr-7.9Sn for biomedical applications, Acta Biomater. 3 (2007) 277–286.

[11] C.C. Chung, S.W. Wang, Y.C. Chen, C.P. Ju, J.H. Chern Lin, Effect of cold rolling on structure and tensile properties of cast Ti-7.5Mo alloy, Mater. Sci. Eng. A. 631 (2015) 52–66.

[12] D.J. Lin, C.C. Chuang, J.H. Chern Lin, J.W. Lee, C.P. Ju, H.S. Yin, Bone formation at the surface of low modulus Ti–7.5Mo implants in rabbit femur, Biomaterials. 28 (2007) 2582–2589.

[13] H.Y. Kim, Y. Ikehara, J.I. Kim, H. Hosoda, S. Miyazaki, Martensitic transformation, shape memory effect and superelasticity of Ti–Nb binary alloys, Acta Mater. 54 (2006) 2419–2429.

[14] H. Conrad, Effect of interstitial solutes on the strength and ductility of titanium, Prog. Mater. Sci. 26 (1981) 123–403.
[15] E.W. Collins, J.C. Ho, H.L. Gegel, Solid Solution Strengthening and Fundamental Design of Titanium Alloys, 1972.
[16] A. Ramarolahy, P. Castany, F. Prima, P. Laheurte, I. Péron, T. Gloriant, Microstructure and mechanical behavior of superelastic Ti-24Nb-0.5O and Ti-24Nb-0.5N biomedical alloys, J. Mech. Behav. Biomed. Mater. 9 (2012) 83–90.
[17] H. Duan, H. Xu, W. Su, Y. Ke, Z. Liu, H. Song, Effect of oxygen on the microstructure and mechanical properties of Ti-23Nb-0.7Ta-2Zr alloy, Int. J. Miner. Metall. Mater. 19 (2012) 1128–1133.
[18] M. Besse, P. Castany, T. Gloriant, Mechanisms of deformation in gum metal TNTZ-O and TNTZ titanium alloys: A comparative study on the oxygen influence, Acta Mater. 59 (2011) 5982–5988.
[19] I.I. Kornilov, Effect of oxygen on titanium and its alloys, Met. Sci. Heat Treat. 15 (1974) 826–829.
[20] M. Nakai, M. Niinomi, T. Akahori, H. Tsutsumi, M. Ogawa, Effect of Oxygen Content on Microstructure and Mechanical Properties of Biomedical Ti-29Nb-13Ta-4.6Zr Alloy under Solutionized and Aged Conditions, Mater. Trans. 50 (2009) 2716–2720.
[21] J. Il Kim, H.Y. Kim, H. Hosoda, S. Miyazaki, Shape Memory Behavior of Ti–22Nb–(0.5–2.0)O (at%) Biomedical Alloys, Mater. Trans. 46 (2005) 852–857.
[22] H.Y. Kim, S. Miyazaki, Martensitic Transformation and Superelastic Properties of Ti-Nb Base Alloys, Mater. Trans. 56 (2015) 625–634.
[23] M. Tahara, H.Y. Kim, T. Inamura, H. Hosoda, S. Miyazaki, Lattice modulation and superelasticity in oxygen-added β-Ti alloys, Acta Mater. 59 (2011) 6208–6218.
[24] G. Ghosh, G.B. Olson, Kinetics of F.C.C. → B.C.C. heterogeneous martensitic nucleation-I. The critical driving force for athermal nucleation, Acta Metall. Mater. 42 (1994) 3361‑3370.
[25] J.-Y. Yan, G.B. Olson, Computational Thermodynamics and Kinetics of Displacive Transformations in Titanium-Based Alloys, J. Alloys Compd. 673 (2016) 441–454.
[26] M. Yan, W. Xu, M.S. Dargusch, H.P. Tang, M. Brandt, M. Qian, Review of effect of oxygen on room temperature ductility of titanium and titanium alloys, Powder Metall. 57 (2014) 251–257.
[27] Y.W. Chai, H.Y. Kim, H. Hosoda, S. Miyazaki, Interfacial defects in Ti-Nb shape memory alloys, Acta Mater. 56 (2008) 3088–3097.
[28] Y. Takemoto, I. Shimizu, A. Sakakibara, M. Hida, Y. Mantani, Tensile Behavior and Cold Workability of Ti-Mo Alloys, Mater. Trans. 45 (2004) 1571–1576.
[29] Y. Mantani, Y. Takemoto, M. Hida, A. Sakakibara, M. Tajima, Phase Transformation of Martensite Structure by Aging in Ti-8 mass % Mo Alloy, Mater. Trans. 45 (2004) 1629–1634.
[30] C.H. Wang, C.D. Yang, M. Liu, X. Li, P.F. Hu, A.M. Russell, G.H. Cao, Martensitic microstructures and mechanical properties of as-quenched metastable β-type Ti–Mo alloys, J. Mater. Sci. 51 (2016) 6886–6896.
[31] K.A. Bywater, J.W. Christian, Martensitic transformations in titanium-tantalum alloys, Philos. Mag. 25 (1972) 1249–1273. doi:10.1080/14786437208223852.
[32] A.G. Crocker, Twinned martensite, Acta Metall. 10 (1962) 113–122.
[33] T. Inamura, J.I. Kim, H.Y. Kim, H. Hosoda, K. Wakashima, S. Miyazaki, Composition dependent crystallography of α''-martensite in Ti‑Nb-based β-titanium alloy, Philos. Mag. 87 (2007) 3325‑3350.
[34] Y. Liang, H. Kato, M. Taya, T. Mori, Infinitesimal approach to the crystallography of martensitic transformation: application to Ni-Ti, Scr. Mater. 43 (2000) 535–540.
[35] B. Predel, Mo-Ti, in: O. Madelung (Ed.), Landolt-Börnstein - Gr. IV Phys. Chem., Springer Berlin Heidelberg, Berlin/Heidelberg, 1997: pp. 1–3.
[36] M. Tahara, T. Inamura, H.Y. Kim, S. Miyazaki, H. Hosoda, Role of oxygen atoms in α'' martensite of Ti-20at.% Nb alloy, Scr. Mater. 112 (2016) 15‑18.
[37] X.H. Min, P.F. Bai, S. Emura, X. Ji, C. Cheng, B. Jiang, K. Tsuchiya, Effect of oxygen content on deformation mode and corrosion behavior in β-type Ti-Mo alloy, Mater. Sci. Eng. A. 684 (2017) 534–541.
[38] M. Bönisch, M. Calin, T. Waitz, A. Panigrahi, M. Zehetbauer, A. Gebert, W. Skrotzki, J. Eckert, Thermal stability and phase transformations of martensitic Ti–Nb alloys, Sci. Technol. Adv. Mater. 14 (2013) 55004.
[39] A.I. Kahveci, G.E. Welsch, Effect of oxygen on the hardness and alpha/beta phase ratio of Ti6A14V alloy, Scr. Metall. 20 (1986) 1287–1290.

[40] F. Geng, M. Niinomi, M. Nakai, Observation of yielding and strain hardening in a titanium alloy having high oxygen content, Mater. Sci. Eng. A. 528 (2011) 5435–5445.
[41] Z. Liu, G. Welsch, The effects of oxygen and heat treatment on microstructures and mechanical properties of alpha and beta titanium alloys, Metall. Trans. A. 19A (1988) 527–542.
[42] J.L. Murray, Phase Diagrams of Binary Titanium Alloys, Metals Park, Ohio: ASM International, 1987.
[43] F.J. Gil, C. Aparicio, J.A. Planell, Effect of Oxygen Content on Grain Growth Kinetics of Titanium, J. Mater. 10 (2003) 10–13.
[44] K. Wang, The use of titanium for medical applications in the USA, Mater. Sci. Eng. A. 213 (1996) 134–137.
[45] A.K. Mishra, J.A. Davison, P. Kovacs, R.A. Poggie, Ti-13 Nb-13Zr: A new low modulus, high strength, corrosion resistant near-beta alloy for orthopaedic implants, in: Beta Titan. Alloy. 1990's, TMS of AIME, 1993: pp. 61–72.
[46] M. SEMLITSCH, H. WEBER, R. STREICHER, R. SCHON, Joint replacement components made of hot-forged and surface-treated Ti-6Al-7Nb alloy, Biomaterials. 13 (1992) 781–788.
[47] Y. Okazaki, Y. Ito, A. Ito, T. Tateishi, Effect of Alloying Elements on Mechanical Properties of Titanium Alloys for Medical Implants, Mater. Trans. JIM. 34 (1993) 1217–1222.
[48] K.K. Wang, L.J. Gustavson, J.H. Dumbleton, The characterization of Ti- 12Mo-6Zr-2Fe-A new alloy developed for surgical implants, in: Beta Titan. Alloy. 1990's, TMS of AIME, 1993: pp. 49–60.
[49] P.L. Ferrandini, F.F. Cardoso, S.A. Souza, C.R. Afonso, R. Caram, Aging response of the Ti-35Nb-7Zr-5Ta and Ti-35Nb-7Ta alloys, J. Alloys Compd. 433 (2007) 207–210.
[50] M. Niinomi, Fatigue performance and cyto-toxicity of low rigidity titanium alloy, Ti-29Nb-13Ta-4.6Zr, Biomaterials. 24 (2003) 2673–2683.
[51] T. Saito, T. Furuta, J.-H. Hwang, S. Kuramoto, K. Nishino, N. Suzuki, R. Chen, A. Yamada, K. Ito, Y. Seno, T. Nonaka, H. Ikehata, N. Nagasako, C. Iwamoto, Y. Ikuhara, T. Sakuma, Multifunctional Alloys Obtained via a Dislocation-Free Plastic Deformation Mechanism, Science (80-.). 300 (2003) 464–467.
[52] Q. Li, M. Niinomi, J. Hieda, M. Nakai, K. Cho, Deformation-induced ω phase in modified Ti-29Nb-13Ta-4.6Zr alloy by Cr addition, Acta Biomater. 9 (2013) 8027–8035.

Chapter 5 Strain-rate effect and work-hardening behavior in β-type Ti-10Mo-1Fe alloy with TWIP effect

5.1 Introduction

β-Ti alloys have attracted a lot of attentions for applications in aerospace, biomedical and energy industries due to their superior properties such as high specific strength, good corrosion resistance, low elastic modulus and excellent biocompatibility [1-3]. One characteristic of β-Ti alloys has been reported that the dominant deformation mode varies from dislocation slip to $\{332\}<113>_\beta$ twinning and/or stress-induced α″ martensitic transformation with decreasing the β phase stability [4]. As a unique twin mode in bcc metals and alloys, $\{332\}<113>_\beta$ twinning has been always observed in Ti-Mo [5,6], Ti-Nb [7], Ti-V [8] and Ti-Cr [9,10] alloys. Several studies have shown that the $\{332\}<113>_\beta$ twinning in β-Ti alloys leads to a outstanding work-hardening rate and improved ductility, similar to the twinning-induced plasticity (TWIP) in steels [11-13]. The mechanism of the outstanding work-hardening induced by the twinning can be well-explained by a dynamic Hall-Petch effect [14]. The twin boundaries are suggested to act as strong barriers for the dislocation glide, and the increasing number of twin boundaries leads to a reduction of a mean free path of dislocation motion, contributing to the enhanced flow stress and work hardening rate. Min *et al.* [12] reported that the dynamic Hall-Petch effect by $\{332\}<113>_\beta$ twinning also takes place in the metastable β alloy of Ti-15Mo (wt.%). Thus the understanding of TWIP with the $\{332\}<113>_\beta$ twinning is of great importance for improving the strength-ductility balance in β-Ti alloys.

Some reports have revealed that the mechanical properties and deformation mechanisms of β-Ti alloys have a strong dependence on the strain rate [15-18]. Farghadany *et al*. [17] reported a suppression of stress-induced α″ martensitic transformation during the high strain rate deformation, resulting in the negative strain rate sensitivity in Ti-29Nb-13Ta-4.6Zr (wt.%) alloy, *i.e.*, a higher flow stress at a lower strain rate. Chiou *et al.* [18] found an increasing flow stress by increasing the strain rate in Ti-15Mo-5Zr-3Al (wt.%) alloy with a higher β phase stability, in which the deformation mode is only dislocation slip. Some TWIP steels exhibit negative strain rate sensitivity of flow stress [19-22]. There are two mechanisms that has been proposed to explain this: (1) dynamic strain aging (DSA), in which the dislocation motion is restricted by the solute atoms (*e.g.*, interstitial carbon) during the plastic deformation [19,20]; (2) suppresed twin formation at an enhanced strain rate deformation in DSA-free TWIP steels [21,22]. Meanwhile, there is a lack of knowledge related with the mechanism of strain rate dependence of work-hardening performance in β-Ti alloys, in particular, with the occurance of $\{332\}<113>_\beta$ twinning. Furthermore, it has been suggested that two factors contribute to the strain rate sensitivity (m): one is the instantaneous strain rate sensitivity (m_i), dealing with the strain rate effect on the existing microstructure, and the other is the strain rate sensitivity of work-hardening (m_θ), associated with the deformation microstructure evolution [23]. The existing knowledge on the strain rate dependence of β-Ti alloys is mostly related to the overall *m* [24-29]. More fundamental understandings on the contribution of m_i and m_θ to the overall m are therefore required for β-Ti alloys.

The purpose of the present study is to investigate the effect of strain rate on the work-hardening behavior in a metastable β-Ti alloy showing TWIP effect. We focused on a Ti-10Mo-1Fe (wt.%) alloy, which has been reported to deform mainly by {332}<113>$_\beta$ twinning [13]. The work-hardening behavior was studied by monotonic tensile tests at various strain rates ranging from 2.8x10^{-5} s^{-1} to 2.8x10^{-1} s^{-1}. In order to study the change of instantaneous strain rate sensitivity during plastic deformation, strain rate jump tests were also performed by instantaneously changing the strain rate from 2.8x10^{-5} s^{-1} to 2.8x10^{-3} s^{-1} at different strain levels (2.0%, 7.7%, 12.2%, 19.9%). Microstructure evolution was invesitigated by EBSD and XRD focusing on {332}<113>$_\beta$ twinning and dislocations. The correlation between the work-hardening behavior and microstructure evolution was discussed.

5.2 Experimental results

5.2.1 Tensile properties and work-hardening behavior

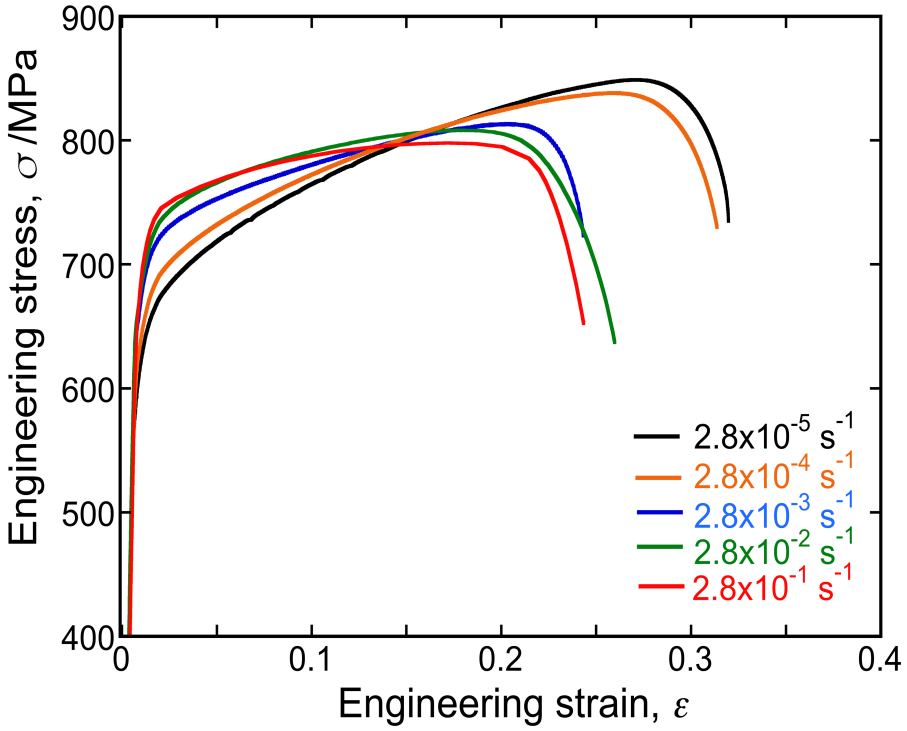

Fig. 5-1 Engineering stress-strain curves at various strain rates.

The engineering stress (σ)-strain (ε) curves obtained at constant strain rates (2.8x10^{-5}~2.8x10^{-1} s^{-1}) are displayed in Fig. 5-1. Three samples were deformed for each strain rate and the obtained tensile properties were found to be reproducible and reliable. The average values and standard deviations of tensile properties are listed in Table 5-1. The yield strength (YS, 0.2% proof stress) is observed to be increased with increasing the strain rate (612 MPa at 2.8x10^{-5} s^{-1} and 675 MPa at 2.8x10^{-1} s^{-1}). However, when the strain rate is increased from 2.8x10^{-5} s^{-1} to 2.8x10^{-1} s^{-1}, the ultimate tensile strength (UTS) decreases from 841 MPa to 799 MPa and the total elongation (tEL) decreases from 0.34 to 0.24. Furthermore, uniform elongation (uEL), also listed in Table 5-1, decreases from 0.25 at the strain rate of 2.8x10^{-5} s^{-1} to 0.15 at 2.8x10^{-1} s^{-1}. It shows that the lower strain rate leads to enhanced ductility.

Table 5-1 Tensile properties of 0.2% proof stress (YS), ultimate tensile strength (UTS), total elongation (tEL) and uniform elongation (uEL) at different strain rates deformation.

Strain rate	YS (MPa)	UTS (MPa)	tEL	uEL
$2.8x10^{-5}$	612 ± 6	841 ± 6	0.34 ± 0.01	0.25 ± 0.01
$2.8x10^{-4}$	626 ± 4	833 ± 6	0.32 ± 0.01	0.24 ± 0.02
$2.8x10^{-3}$	662 ± 7	822 ± 7	0.28 ± 0.02	0.21 ± 0.02
$2.8x10^{-2}$	673 ± 3	816 ± 6	0.26 ± 0.01	0.17 ± 0.01
$2.8x10^{-1}$	675 ± 3	799 ± 8	0.24 ± 0.03	0.15 ± 0.02

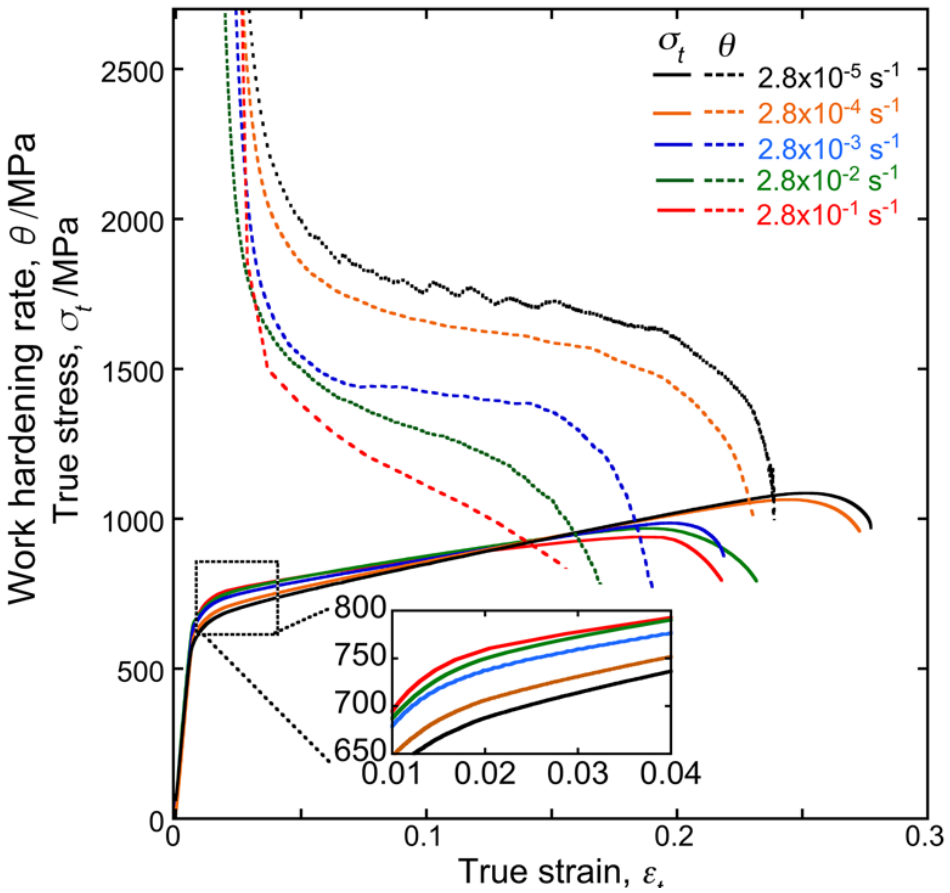

Fig. 5-2 True stress-strain curves and corresponding work-hardening rate curves at various strain rates.

The true stress (σ_t)-true strain (ε_t) curves and the calculated work-hardening rate ($\theta = \partial\sigma_t/\partial\varepsilon_t$) curves at different strain rates are shown in Fig. 5-2. The inset exhibites a magnified inage of the area in the dashed box. It can be observed that the increasing strain rates result in a higher flow stress at a lower strain level, while for the strain over 0.13, the higher strain rate contributes to a lower flow stress. The θ-ε_t curves in Fig. 5-2 first exhibite a sharp drop up to $\varepsilon_t \sim 0.02$, which refers to the ordinary transition from the elastic to plastic regimes, and then gradually decrease to the point of plastic instability described by the Considere criteria ($\sigma_t = \theta$) [30]. It is clearly seen that the overall work-hardening rate decreases with increasing strain rate.

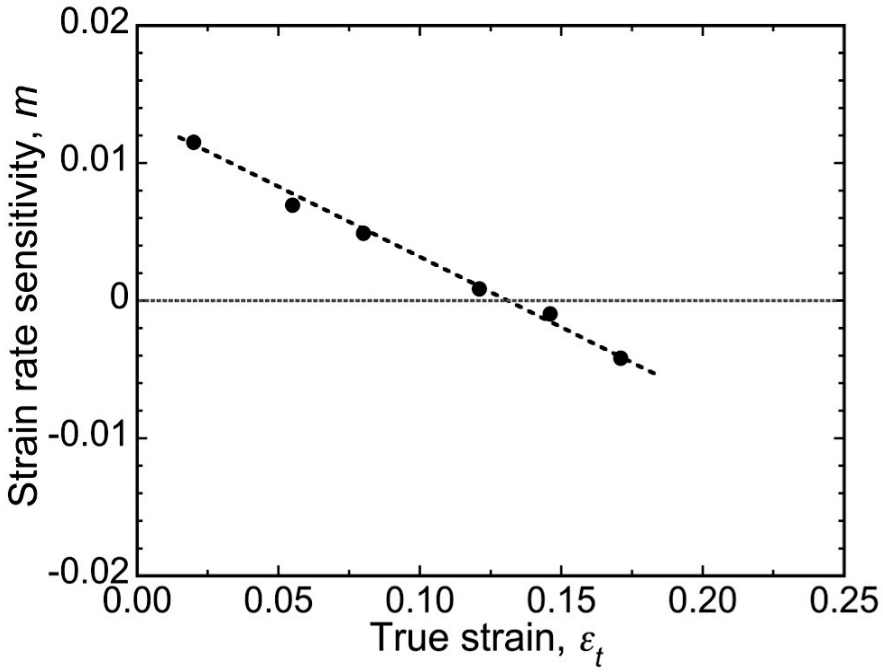

Fig. 5-3 The estimated strain rate sensitivity parameter (*m*) from Eq. (5-1) plotted with respect to true strain (ε_t).

From the results shown in Fig. 5-2, the strain rate sensitivity of flow stress, *m*, can be estimated based on the following equation:

$$m = \frac{\partial ln\sigma_t}{\partial ln\dot{\varepsilon}} \qquad (5-1)$$

where σ_t is the flow stress and $\dot{\varepsilon}$ is the strain rate. The dependence of the strain rate sensitivity *m* on the true strain is plotted in Fig. 5-3. The *m* linearly decreases with increasing true strain levels; in particular, *m* is positive at a true strain lower than 0.13, and becomes negative at strain over 0.13.Meanwhile, from the work-hardening rate curves, the strain rate sensitivity of work-hardening (m_θ) was calculated by

$$m_\theta = \frac{\partial ln\theta}{\partial ln\dot{\varepsilon}} \qquad (5-2)$$

The results are shown in Fig. 5-4. It shows that the m_θ is always negative and decreases linearly with strain.

The true stress-strain curves obtained from the strain rate jump tests from $2.8\text{x}10^{-5}$ s^{-1} to $2.8\text{x}10^{-3}$ s^{-1} are plotted in Fig. 5-5. The inset of Fig. 5-5 schematically illustrates the instantaneous response of the stress-strain curve at the vicinity of the jump. The sudden increase in the strain rate (from $\dot{\varepsilon}_1$ to $\dot{\varepsilon}_2$) leads to a sudden increase in the stress (from σ_1 to σ_i), followed by a gradually decrease until reaching a steady-state value (σ_2), which is still higher than the flow stress σ_1 prior to the jump. The results of instantaneous strain rate sensitivity with strain are

$$m_i = \frac{\ln(\sigma_2 - \sigma_1)}{\ln(\dot{\varepsilon}_2 - \dot{\varepsilon}_1)} \qquad (5-3)$$

where σ_1 is the flow stress before the strain rate jump and at the strain rate $\dot{\varepsilon}_1$ ($2.8\text{x}10^{-5}$ s^{-1}), and σ_2 is the extrapolated steady-state stress level after the strain rate jump to $\dot{\varepsilon}_2$ ($2.8\text{x}10^{-3}$ s^{-1}), as indicated in the inset of Fig. 5-5. The dependence of m_i on the true strain is plotted in Fig. 5-6. The m_i exhibits positive values and seems less sensitive to the true strain.

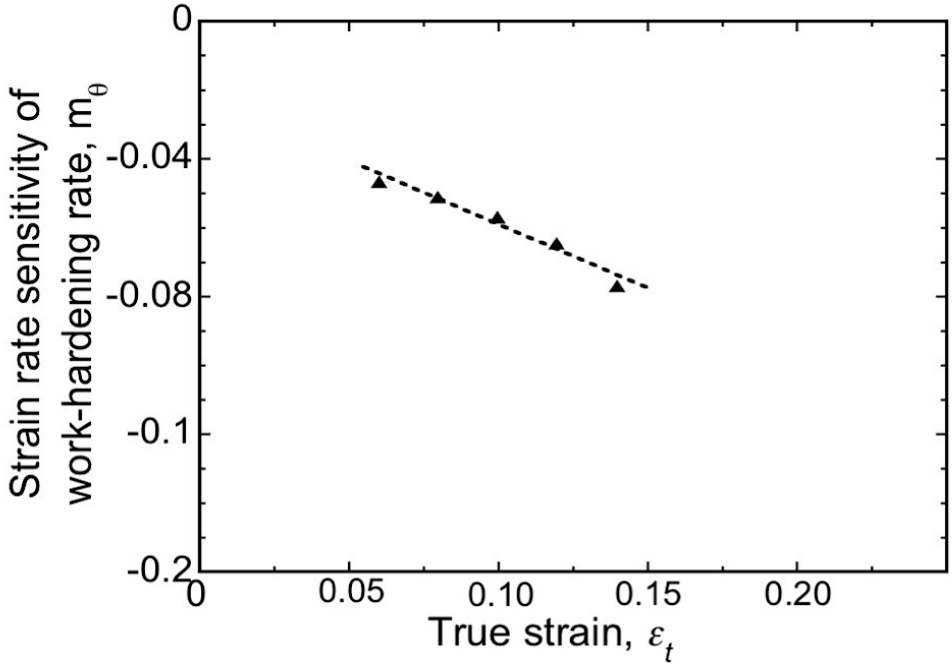

Fig. 5-4 The calculated strain rate sensitivity of work-hardening rate parameter (m_θ) plotted with respect to true strain (ε_t).

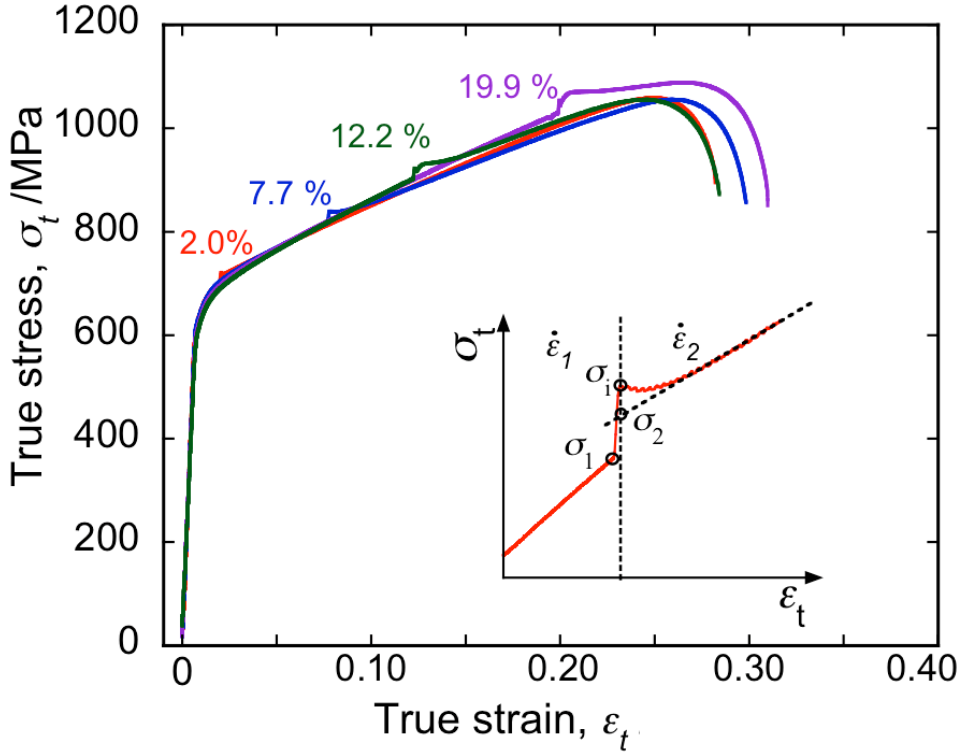

Fig. 5-5 True stress-strain curves of strain rate jump test from =$2.8\text{x}10^{-5}$ s^{-1} to = $2.8\text{x}10^{-3}$ s^{-1} performed at 2.0%, 7.7%, 12.2%, 19.9%. The inset shows a schematic illustration of the curve at a strain rate jump point

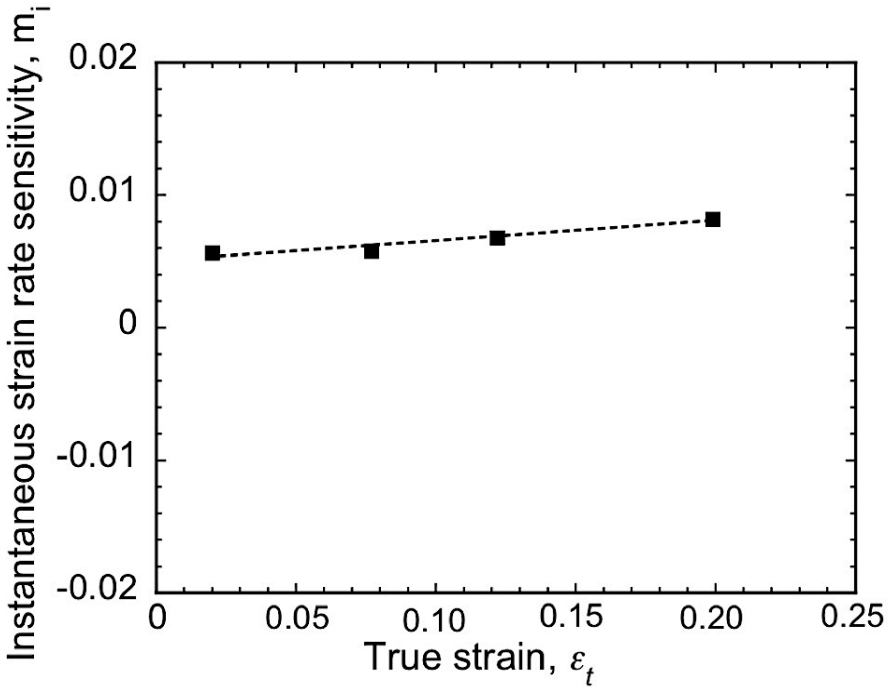

Fig. 5-6 True stress-strain curves of strain rate jump test from =2.8x10^{-5} s^{-1} to = 2.8x10^{-3} s^{-1} performed at 2.0%, 7.7%, 12.2%, 19.9%. The inset shows a schematic illustration of the curve at a strain rate jump point

5.2.2 Microstructure characterization

5.2.2.1 Initial microstructure

Fig. 5-7(a) shows EBSD inverse pole figure (IPF) map of the initial microstructure after solution-treatment and followed by water quenching. It exhibits a typical equiaxed microstructure with fully retained bcc-β phase. The average grain size is ~160 μm. As shown in Fig. 5-7(b), the texture in the initial microstructure is weak and thus the texture effect on the following deformation can be negligible.

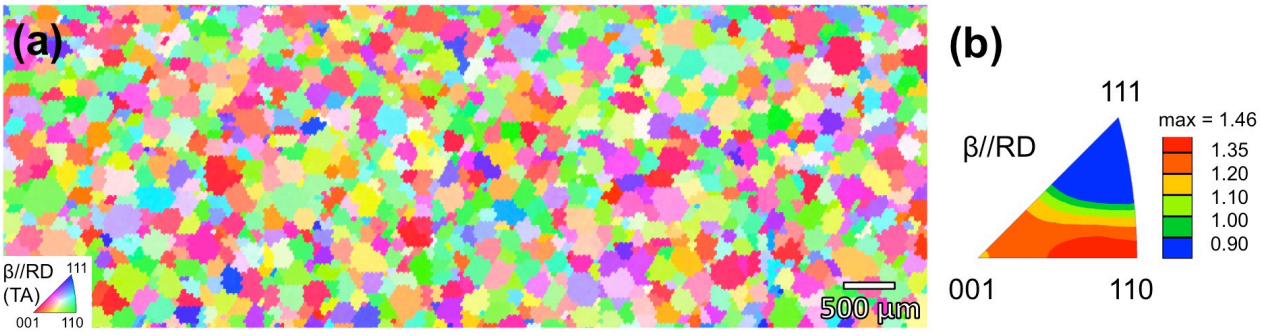

Fig. 5-7 (a) EBSD-IPF map of initial microstructure along RD (TA//RD, step size: 50 μm). (b) Invers pole figure.

5.2.2.2 Deformation microstructure

Fig. 5-8(a) shows EBSD-IPF map of the deformation microstructure with εt = 0.05 at strain rate of 2.8x10-1 s-1. The TA is parallel to the horizontal line. Band-like structures can be observed within the β-grains, which were induced by tensile deformation. They were p identified as {332}<113>$_\beta$

twinning in β phase with a boundary misorientation of 50.4° along the <110> direction [31], as indicated with the black lines in Fig. 5-8(b). Some of the grains in Fig. 5-8(a) contain single twin variant, as shown by an example of the grain marked with G-1. While some contain 2 (G-2) or more twin variants. The EBSD-IPF image of Fig. 5-8(b) shows the configuration of intersPection between two twin variants (T-A and T-B) taken from the grain of G-2. The crystallographic orientation of G-2 is $[\mathbf{21\bar{3}}]$//TA. Based on the trace analyze, the twinning systems of T-A and T-B is determined as $(\bar{\mathbf{3}}\mathbf{23})[\bar{\mathbf{1}}\mathbf{31}]$ and $(\mathbf{2}\bar{\mathbf{3}}\mathbf{3})[\bar{\mathbf{3}}\bar{\mathbf{1}}\mathbf{1}]$, which correspond to the largest Schmid factors of 0.48 and 0.37, respectively. It indicates that the activation of $\{332\}\langle 113\rangle_\beta$ twinning in G-2 obeys the Schmid law. Furthermore, the secondary twins can be observed within the primary twin of T-A, as shown in Fig. 5-8(b). Fig. 5-9 shows the ECCI images of the activated $\{332\}\langle 113\rangle_\beta$ twin. Masses of dislocations are observed in the intersection region of two twin bands, as indicated in Fig. 5-9.

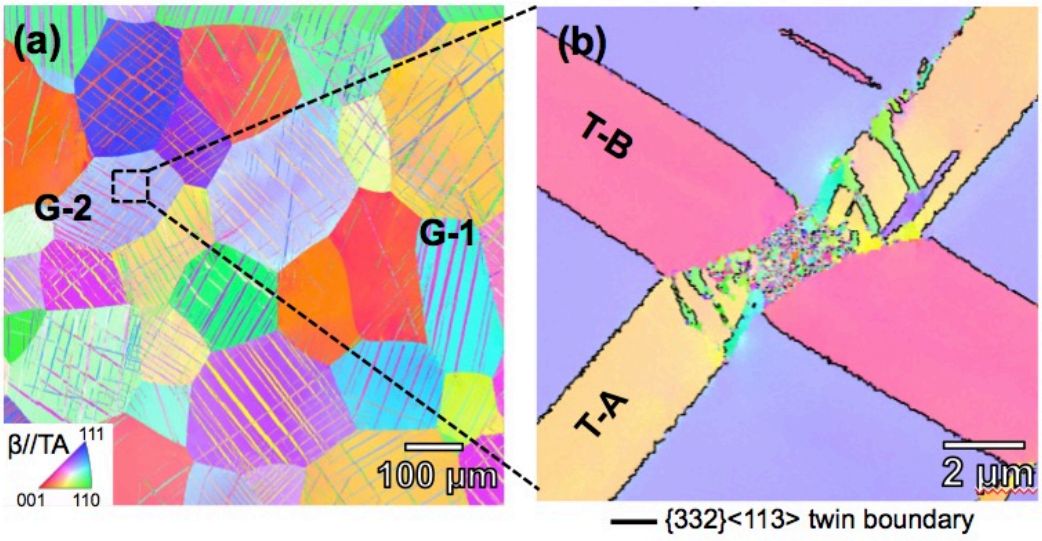

Fig. 5-8 (a) EBSD-IPF image of Ti-10Mo-1Fe alloy with strain of 0.05. The TA is parallel to the horizontal line. (b) IPF image taken from the region marked in (a). The {332}<113> twin boundary is indicated in black lines.

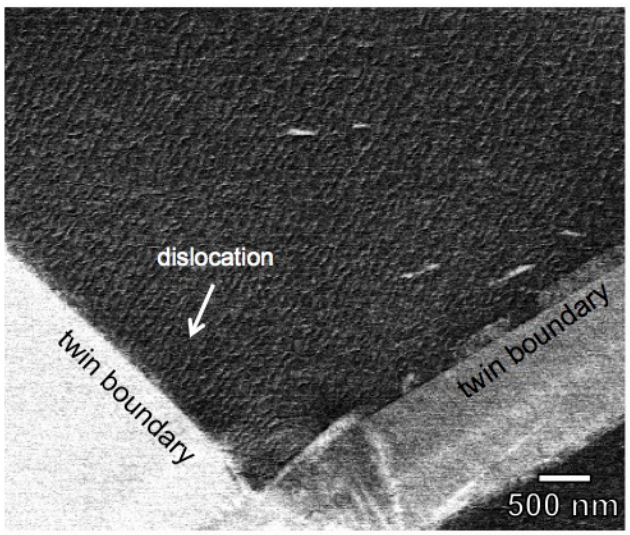

Fig. 5-9 ECCI image of the intersection region between two {332}<113> twins.

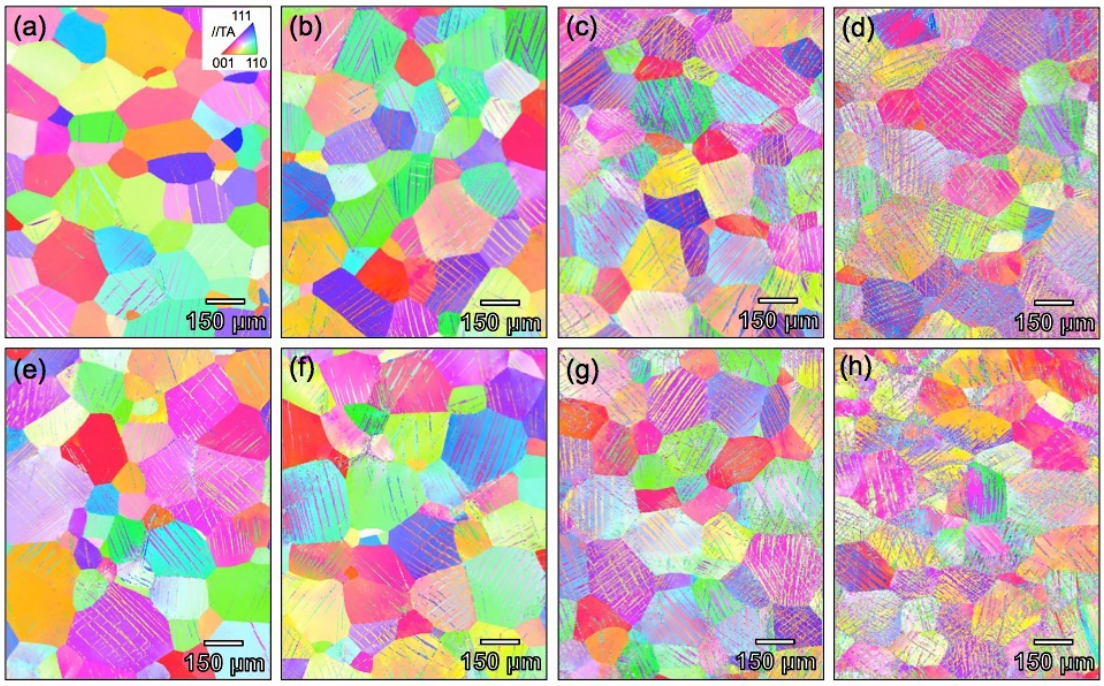

Fig. 5-10 EBSD-IPF maps for tensile axis (TA) direction of specimens deformed at lower strain rate of $2.5x10^{-5}$ s^{-1} with strain of (a) 0.025, (b) 0.05, (c) 0.1, and (d) 0.14; at higher strain rate of $2.5x10^{-1}$ s^{-1} (e) 0.025, (f) 0.05, (g) 0.1 and (h) 0.14. The horizontal direction is parallel to TA.

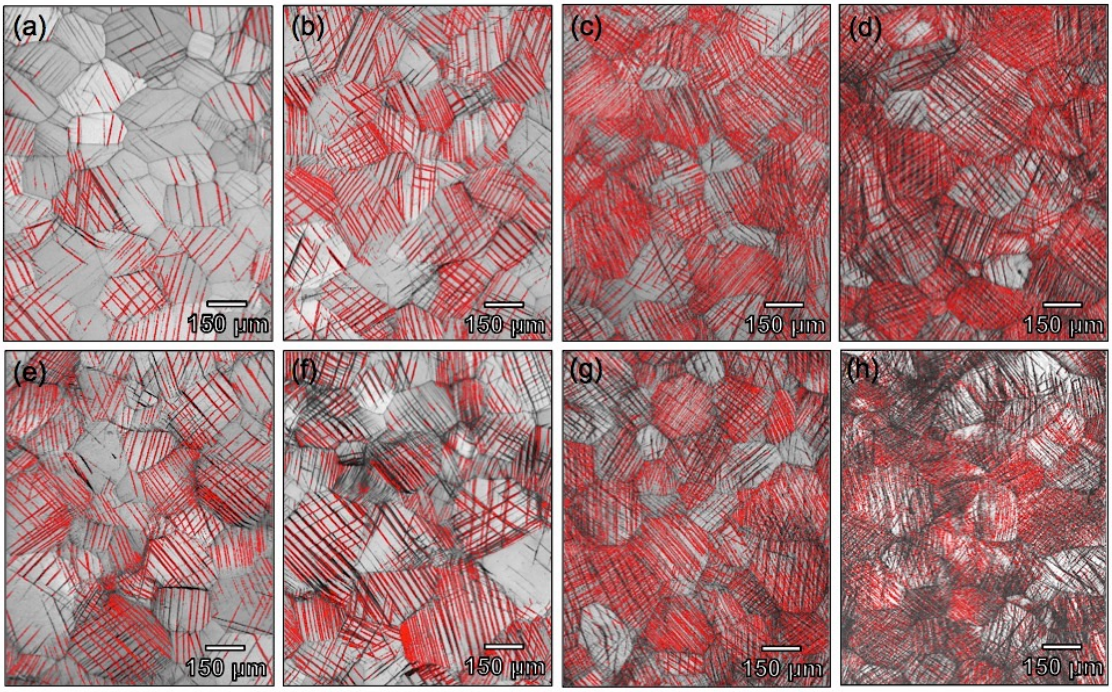

Fig. 5-11 Corresponding EBSD-IQ maps of specimens deformed at lower strain rate of $2.5x10^{-5}$ s^{-1} with strain of (a) 0.025, (b) 0.05, (c) 0.1, and (d) 0.14; at higher strain rate of $2.5x10^{-1}$ s^{-1} (e) 0.025, (f) 0.05, (g) 0.1 and (h) 0.14. The red line indicates {332}<113> twin boundary.

5.2.2.3 Evolution of {332}<113>$_\beta$ twin

In order to compare the evolution of {332}<113>$_\beta$ twinning in Ti-10Mo-1Fe alloy at different strain rates, EBSD scanning was carried out on the mirror-polished specimens stretched to different true strain levels (0.025, 0.05, 0.10 and 0.14) at constant strain rates of $2.8x10^{-5}$ s^{-1} and $2.8x10^{-1}$ s^{-1}. In order to obtain

the value of area fraction of {332}<113>$_\beta$ twinning, three areas of 1 × 2 mm^2 in the center of each specimen were calculated. The total area for each condition contains more than 200 grains, which makes the quantified results more reliable. Based on the EBSD-boundary maps, the twin area fractions were calculated with image processing softwares (Adobe Photoshop and NIH Image J).

Fig. 5-10 displays the EBSD-IPFs of deformation microstructures taken from the specimens strained up to (a) 0.025, (b) 0.05, (c) 0.10 and (d) 0.14 at the strain rate of 2.8x10^{-5} s^{-1}, and (e) 0.025, (f) 0.05, (g) 0.10 and (h) 0.14 at the strain rate of 2.8x10^{-1} s^{-1}. The corresponding IQ maps are displayed in Fig. 5-11. The plate-like features in the grain interiors (Fig. 5-10) are identified as {332}<113>$_\beta$ twins with a boundary misorientation of 50.4° along the <110>$_\beta$ direction [31]. Accordingly, the twin boundaries are indicated by the red lines in Fig. 5-11. Hence the EBSD results verify the {332}<113>$_\beta$ twinning as the dominant deformation mechanism in the present Ti-10Mo-1Fe alloy. The quantified area fraction of twins (f_{twin}) is plotted in Fig. 5-12 with the true strain, and the error bar represents the standard deviation. Deformation at different strain rates leads to a small but significant difference in f_{twin}. At ε_t of 0.025, a higher f_{twin} is obtained at the higher $\dot{\varepsilon}$ (15.6% at 2.8x10^{-5} s^{-1} and 9.3% at 2.8x10^{-1} s^{-1}). With continuing the deformation, the increasing rate of f_{twin} is reduced at the higher strain rate ($\dot{\varepsilon} = 2.8\text{x}10^{-1}$ s^{-1}), compared to that at the lower strain rate ($\dot{\varepsilon} = 2.8\text{x}10^{-5}$ s^{-1}). This could explain the intersection of the curves, as shown in Fig. 5-12. When ε_t = 0.14, the f_{twin} at the higher strain rate of 2.8x10^{-1} s^{-1} is 45.6%, which is lower than that of 53.5% at the lower strain rate of 2.8x10^{-5} s^{-1}. It indicates that the nucleation and growth of {332}<113>$_\beta$ twins are suppresed at the higher strain rate deformation, leading to the lower area fraction of {332}<113>$_\beta$ twins.

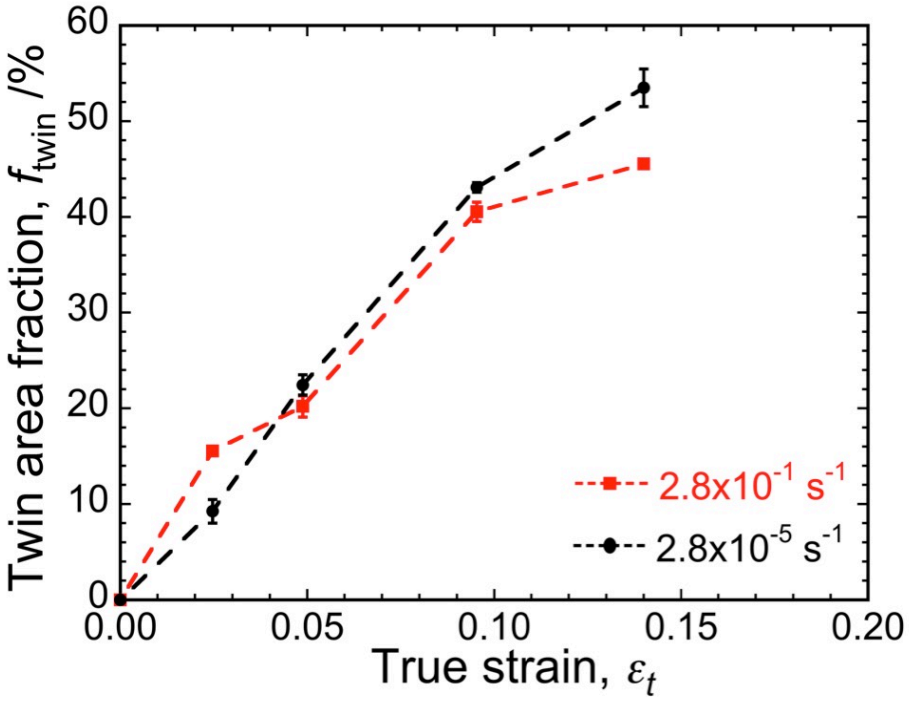

Fig. 5-12 The evolution of twin area fraction at different strain rates of 2.8x10^{-5} and 2.8x10^{-1} s^{-1}.

5.2.2.4 Evolution of dislocation density

In order to capture the effect of strain rate on the dislocation density, ρ, XRD experiments were carried out for the specimens with different strain level (0.025, 0.05, 0.10 and 0.14) at respective strain rates of $2.8\text{x}10^{-5}\ s^{-1}$ and $2.8\text{x}10^{-1}\ s^{-1}$, as well as the initial microstructure before tensile tests. For each specimen, six diffraction peaks from β phase ((110), (211), (200), (220), (321), (310)) were recorded and the full width at half maximum (FWHM) was measured.

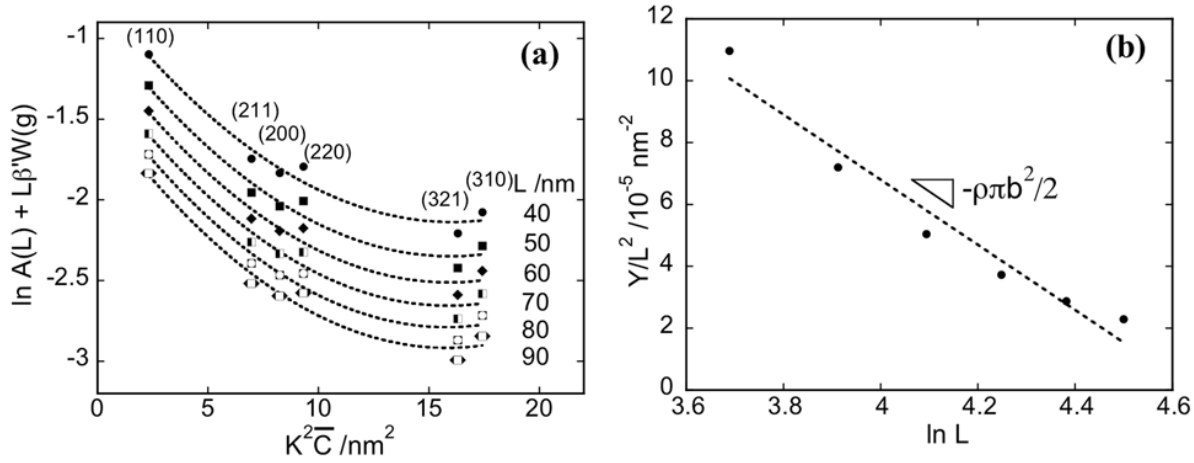

Fig. 5-13 (a) The logarithm of the Fourier coefficients vs. $K^2\bar{C}$, including the effect of planar faults, according to Eq. (5-4). (b) Y/L^2 vs. ln$L$ plot according to Eq. (5-5).

The modified Warren-Averbach method [32,33] was employed to evaluate the dislocation density. It is worth noticing that the effect of planar faults, *i.e.*, {332}<113>$_\beta$ twinning, in the broadening of diffraction peaks is incorporated into the present method. According to this method, the broadening of the diffraction peaks should be linked to the dislocation density, crystallite size and twinning and faulting probability as:

$$ln\ A(L) + L\beta' W_{hkl} \cong -\frac{L}{D} - \rho\frac{\pi b^2}{2}L^2 \ln\left(\frac{R_e}{L}\right)(K^2\bar{C}) + Q(K^4\bar{C}^2) \qquad (5-4)$$

where D, ρ and b indicate the average crystallite size, dislocation density and the magnitude of Burgers vector, respectively. Q stands for higher order terms in $K^2\bar{C}$. R_e is the effective outer cut-off radius of dislocation. W_{hkl} is a factor to scale the twinning and faulting-induced peak broadening at {hkl} reflections [34], and β' stands for the probability of finding a staking fault and twin boundary in each {hkl} plane, whose value is determined carefully in order to have a best quadratic fitting between ln$A(L)$ + $L\beta' W_{hkl}$ and $K^2\bar{C}$. *A(L)* is the real part of the Fourier coefficients of the XRD files, and defined as:

$$A_i(L) = \frac{1}{z_i}\int_{-\Delta 2\theta_{i,L}}^{\Delta 2\theta_{i,L}} \frac{W_i^2}{x^2 + W_i^2} cos\pi x dx \qquad (5-5)$$

Here, W_i is the FWHM of each diffraction peak and z_i is a coefficient of normalizing the integral intensity to be 1. x_i is the integration range with X-ray intensity, which becomes 0.1% of the maximum peak intensity. L is the Fourier variable and K=2sinθ_0/λ, λ is the wavelength of the X-rays. $\bar{C}$ is the average dislocation contrast factor, determined by:

$$\bar{C} = \bar{C}_{h00}\left[1 - q\left(\frac{h^2k^2+k^2l^2+l^2h^2}{h^2+k^2+l^2}\right)\right] \quad (5-6)$$

where $\bar{C}_{h00}$ and q are constants related to the anisotropic elastic constants (C_{11}, C_{12} and C_{44}) [35,36]. For instance, Fig. 5-13(a) shows the plot of the $\ln A(L) + L\beta' W_{hkl}$ vs. $K^2\bar{C}$ using various L values from the specimen with ε_t=0.1 at the strain rate of 2.8x10^{-1} s^{-1}. The coefficient of second term on the right side of Eq. (5-4):

$$\rho\frac{\pi b^2}{2}L^2 \ln\left(\frac{R_e}{L}\right) = Y \quad (5-7)$$

can be achived from the well-behaved smooth curves as indicated by dash lines in Fig. 5-13(a). From the linear relationship between Y/L^2 and $\ln L$ shown in Fig. 5-13(b), the value of dislocation density ρ is obtained from the gradient of the smooth linear line.

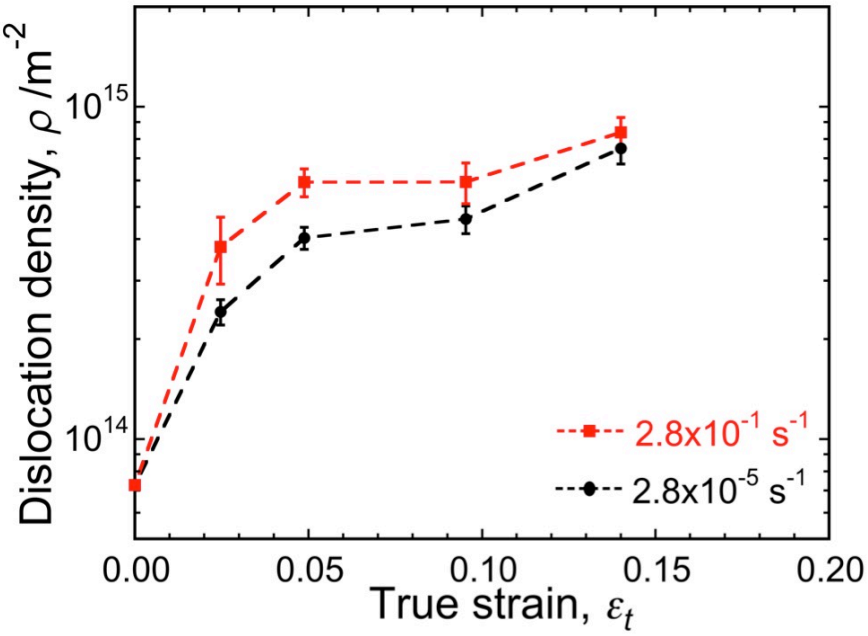

Fig. 5-14 The evolution of dislocation density at different strain rates of 2.8x10^{-5} s^{-1} and 2.8x10^{-1} s^{-1}.

The results of dislocation density at various strain rates are plotted against true strain in Fig. 5-14. The value of the initial ρ prior to deformation is expected as 7.27x10^{13} m^{-2}. When the true strain increases to 0.14, ρ increases to 7.5x10^{14} m^{-2} at the lower strain rate (2.8x10^{-5} s^{-1}) and to 8.37x10^{14} m^{-2} at the higher strain rate (2.8x10^{-1} s^{-1}), respectively. These values are comparable to the previous results in steels [33,37] and β-Ti alloys [38,39]. Fig. 5-14 also displays that an increase in the strain rate contributes to an increase in dislocation density. However, the increasing rate of dislocation density seems to be enhanced at the lower strain rate than that at the higher strain rate, which can be seen from the difference in the slope of the dislocation density curves. In other words, with continuing deformation, the dislocation generation and multiplication are suppressed to some extent and dynamic recovery is enhanced at the higher strain rates in the present Ti-10Mo-1Fe alloy.

5.3 Discussion

5.3.1 Strain rate sensitivity

Deformation at a lower strain rate leads to significantly enhanced work-hardening in the tensile deformation of Ti-10Mo-1Fe. This tendency is reflected in the strain rate sensitivity decreasing from positive to negative with the increasing strain (Fig. 5-3). At the onset of plastic deformation, the higher yield strength increases with the strain rate (Table 5-1), which indicates a higher and positive value of strain rate sensitivity. The reason for this phenomenon can be ascribed to the thermally activated dislocations in bcc alloys; thus a higher yield stress is required to overcome the improved Peierls potential and active the dislocation motion at a higher strain rate [40]. With continuing plastic deformation, the increase of flow stress at the higher strain rate is less pronounced than that at the lower strain rate. This is attributed to the corresponding lower work-hardening rate (Fig. 5-2). Eventually, a higher strain rate leads to a lower flow stress when the strain exceeds 0.13 (Fig. 5-2), indicating negative strain rate sensitivity. Similar behaviors have been reported in some TWIP steels [21], Mg alloys [41], and Ti/Ni multilayers [42]. Smooth plastic flow without any trace of serration can be observed in Fig. 5-1. It suggests that the whole plastic deformation process of the present Ti-10Mo-1Fe alloy is free of DSA effect. The strain rate sensitivity (m) of the present alloy was studied in terms of strain rate sensitivity of work-hardening (m_θ). The m_θ dealing with the microstructure evolution caused by different strain rate displayed negative value and distinctly decreased with true strain, Fig. 5-4, whereas the m_i concerning the strain rate effect on the existing microstructure showed a positive and constant value (Fig. 5-6). The above results suggest that the ascending m with the strain is mainly attributed to the negative m_θ.-Thus the decreasing strain rate sensitivity during the plastic deformation may be associated with the lower increasing rates of $\{332\}\langle 113\rangle_\beta$ twins (Fig. 5-12) and dislocation density (Fig. 5-14) at higher strain rate deformation [20,21,43].

5.3.2 Work-hardening behavior

According to the previous studies [12,44], the mechanism of the work-hardening related with the twinning structure is because of the reduction of dislocation mean free path by the formation of twins, known as dynamic Hall-Patch effect (Fig. 5-8(a)). In addition, the twin-twin interaction (as shown in Fig. 5-8(b)) also contributes to the work-hardening [45]. The twin-twin intersection contributes to the reduction of twin propagation rate, which had post likely induced stress concentration. Thus the twin nucleation events may be promoted, as the stress of twinning nucleation is known to be higher than that of twin propagation [46]. Besides, the activation of secondary twins in the crossed twins as accompanying the twin-twin intersection (shown as an example in Fig. 5-8(b)) is also considered to enhance the effectiveness of deformation twinning for the substantial work hardening behavior [47]. Furthermore, it has been found that the dislocation evolution during plastic deformation also makes significant contributions to the work-hardening [48,49]. According to Klepaczko *et al.* [23], the microstructure evolution at different strain rates contributes to the change of macroscopic work-hardening rate. In the present work, the higher strain rate deformation exhibits a lower work-hardening rate (Fig. 5-2), which indicates the weakened ability of work-hardening by

increasing the strain rate. Thus, the strain rate dependence of work-hardening behavior is discussed based on the quantification of {332}<113>$_\beta$ twins (Fig. 5-12) and dislocations (Fig. 5-14) evolutions at different strain rates deformation.

More twins and dislocations are observed in the early stage of plastic deformation ($\varepsilon_t \sim 0.05$) at higher strain rate, as shown in Fig. 5-12 and Fig. 5-14. The critical resolve stress of the {332}<113>$_\beta$ twinning has been stated with negligible dependence on the strain rate [24]. The twin nucleation events are thus assumed to be enhanced by the higher density of dislocations at the higher strain rate deformation [50], as indicated in Fig. 5-14. With the work-hardening mechanism, a higher flow stress is required to continue the plastic deformation, resulting in positive strain rate sensitivity (Fig. 5-3). However, the increasing rates of {332}<113>$_\beta$ twins and dislocation density are observed to be lower at the higher strain rate ($2.8\text{x}10^{-1}$ s^{-1}) than those at the lower strain rate deformation ($2.8\text{x}10^{-5}$ s^{-1}) when the strain exceeds 0.025. Consequently, a lower work-hardening rate at a higher strain rate deformation would be obtained, as displayed in Fig. 5-2.

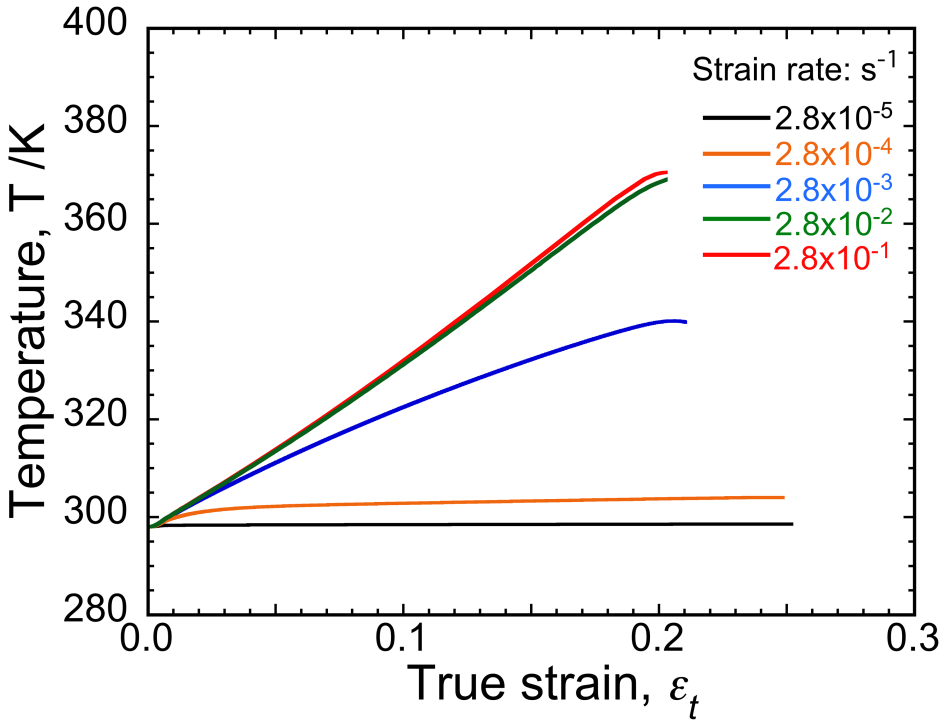

Fig. 5-15 The evolution of temperature with true strain at different strain rates of calculated from Eq. (5-8).

A temperature increase due to adiabatic heating may play an important role on the deformation behavior. Adiabatic heating generated at a high strain rate deformation has been reported to stabilize the austenite matrix in austenitic stainless steels, resulting in the suppression of stress-induced α″ martensitic transformation [51,52]. Ahmed *et al*. [24] have reported that the temperature rise induced by the high strain rate may significantly stabilize the β phase in Ti-10V-3Fe-3Al (wt.%) alloy, leading to the alteration of dominant deformation mechanism from stress-induced α″ martensitic transformation ($\leq 10^{-3}$ s^{-1}) to {332}<113>$_\beta$ twinning ($\geq 10^{1}$ s^{-1}). In the present study, the evolution of temperature is evaluated by considering the rise of temperature from the external work minus the heat lost due to conduction to the sample holders [37]:

$$dT = \frac{\eta \sigma_t d\varepsilon_t}{\rho_w C} - \frac{2\alpha}{\rho_w C L^2}(T - T_0)\frac{d\varepsilon_t}{\dot{\varepsilon}} \qquad (5-8)$$

where C is heat capacity (taken as 0.49 kJ/kg/K which is the typical value for β-Ti), ρ_w is the density (~ 4.93 g/cm^3), α is the thermal conductivity coefficient (~ 7.6 W/m/K), η is the heat fraction coefficient (~ 0.95 [26]), L is the gauge length of the tensile specimen, and T_o is the temperature of the sample holder (~ 300K). Based on the Eq. 5-8, the temperature rise of the specimen at various strain rates deformation was estimated and is plotted as a function of true strain in Fig. 5-15. Temperature increase is expected to reach 100K before fracture at the highest strain rate deformation of 2.8×10^{-1} s^{-1}, whereas the temperature at the lowest strain rate of 2.8×10^{-5} s^{-1} remains constant.

It is possible that a temperature rise during deformation by adiabatic heating leads to an increase in the thermodynamic stability of β phase, which, in turn, changes the predominant deformation mode from {332}<113>$_\beta$ twins to dislocation slip [24,29,53]. In fact, Zhan *et al*. [29] reported suppression of {332}<113>$_\beta$ twinning by increasing the testing temperature from 298K to 873K in Ti-25Nb-3Zr-3Mo-3Sn (wt.%) alloy. Another cause for the suppression of {332}<113>$_\beta$ twinning may be related to lattice instability of β-Ti alloys. {332}<113>$_\beta$ twinning is a unique twinning mode, which can be identified exclusively in metastable β-Ti alloys. Close relation with stress-induced ω phase has been reported by Hanada *et al*. [11,54]. More recently, Tobe *et al*. found that the lattice instability of bcc lattice (the lower shear modulus c' (= (c_{11}-c_{12})/2)) contributes to the modulation of {110}<110>$_\beta$ and to tetragonal distortion which facilitates {332}<113>$_\beta$ twinning [55]. It is well acknowledged for β alloys presenting displacive transformation, *e.g.*, martensitic transformation or omega phase transformation, that the lattice instability develops with lowering temperatures toward the transformation temperatures [56]. Hence it is supposed that a temperature increase by adiabatic heating retards the nucleation and growth of {332}<112>$_\beta$ twins, and consequently, to decrease the contribution of dynamic Hall-Petch effect to the work-hardening rate. In addition, the effect of adiabatic heating can have great effect on the dislocation dynamics. Dynamic recovery contains a thermally activated process of climb and cross slip, contributing to the annihilation of dislocations [37,57]. The temperature rise at the late stage of deformation can promote dislocation annihilation and lower dislocation density (Fig. 5-14), resulting in the lower work hardening rate observed at higher strain rate deformation as indicated in Fig. 5-2.

To summarize the discussion, the lower work hardening rate at the higher strain rate deformation may be ascribed to the reduced formation of {332}<113>$_\beta$ twins and enhanced dynamic recovery, especially in the late stage of deformation. Furthermore, since the enhanced work-hardening rate suppresses the localization of the deformation and delays plastic instability [58], larger uniform elongation can be achieved (Fig. 5-2). In conclusion, the obtained strain rate sensitivity of the Ti-10Mo-1Fe alloy is rationalized at least qualitatively in terms of the microstructure evolution affected by the adiabatic heating.

5.4 Conclusion

In the present work, the effect of strain rate in the range between $2.8x10^{-5}$ s^{-1} and $2.8x10^{-1}$ s^{-1} on the tensile properties and work-hardening behavior in a β-type Ti-10Mo-1Fe alloy has been investigated. The main results are summarized below:

(1) From the monotonic tensile tests at different strain rates up to fracture, the yield strength (YS) increases with increasing the strain rate from 2.8x10-5 to 2.8x10-1 s-1, whereas the ultimate tensile strength (UTS), total elongation (tEL) as well as uniform elongation (uEL) show a decreasing tendency. From the strain rate jump tests, the instantaneous strain rate sensitivity achieved from strain rate jump tests remains stable and positive with strain.

(2) The strain rate sensitivity decreases with increasing strain, showing a transition from positive to negative. The higher strain rate deformation exhibits a lower work-hardening rate.

(3) The $\{332\}<113>_{\beta}$ twinning dominates the deformation mechanism of the Ti-10Mo-1Fe alloy. Electron Backscattered Diffraction (EBSD) and X-ray diffraction (XRD) results indicate lower increasing rates of $\{332\}<113>_{\beta}$ twins and dislocation density at the higher strain rate, leading to a reduced work-hardening rate. This phenomenon is associated with the adiabatic heating generated at the higher strain rate deformation.

References

[1] R.R. Boyer, An overview on the use of titanium in the aerospace industry, Mater. Sci. Eng. A. 213 (1996) 103–114.

[2] P.J. Bania, Beta titanium alloys and their role in the titanium industry, JOM. 46 (1994) 16–19. [3] M. Niinomi, Mechanical biocompatibilities of titanium alloys for biomedical applications, J. Mech. Behav. Biomed. Mater. 1 (2008) 30–42.

[4] R.P. Kolli, W.J. Joost, S. Ankem, Phase Stability and Stress-Induced Transformations in Beta Titanium Alloys, JOM. 76 (2015) 1273–1280.

[5] M. Marteleur, F. Sun, T. Gloriant, P. Vermaut, P.J. Jacques, F. Prima, On the design of new β-metastable titanium alloys with improved work hardening rate thanks to simultaneous TRIP and TWIP effects, Scr. Mater. 66 (2012) 749–752.

[6] X.H. Min, K. Tsuzaki, S. Emura, K. Tsuchiya, Heterogeneous twin formation and its effect on tensile properties in Ti–Mo based β titanium alloys, Mater. Sci. Eng. A. 554 (2012) 53–60.

[7] S. Hanada, M. Ozeki, O. Izumi, Deformation Characteristics in β Phase Ti-Nb Alloys, Metall. Trans. A. 16 (1985) 789–795.

[8] M. Oka, Y. Taniguchi, Stress-induced Products in Meta-stable Beta Ti-Mo and Ti-V Alloys, J. Japan Inst. Met. (1978) 814–820.

[9] S. Hanada, O. Izumi, Transmission Electron Microscopic Observations of Mechanical Twinning in Metastable Beta Titanium Alloys, Metall. Trans. A. 17 (1986) 1409–1420.

[10] X.F. Zhao, M. Niinomi, M. Nakai, J. Hieda, T. Ishimoto, T. Nakano, Optimization of Cr content of metastable β-type Ti–Cr alloys with changeable Young's modulus for spinal fixation applications, Acta Biomater. 8 (2012) 2392–2400.

[11] S. Hanada, T. Yoshio, O. Izumi, Effect of Plastic Deformation Modes on Tensile Properties of Beta Titanium Alloys, Trans. Japan Inst. Met. 27 (1986) 496–503. doi:10.2320/matertrans1960.27.496.

[12] X.H. Min, X.J. Chen, S. Emura, K. Tsuchiya, Mechanism of twinning-induced plasticity in β-type Ti–15Mo alloy, Scr. Mater. 69 (2013) 393–396.

[13] X.H. Min, S. Emura, T. Nishimura, K. Tsuchiya, K. Tsuzaki, Microstructure, tensile deformation mode and crevice corrosion resistance in Ti–10Mo–xFe alloys, Mater. Sci. Eng. A. 527 (2010) 5499–

5506.
[14] L. Remy, Kinetics of f.c.c. deformation twinning and its relationship to stress-strain behaviour, Acta Metall. 26 (1978) 443–451.
[15] H. Zhan, G. Wang, D. Kent, M. Dargusch, Constitutive modelling of the flow behaviour of a β titanium alloy at high strain rates and elevated temperatures using the Johnson–Cook and modified Zerilli–Armstrong models, Mater. Sci. Eng. A. 612 (2014) 71–79.
[16] K. Ogawa, Temperature and strain rate effects on plastic deformation of titanium alloys, Mater. Sci. Forum. 539–543 (2007) 3619–3624.
[17] E. Farghadany, A. Zarei-Hanzaki, H.R. Abedi, D. Dietrich, M.R. Yadegari, T. Lampke, The coupled temperature–strain rate sensitivity of Ti–29Nb–13Ta–4.6Zr alloy, Mater. Sci. Eng. A. 610 (2014) 258–262.
[18] S.T. Chiou, H.L. Tsai, W.S. Lee, Effects of Strain Rate and Temperature on the Deformation and Fracture Behaviour of Titanium Alloy, Mater. Trans. 48 (2007) 2525–2533.
[19] S.J. Lee, J.Y. Kim, S.N. Kane, B.C. De Cooman, On the origin of dynamic strain aging in twinning-induced plasticity steels, Acta Mater. 59 (2011) 6809–6819.
[20] H.K. Yang, Z.J. Zhang, F.Y. Dong, Q.Q. Duan, Z.F. Zhang, Strain rate effects on tensile deformation behaviors for Fe–22Mn–0.6C–(1.5Al) twinning-induced plasticity steel, Mater. Sci. Eng. A. 607 (2014) 551–558.
[21] A. Bintu, G. Vincze, C.R. Picu, A.B. Lopes, J.J. Grácio, F. Barlat, Strain hardening rate sensitivity and strain rate sensitivity in TWIP steels, Mater. Sci. Eng. A. 629 (2015) 54–59.
[22] H.K. Yang, Y.Z. Tian, Z.J. Zhang, Z.F. Zhang, Different strain rate sensitivities between Fe–22Mn–0.6C and Fe–30Mn–3Si–3Al twinning-induced plasticity steels, Mater. Sci. Eng. A. 655 (2016) 251–255.
[23] J.R. Klepaczko, C.Y. Chiem, On rate sensitivity of f. c. c. metals, instantanious rate sensitivity and rate sensitivity of strain hardening, J. Mech. Phys. Solids. 34 (1986) 29–54.
[24] M. Ahmed, D. Wexler, G. Casillas, D.G. Savvakin, E. V. Pereloma, Strain rate dependence of deformation-induced transformation and twinning in a metastable titanium alloy, Acta Mater. 104 (2016) 190–200.
[25] W.S. Lee, C.F. Lin, T.H. Chen, H.H. Hwang, High strain rate deformation of Ti–15Mo–5Zr–3Al alloy over wide temperature range, Mater. Sci. Technol. 24 (2008) 15–25.
[26] S. Bruschi, S. Poggio, F. Quadrini, M.E. Tata, Workability of Ti-6Al-4V alloy at high temperatures and strain rates, Mater. Lett. 58 (2004) 3622–3629.
[27] S.Q. Wang, J.H. Liu, D.L. Chen, Effect of strain rate and temperature on strain hardening behavior of a dissimilar joint between Ti–6Al–4V and Ti17 alloys, Mater. Des. 56 (2014) 174–184.
[28] C. Li, J.H. Chen, X. Wu, S. van der Zwaag, Effect of strain rate on stress-induced martensitic formation and the compressive properties of Ti–V–(Cr,Fe)–Al alloys, Mater. Sci. Eng. A. 573 (2013) 111–118.
[29] H. Zhan, G. Wang, D. Kent, M. Dargusch, The dynamic response of a metastable β Ti–Nb alloy to high strain rates at room and elevated temperatures, Acta Mater. 105 (2016) 104–113.
[30] I.S. Yasnikov, A. Vinogradov, Y. Estrin, Revisiting the Considere criterion from the viewpoint of dislocation theory fundamentals, Scr. Mater. 76 (2014) 37–40.
[31] M.J. Blackburn, J.A. Feeney, Stress-Induced Transformations in Ti-Mo alloys, J. Inst. Met. 99 (1971) 132–134.
[32] T. Ungár, S. Ott, P.. Sanders, A. Borbély, J.. Weertman, Dislocations, grain size and planar faults in nanostructured copper determined by high resolution X-ray diffraction and a new procedure of peak profile analysis, Acta Mater. 46 (1998) 3693–3699.
[33] T. Shintani, Y. Murata, Evaluation of the dislocation density and dislocation character in cold rolled Type 304 steel determined by profile analysis of X-ray diffraction, Acta Mater. 59 (2011) 4314–4322.
[34] B.E. Warren, X-ray studies of deformed metals, Prog. Met. Phys. 8 (1959) 147–202.
[35] M. Tane, T. Nakano, S. Kuramoto, M. Hara, M. Niinomi, N. Takesue, T. Yano, H. Nakajima, Low Young's modulus in Ti-Nb-Ta-Zr-O alloys: Cold working and oxygen effects, Acta Mater. 59 (2011) 6975–6988.
[36] T. Ungár, I. Dragomir, Á. Révész, A. Borbély, The contrast factors of dislocations in cubic crystals: the dislocation model of strain anisotropy in practice, J. Appl. Crystallogr. 32 (1999) 992–1002.
[37] Z.Y. Liang, X. Wang, W. Huang, M.X. Huang, Strain rate sensitivity and evolution of dislocations and twins in a twinning-induced plasticity steel, Acta Mater. 88 (2015) 170–179.

[38] M. Ahmed, D.G. Savvakin, O.M. Ivasishin, E. V. Pereloma, The effect of cooling rates on the microstructure and mechanical properties of thermo-mechanically processed Ti–Al–Mo–V–Cr–Fe alloys, Mater. Sci. Eng. A. 576 (2013) 167–177.
[39] H. Yilmazer, M. Niinomi, K. Cho, M. Nakai, J. Hieda, S. Sato, Y. Todaka, Nanostructure of β-type titanium alloys through severe plastic deformation, Adv. Mater. Lett. 5 (2014) 378–383.
[40] E. El-Magd, Mechanical properties at high strain rates, Le J. Phys. IV. 4 (1994) 149–170.
[41] Y.B. Chun, C.H.J. Davies, Twinning-induced negative strain rate sensitivity in wrought Mg alloy AZ31, Mater. Sci. Eng. A. 528 (2011) 5713–5722.
[42] J. Shi, Z.H. Cao, J.G. Zheng, Size dependent strain rate sensitivity transition from positive to negative in Ti/Ni multilayers, Mater. Sci. Eng. A. 680 (2017) 210–213.
[43] S. Sun, A. Zhao, Q. Wu, Effect of strain rate on the work-hardening rate in high-Mn steel, Mater. Sci. Technol. 33 (2017) 1306–1311.
[44] L.M. Clarebrough, M.E. Hargreaves, Work hardening of metals, Prog. Met. Phys. 8 (1959) 1–103.
[45] H. El Kadiri, J. Kapil, a. L. Oppedal, L.G. Hector, S.R. Agnew, M. Cherkaoui, S.C. Vogel, The effect of twin–twin interactions on the nucleation and propagation of twinning in magnesium, Acta Mater. 61 (2013) 3549–3563.
[46] J.W. Christian, S. Mahajant, Deformation Twinning, Prog. Mater. Sci. 39 (1995) 1–157.
[47] X. Zhou, X. Min, S. Emura, K. Tsuchiya, Accommodative {332} primary and secondary twinning in a slightly deformed β-type Ti-Mo titanium alloy, Mater. Sci. Eng. A. (2016).
[48] Z.Y. Liang, Y.Z. Li, M.X. Huang, The respective hardening contributions of dislocations and twins to the flow stress of a twinning-induced plasticity steel, Scr. Mater. 112 (2016) 28–31.
[49] B.C. De Cooman, O. Kwon, K.G. Chin, State-of-the-knowledge on TWIP steel, Mater. Sci. Technol. 28 (2012) 513–527.
[50] M.A. Meyers, O. Vöhringer, V.A. Lubarda, The onset of twinning in metals: a constitutive description, Acta Mater. 49 (2001) 4025–4039.
[51] A. Das, S. Tarafder, P.C. Chakraborti, Estimation of deformation induced martensite in austenitic stainless steels, Mater. Sci. Eng. A. 529 (2011) 9–20.
[52] C.P. Livitsanos, P.F. Thomson, The effect of temperature and deformation rate on transformation-dependent ductility of a metastable austenitic stainless steel, Mater. Sci. Eng. 30 (1977) 93–98.
[53] H.Y. Zhan, W.D. Zeng, G. Wang, D. Kent, M. Dargusch, On the deformation mechanisms and strain rate sensitivity of a metastable β Ti–Nb alloy, Scr. Mater. 107 (2015) 34–37.
[54] S. Hanada, O. Izumi, Correlation of tensile properties, deformation modes, and phase stability in commercial β-phase titanium alloys, Metall. Trans. A. 18 (1987) 265–271.
[55] H. Tobe, H.Y. Kim, T. Inamura, H. Hosoda, S. Miyazaki, Origin of {332} twinning in metastable β-Ti alloys, Acta Mater. 64 (2014) 345–355.
[56] X. Ren, N. Miura, J. Zhang, K. Otsuka, K. Tanaka, M. Koiwa, T. Suzuki, Y.. Chumlyakov, M. Asai, A comparative study of elastic constants of Ti–Ni-based alloys prior to martensitic transformation, Mater. Sci. Eng. A. 312 (2001) 196–206.
[57] W. Puschl, Models for dislocation cross-slip in close-packed crystal structures: A critical review, Prog. Mater. Sci. 47 (2002) 415–461.
[58] R. Liu, Z.J. Zhang, L.L. Li, X.H. An, Z.F. Zhang, Microscopic mechanisms contributing to the synchronous improvement of strength and plasticity (SISP) for TWIP copper alloys, Sci. Rep. 5 (2015) 9550.

Chapter 6 Conclusion

The present study has been focused on the mechanical properties (tensile properties, hardness, and Young's modulus) and deformation mechanisms (mainly twinning) of β-type Ti-Mo alloys.

The deformation mechanisms of α" martensite in Ti-7.5Mo alloy have been investigated. The as-quenched α″ martensite has been revealed with an internal twinning structure of $\{111\}_{\alpha''}$-type I transformation twinning, which is induced as a lattice invariant shear to accommodate the β→α″ martensitic transformation. After 5% tensile straining, the activation of deformation twins and dislocation slips were confirmed by SEM observation. The deformation twinning system was further identified as $\{112\}_{\alpha''}$-type I twinning by TEM, which has been firstly reported in the orthorhombic-α" martensite of β-Ti alloys. Based on the crystallographic theory of deformation twinning proposed by Bilby and Crocker, the mechanism of the $\{112\}_{\alpha''}$-type I twinning has been analyzed in terms of atomic shears and shuffles.

In order to improve the relatively low strength of Ti-7.5Mo alloy, various amounts of oxygen were added. The effects of oxygen contents (0 ~ 0.5 wt.%) on the microstructure and mechanical properties of Ti-7.5Mo alloy have been investigated. The as-quenched Ti-7.5Mo-xO (x = 0, 0.2, 0.3, 0.4 and 0.5 (wt.%)) alloys are composed mainly of α″ martensite. Additional α phase has been detected in 0.4O and 0.5O alloys, attributed to the α-stabilizing effect by the interstitial oxygen atoms. With increasing the oxygen content, the Vickers micro-hardness, yield strength, ultimate tensile strength, and Young's modulus increase, while their total elongation and uniform elongation decrease. This is ascribed to the solid-solution strengthening by the interstitial oxygen atoms. In the present study, 0.2O and 0.3O alloys exhibit an excellent combination of high yield strength and elongation, as well as low Young's modulus values. The addition of oxygen (≤ 0.3 wt.%) is suggested as an effective method to improve the balance of tensile properties of Ti-7.5Mo alloy. Compared to other multicomponent alloys, these alloys may be more cost effective and potential candidate materials for biomedical applications.

Meanwhile, the effect of strain rate (2.8×10^{-5} s^{-1} ~ 2.8×10^{-1} s^{-1}) on the tensile properties and work-hardening behavior in the Ti-10Mo-1Fe alloy has been investigated, which is focused on the $\{332\}\langle113\rangle_{\beta}$ twinning in bcc-β phase. The strain rate sensitivity decreases with increasing strain, showing a transition from positive to negative. The higher strain rate deformation exhibits a lower work-hardening rate. The $\{332\}\langle113\rangle_{\beta}$ twinning dominates the deformation mechanism of the Ti-10Mo-1Fe alloy. The microstructural evolution including $\{332\}\langle113\rangle_{\beta}$ twinning and dislocation density during the tensile deformation at different strain rates have been evaluated by EBSD and XRD techniques. The results indicate lower increasing rates of $\{332\}\langle113\rangle_{\beta}$ twins and dislocation density at the higher strain rate, leading to a reduced work-hardening rate. This phenomenon is associated with the adiabatic heating generated at the higher strain rate deformation.

Acknowledgement

This study was performed throughout the doctoral course in Materials Science and Engineering at the University of Tsukuba under the joint program between National Institute for Materials Science (NIMS) and the University of Tsukuba.

It has been almost five years since I started the life in Tsukuba. I have been really lucky since so many great people have supported me and made me enjoy the life here. I cannot express enough my gratitude with the limited words.

First and foremost, I would like to give my sincere gratitude to my supervisor, Prof. Koichi Tsuchiya, without whom my research would be impossible. I cannot forget the first interview with Prof. Tsuchiya in Sendai. I am so proud to become one of his students. For the past five years, Prof. Tsuchiya has guided me with wise counsel and precious support. His patience, enthusiasm and immense knowledge will inspire my whole life.

In addition, I would like to thank Dr. Satoshi Emura for his invaluable guidance and instructions through out my study and being the member of my committee. Furthermore, I would like to extent my gratitude to the other members of the committee: Prof. Hee Young Kim and Prof. Masanobu Naito for their valuable instructions and comments.

Needless to say, I owe my grateful appreciation to all the members of the Corrosion Resistance Alloy Group at NIMS, Dr. Ivan Gutierrez-Urrutia, for his insightful comments. I really learned a lot through the discussion with him; Dr. Baozhen Jiang, Dr. Jian Qiang, Dr. ThiHaiYen Nguyen and Mr. Wataru Tasaki for their generous help; Ms. Yumiko Komai for her technical assistance; Ms. Kayo Sasame and Ms. Kyouko Nemoto for their kind support. Meanwhile, I would like to express a special gratitude to Ms. Tomomi Utagawa who treated me like her daughter and helped me a lot in my life in Tsukuba. I feel so lucky that I could join such a friendly and cheerful group. I am also grateful to the engineers in Materials Manufacturing and Engineering Station at NIMS for alloy preparation.

Last but not least, I must thank my family in China for their persistent care and encouragement. Their love and support will always be my motivation to advance.